COMBUSTION EFFICIENCY FROM INDUSTRIAL FLARES WITH UNCERTAINTY QUANTIFICATION

by

Anchal Jatale

A dissertation submitted to the faculty of
The University of Utah
in partial fulfillment of the requirements for the degree of

Doctor of Philosophy

Department of Chemical Engineering

The University of Utah

August 2014

The University of Utah Graduate School

STATEMENT OF DISSERTATION APPROVAL

The dissertation of **Anchal Jatale**

has been approved by the following supervisory committee members:

Philip J. Smith	, Chair	**5-5-2014** Date Approved
Jeremy N. Thornock	, Member	**4-22-2014** Date Approved
James C. Sutherland	, Member	**4-23-2014** Date Approved
Meredith M. Metzger	, Member	**4-20-2014** Date Approved
Rajesh Rawat	, Member	**4-16-2014** Date Approved

and by **Milind Deo** , Chair/Dean of

the Department/College/School of **Chemical Engineering**

and by David B. Kieda, Dean of The Graduate School.

ABSTRACT

The increasing cost of full-scale testing makes model-based computational methods very important for the reliability assessment of large complex systems. However, physical, statistical, and model uncertainties make it difficult to have high confidence in model-based reliability prediction. Hence, there is an important need to validate model predictions using test data. However, for large-scale systems, availability of test results is rare. This kind of problem can be validated from obtaining test data to validate smaller modules (subsystem and component-level models) of the overall reliability computational model.

A framework for Validation and Uncertainty Quantification (VUQ) of a model for an overarching problem with no prior experimental data is implemented on one such problem, measurement of combustion efficiency for industrial flares. The hierarchical VUQ process begins with defining lower subsystems. For the current overarching problem, a nonreacting buoyancy-driven turbulent mixing experiment was selected as a component-scale case and wind-tunnel flare experiments as a pilot-scale case.

A 6-step systematic validation framework is adopted from the literature and applied to provide upper and lower bounds of the prediction. Each brick/level in the hierarchy is validated individually as well as together as one big system to propagate the uncertainties and to build confidence in the model. Monte-Carlo method and consistency constraints are used to analyze surrogate models, constructed for complex and expensive

multiphysics simulators. The analysis refines the parameter space where the model makes valid predictions and with certain confidence.

To My Family

TABLE OF CONTENTS

LIST OF TABLES

LIST OF FIGURES

ACKNOWLEDGMENTS

First and foremost, I want to thank my advisor, Dr. Philip Smith. It has been an honor to be his Ph.D. student. This thesis would not have been possible without his help and support, not to mention his unsurpassed knowledge of computational combustion. He patiently provided the vision, encouragement, and the advice necessary for me to go through the doctoral program and complete my dissertation. The joy and enthusiasm he has for his research was contagious and motivational for me, even during tough times in my Ph.D. pursuit. The experience I gained throughout my graduate studies under his leadership proved to be invaluable.

I am also thankful to Dr. Jeremy Thornock for his valuable input, guidance, and advice throughout the course of my doctorate. He has been always available for helping me out and answering my questions. Special thanks to other members of my committee, Dr. James Sutherland, Dr. Meredith Metzger, and Rajesh Rawat, for their constant guidance, helpful suggestions, and understanding throughout my research, as well as for taking time to answer all of my questions, and ask tough questions in return. Throughout these discussions, I was able to expand my knowledge and gain perspectives I would not be able to achieve on my own. The guidance has served me well and I owe them my heartfelt appreciation. I will also like to thank Rajesh Rawat for providing abundant help and support with STAR-CCM+ throughout the last 5 years.

I gratefully acknowledge the funding sources that made my Ph.D. work possible. I was funded by John Zink Company LLC for the 4 years. My work was also supported by CSAFE and Spectral Sciences Inc.

I would like to express special gratitude to my colleagues Michal Hradisky and Naveen Punati for all their help and willingness to share their knowledge with me. I want to thank them for all the interesting and insightful conversations we had related to the work as well as other stuff. I am also very grateful to other faculty members, staff, and fellow CRSIM group members at the University of Utah for their support and help.

I wish to thank my family members for their love and support throughout this endeavor. My parents and sister have given me their unequivocal support throughout, as always, for which my mere expression of thanks likewise does not suffice. A special thanks is also due to my friends in Salt Lake City for providing me with a family away from home.

Finally, I would like to give my greatest thanks to my wife, Vintee. Her love and encouragement allowed me to finish this journey. Words cannot express how grateful I am for her continuous support and understanding.

CHAPTER 1

INTRODUCTION

Computer simulations are very important in engineering and design. Be it the aerospace, chemical, construction, or mechanical industry, all use simulation extensively to improve their productivity. Even government agencies use simulations to effectively develop public policies and prepare safety procedures. This growing dependency on computer simulations makes it essential to have confidence in the results [1]. The practical utility of the results of a numerical simulation is proportional to the degree to which the error and uncertainty in the simulation results have been quantified. Once this is done, a tool can be used to predict results accurately for any scenario, even if such measurement is not possible in experiments. Computational Fluid Dynamics (CFD) code also needs to be validated before its use. Most of the available strategies to validate a code are based on the logic that simulation data should be in close conjunction with experimental results. One such technique is Verification Validation and Uncertainty Quantification (V&VUQ). This technique focuses on a combination of 3 processes, which, together, determines both numerical and physical accuracy. This technique also measures the deviation of the model output from the experiments. Figure 1.1 describes this approach schematically [2,3]. The cyclical nature of the process allows the transfer of information back and forth many times, thus improving the model as a whole by reducing the errors. Simply stated, verification is related to numerics while validation deals with the physics of the model [4].

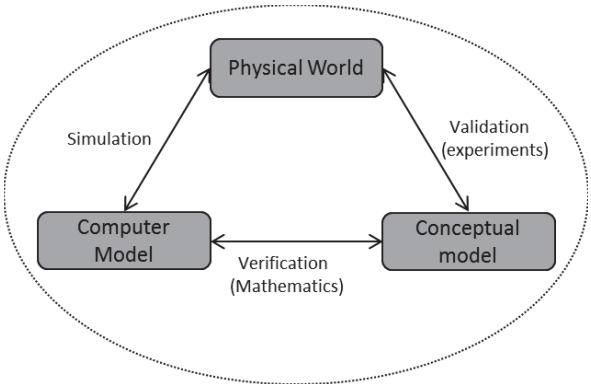

Fig 1.1: Validation and Verification Cycle (Apapted from [2, 3])

The scope and complexity of many real-world problems result in very sparse and expensive 'a priori' experimental data. Such a lack of data does not allow validation of the model. Yet this issue may be tackled by building a hierarchical validation framework. In this framework, the computational and experimental data are integrated through a range of experimental scales and a hierarchy of complexity levels, ultimately creating the prediction of the complex application with data and models from simpler systems lower in the tree. The V&VUQ analysis is undertaken by organizing data around a central overarching problem, with a goal of producing quantified error bounds for the important metrics of the central problem. The lower bricks of the hierarchy include smaller-scale problems. The selection of the smaller-scale problems is based on some similarity with the overarching problem's physics and the presence of experimental data [5]. The hierarchy provides a concept for isolating the physics that contribute to the intended use of the model and quantifying errors at each of the different levels. It also provides insight into error propagation from the various isolated submodels. One such overarching problem is the measurement of combustion efficiency for an industrial flare system. The primary objective of flares is to burn unwanted combustible gases released during

industrial operations in an effective and safe manner [6]. Since hydrocarbon gases like methane are 20 times more effective at trapping heat in the atmosphere when compared with combustion products such as CO_2, the effect of flaring hydrocarbon on air quality is of major concern to both government and industry [7]. Thus, an understanding of flare effectiveness is very important. At this point, combustion efficiency is the most commonly used quantity to describe the effectiveness of such systems. Yet the lack of experimental data for combustion efficiency is a main worry in the flare community.

Flaring systems carry numerous problems, such as the effect of high temperatures and radiant heat on equipment, the effect of external winds and intrinsic turbulence on the nature of flare flames, the unclear dilution of flare emission plume with ambient air, the lack of suitable sampling locations, etc. It is also difficult to measure combustion efficiency, since one must know simultaneously both the composition and velocity to obtain a mass flux surrounding the reacting flare. Hence, very limited published research on the combustion efficiency of flares in open environment is available. Most of the prominent studies were performed in smaller pilot-scale set ups [8-11]. Researchers have shown that the combustion efficiency of flares can be very high (>98%) for a wide range of flow rates and flare gas compositions [12]. However, studies also found that some flares had efficiencies as low as 62% [13]. In order to design a highly efficient flare system, knowledge of the unsteady mixing phenomena is important. That being said, the wide variety of fuel composition, fuel velocities, ambient wind conditions, and the size of the flare equipment make these experimental studies unreasonable. One way to tackle this problem cost-effectively is by using computational combustion simulations. Still, the process of validating a model to predict desired quantities with certain confidence is

hampered by the lack of experimental data. This dissertation proposes a hierarchical method in order to validate a model and make it useful for prediction of an overarching problem, like measurement of combustion efficiencies from industrial flare systems, where experimental data are not readily available.

The combustion physics of industrial flares is very turbulent and features multiple reactions. The temperature ranges in flares also give rise to radiation heat transfer. Turbulent combustion applications have such complex physics coupled with a wide range of length and time scales. In order to completely resolve these scales for numerical simulations, extremely unrealistic computing powers are required. Thus, the majority of industry uses standard Reynolds Averaged Navier-Stokes (RANS) methods, which are less resource intensive and provide results in less time. The RANS methods, however, are unable to represent any timescale dependency, an important aspect of flare physics. They are also incapable of capturing fuel separation mechanism at high winds or any unsteady information, such as instantaneous mixing and flame shape. Due to these limitations, the Large Eddy Simulation (LES) model was used for performing the simulations. LES takes advantage of the recent increase in computing power and captures a large range of turbulent time and length scales. This, in turn, provides a better measurement of combustion efficiency.

The hierarchical tree for the overarching problem consists of a component-scale and pilot-scale brick. Because of the expensive computational nature of LES simulations, buoyant-flow experiments play an important role in validating a model used for predictions of systems with high complexity, like combustion. Though they sound simple, buoyancy-driven flows provide their own challenges in the form of an inverse

energy cascade. Gravitational forces acting on the fluids give rise to density stratifications, which, in turn, produce Rayleigh-Taylor instabilities [14,15]. A 1 m nonreacting helium-plume flow makes a good case for studying generation of turbulence due to buoyancy without the complexities of combustion and radiation that would take place in a fire; hence, it was chosen as the component-scale brick of the hierarchy.

The pilot-scale brick was made up of wind-tunnel flare experiments performed at CETC (CANMET Energy Technology Centre) flare testing facility in Ottawa, Canada. This experiment reports combustion efficiency data, which are a quantity of interest for the overarching problem. Various definitions of combustion efficiencies are present in the literature [8-13]. Commonly, it is defined as the ratio of carbon present in unburned flare gases to carbon in products in the form of CO_2 [8]. The current paper uses a progress variable approach [16] to define combustion efficiency. The Progress Variable Model (PVM) is designed to incorporate complex chemical mechanisms with a reduced computational cost. A progress variable, based on chemical enthalpy, in addition to using a mixture fraction and mixture fraction variance, was used to describe the combustion process for LES [17].

As stated previously, the main objective of this dissertation is to validate a code for predictive use of the overarching problem with no experimental data by using available, lower-scale experimental datasets. This was accomplished by constructing a bridge between the experimental data and simulation results in the form of a VUQ analysis. This bridge uses prior information about the models and data, as well as the associated likelihood functions, to get informative posterior distribution. This approach

sheds light on the transfer of information and uncertainties from one brick to another. The numerical simulations were conducted using commercial code, STAR-CCM+ v5.06.010.

Along with validation and uncertainty quantification, a Method of Manufactured Solution (MMS) approach was applied to verify the code. It is an extremely useful verification exercise for finding programming error and ensuring expected behavior of the computer [4]. This step is essential before using any code. Indeed, recent work by Abanto et al. [18] showed that 3 commonly used commercial CFD codes did not display monotonic error convergence for very simple, 2-D test problems for which analytical solutions are easily derived from the Navier-Stokes equations. This work demonstrates that numerically correct behavior of commercial codes, or any code for that matter, cannot be assumed. Though LES simulations are computationally less expensive than DNS, they still carry a substantial cost. For this reason, LES codes are designed for high-performance computing environments.

The University of Utah has a large state-of-the-art high-performance computing facility and a critical aspect for utilizing such assets is the scalability of the underlying numerical methods [19]. Thus, an extensive scaling study was performed during the course of this research.

1.1. Significance of the Research and Original Contribution

The purpose of this research is to provide an approach by which a model can be validated to use for predicting an overarching problem like efficiency of an industrial flare, with no experimental data. This can be achieved by using available lower-scale experimental datasets. This work will make a significant contribution in the estimation of combustion efficiency from industrial flares and this approach can be used for predictive

purposes. Limited studies have been carried out on the estimation of combustion efficiencies from an industrial flare system due to constraints in experimental measurement as well as computational calculations and most of those were performed at lab-scale setups. Because of this lack of experimental data, the proposed models were not validated, thus losing their credibility to predict the efficiency. Hence, it will be helpful to have a method to predict them with certain confidence.

The current work proposes a method to perform interlevel hierarchical validation analysis with uncertainty propagation. It uses a wide variety of experimental datasets to validate a model for an overarching problem. The capability to handle uncertainties in multiple directions was also demonstrated.

1.2. Thesis Outline

The core of this thesis is made up by 3 papers. They are arranged in this thesis as chapters. Chapter 2 is the paper focusing on describing the validation framework along with its application on a buoyant helium-plume case. Chapter 3 is comprised of a paper which focuses on the measurement of combustion efficiency for flares and validation of the model used. The paper in Chapter 4 discusses the overall consistency analysis for an overarching problem using a hierarchical approach. Chapter 5 contains a comprehensive summary of the study and recommendations for the future work. Appendices provide the results for simulations in tabular format, and governing equations in detail.

CHAPTER 2

VALIDATION AND UNCERTAINTY QUANTIFICATION OF A TURBULENT BUOYANT HELIUM-PLUME

Anchal Jatale, Philip J. Smith, Jeremy N. Thornock, Sean T. Smith, Michal Hradisky
(To Be Submitted)

2.1 Abstract

Large-scale buoyant plumes appear in nature in the form of fires, steam vents, etc. Large eddy simulations (LES) were used to model the performance of these plumes for predictive applications. The quantitative validation approach was demonstrated using test data from the 1 m diameter helium-plume at the Sandia National Laboratory. This implemented approach draws on prior information and exploits a consistency requirement among the available experimental datasets and simulations of these sets to quantify the uncertainty in model parameters, boundary conditions, experimental error, and simulation outputs in order to produce predictivity. A total of 15 cases were run with the LES simulator and data were collected at 3 different heights (0.2 m, 0.4 m, and 0.6 m above the helium inlet) in the domain. The simulation results were then subjected to consistency constraints to produce the error bars. The predictions for the time-averaged velocities were consistent with all experimental observations at all locations. The use of the V&VUQ framework also gave a measure of consistency between the model predictions and experimental data. A verification study was also performed along with validation analysis.

2.2. Introduction

Over the last decade, the use of computer simulations has grown to impact not only design and analysis of engineering systems, but it has also been used to change public policy, define safety procedures, and assess legal liability. The growing influence of modeling and simulation and their resulting predictions in day-to-day life demands an extensive analysis of simulation credibility [1]. Users and developers of computational simulation are now facing important questions with regards to assessment of confidence in their predictions since the practical utility of the results of any numerical simulation is proportional to the degree to which error and uncertainty have been quantified. Once quantified, tools can be used to predict results accurately for any scenario, even if such predictions are impossible in experiments. Currently, most available strategies rely on the notion that simulation data should be in close conjunction with experimental results. One such technique is Verification, Validation, and Uncertainty Quantification (V&VUQ). This technique focuses on a combination of 3 processes, which together determines both numerical and physical accuracy. This technique also measures the deviation of the model output from the experiments. Figure 1.1 from Chapter 1 describes this approach. The cyclical nature of the process allows for repeated back-and-forth transfer of information, thus improving the model as a whole by reducing the errors.

The validation process involves building a bridge between the experimental data with their uncertainties and the simulation results with their uncertainties in order to make statements regarding what is known about the real world. The objective of this paper is to build one such bridge by performing a V&VUQ of a turbulent buoyant helium-plume, using Monte-Carlo analysis of LES simulations. Because of the

computational expense of LES simulations, buoyant-flow experiments play an important role in validating a model used for predictions of systems with high complexity, like combustion. Though they sound simple, buoyancy-driven flows provide their own challenges in the form of an inverse energy cascade. Gravitational forces acting on the fluids give rise to density stratifications, which in turn produce Rayleigh-Taylor instabilities [14, 15]. Thus, the chosen 1 m nonreacting helium-plume makes a good case for studying the generation of turbulence due to buoyancy without the complexities of combustion and radiation that would take place in a fire. A V&VUQ framework to perform a systematic validation of the experimental data collected from the Sandia FLAME facility was employed. The approach in the framework used prior information about the models or data and their associated likelihood functions to compute informative posterior distribution. Numerical simulations were conducted using commercial code STAR-CCM+ v5.06.010.

2.3. V&VUQ Frameworks

The modeling and simulation community is actively working to create a complete and detailed framework for performing V&VUQ. References [20–30] highlight various schools of thoughts and progress in this area. All the methods used for VUQ can be placed in 2 major categories: Predictive and Physical [31]. The predictive approach believes that accurate comparison between predictions and field data is the primary indicator of model evaluation. On the other hand, the physical approach focuses on the accuracy of individual elements of the model itself. The framework used in this paper most closely resembles the predictive approach. It draws on prior information and exploits a consistency requirement among the available experimental datasets and the

simulations of these sets, thereby quantifying the uncertainty in model parameters, boundary conditions, experimental error, and simulation outputs to produce predictivity.

All of the V&VUQ frameworks discuss uncertainties in the predicted results. These uncertainties are commonly classified according to their core: Aleatoric or Epistemic [32-37]. Other ways to categorize uncertainties are based on their source [38], such as parameter uncertainty, model inadequacy, algorithmic uncertainty, experimental uncertainty, interpolation uncertainty, etc.

Oberkampf et al. developed a comprehensive framework for model validation and verification [21]. This proposed framework coincides with predictive uncertainty and is known as Probability Bounds Analysis (PBA) [39-41]. Within the PBA framework, all the uncertainties are classified according to their mathematical structure before estimating the numerical uncertainty. Methods such as Richardson Extrapolation [3], Discretization Error Transport Equations [42, 43], and Residual/Recovery methods in finite elements [44,45] may be used. Because the estimated values are not completely accurate within this method, upper and lower bounds must be applied. The total uncertainty in the framework is a combination of numerical error, error in input parameters, and model form uncertainties. The input uncertainties are circulated through the model using Monte-Carlo sampling methods. The model uncertainty is quantitatively estimated at the scenarios where experimental data are available [39, 46-48], then extrapolated to the other points of interest.

Another widely-recognized framework is provided by the American Society of Mechanical Engineers (ASME) [24]. In contrast to the PBA framework, here, uncertainties in the experiments are processed in the same way as uncertainties in the

simulation results. The uncertainty in each error source is estimated as the standard deviation of all possible errors. Thus, a range for modeling errors is found. The main objective of this methodology is to calculate validation uncertainty, which is defined as:

$$U_{val} = \sqrt[2]{U_{num}^2 + U_{input}^2 + U_{exp}^2} \tag{2.1}$$

where U_{num} is the numerical uncertainty calculated using code and solution verification techniques similar to the first framework; U_{input} is the uncertainty in the input parameters of the model, measured by the Sensitivity Coefficient method or Monte-Carlo sampling methods; and U_{exp} is the uncertainty in the experimental results, determined using well-accepted techniques [24].

Recently, V Romero [20] proposed a new validation approach known as Real Space validation. This approach works backwards from an end objective to estimate the accuracy of predictions. It adopts and refines some elements from the literature, while also constructing other elements. There are some more frameworks available in the literature, most of which are based on Continuous Monte-Carlo [49] and Polynomial Chaos [50, 51].

The validation framework used in this paper is inspired by Bayarri et al. [22] and Frenklach et al. [52-54]. Bayarri et al. framework is based on the Bayesian approach. The purpose of this framework is to produce tolerance bounds for model validity, using Bayesian and likelihood techniques. It provides a quantitative understanding of the model validation. The accuracy of the model is estimated by comparison with field data. This methodology was combined with the Data Collaboration (DC) approach proposed by

Frenklach et al. [52]. The main goal of DC is to provide quantitative and reliable uncertainty bounds on predictions from simulations [53-54].

2.4. Mathematic Formulation (Large Eddy Simulation)

The LES-based model in STAR-CCM+ solves the flow equations (velocity and pressure) in segregated patterns. In this model, pressure and velocity are coupled using the Standard Semi-Implicit Method for Pressure Linked (SIMPLE) algorithm [55]. These compressible Navier-Stokes equations are closed using subgrid-scale turbulence models, which employ the Boussinesq hypothesis [56] to provide the relationship between the turbulent flux and subgrid-scale turbulent viscosity, μ_t. The turbulent viscosity in turn is estimated by the WALE (Wall-Adapting Local-Eddy Viscosity) subgrid-scale model [57].

2.5. Application of V&VUQ on Buoyancy-Driven Helium-Plume Flow

2.5.1. Verification

As described earlier, the verification process checks the accuracy of the solution of a mathematical model in computational applications. It gives considerable attention to numerical accuracy, which is important in model validation [58,59]. It has 2 important parts: code verification and solution verification. Code verification provides evidence that the codes are free from error and behave mathematically as the programmer intended. It is also useful for examining the kinetic energy conservation properties of a code. The discretization error associated with conservation of kinetic energy is closely associated with the grid, CFD algorithm, and choice of the discretization scheme. Thus, this type of verification activity helps illuminate the costs (in terms of error) associated with various

numerical schemes and helps identify which schemes are appropriate for a given application. Study of the conservation and convergence of kinetic energy is also important from an LES standpoint as the total amount and transfer of kinetic energy among the length of the scales controls the mixing of species in a system. This study was performed using the Method of Manufactured Solution (MMS) method. It was simultaneously used to compare 2 meshing techniques available in the code.

In contrast, solution verification helps in estimating and reducing numerical uncertainty in the intended-use regime providing results that are directly usable in any future analysis. For the helium-plume case, a grid refinement approach was used to reduce the numerical uncertainty from the solution and to make it suitable for use in validation studies.

Verification is not only confined to accuracy of the code and solution, but in the case of parallel computing, scalability of the code for intended application is also important. For this reason, an extensive scaling study was performed for helium-plume application. Not only did this help reduce the computational cost of the simulations, it allowed the user to run simulations efficiently.

2.5.1.1. Code Verification

The applied MMS approach allow for arbitrary complexity in the solutions. A manufactured solution, or set of manufactured solutions, is created to verify all parts of the equation [60]. In this paper, STAR-CCM+ was verified using the following MMS:

$$u(x,y,t) = 1 - Acos\big(2\pi(x-t)\big)\sin\big(2\pi(y-t)\big)\,e^{-2\vartheta t}, \tag{2.2}$$

$$v(x,y,t) = 1 + Asin\big(2\pi(x-t)\big)\cos\big(2\pi(y-t)\big)\,e^{-2\vartheta t}\,, \tag{2.3}$$

where A is the amplitude and ϑ is viscosity. These expressions for velocity are convenient because they do not produce any extra source terms while still allowing a non-trivial flow field.

The verification was performed for 2 meshing schemes: the Polyhedral and the Trimmer. A polyhedral scheme, as the name suggests, creates a mesh with polyhedral shaped cells whereas the trimmer scheme ensures that the resulting mesh is composed primarily of hexahedral cells with trimmed cells next to the surface. Trimmed cells are hexahedral cells with one or more corners and/or edges removed. A 2-D laminar problem with constant density, periodic boundaries, segregated flow solver (Low-Mach, Pressure Projection), and implicit unsteady solver (2^{nd} order) was simulated. In addition to verifying that the code had been properly implemented (bug-free), each test run had its own purpose as well. Table 2.1 shows the cell count for different polyhedral and trimmer meshes used for this study. Both the trimmer and polyhedral meshes were examined by running four cases and comparing the results to the exact solution. Figure 2.1 shows the result for Case 1, which examines the convergence error of the convection term (spatial derivatives) only and minimizes the temporal error. The error in the x and y component of velocity were plotted with respect to Δx. Note that the value of Δx for each grid was calculated as the minimum distance between node points across the mesh. It is observed that for both meshes, the error decreases with refinement. In polyhedral mesh, however, the error does not reach monotonic convergence and appears to display close to 1st order convergence. The trimmer mesh is more consistent, with the error converging close to 2^{nd} order. Thus, the trimmer mesh has a higher-order convergence rate than the polyhedral mesh for the convection term.

Table 2.1: Cell Count for Meshes Used in Code Verification

Polyhedral Mesh cell count	Trimmer Mesh cell count
133	100
505	400
1890	1600
12858	10000
22756	17956

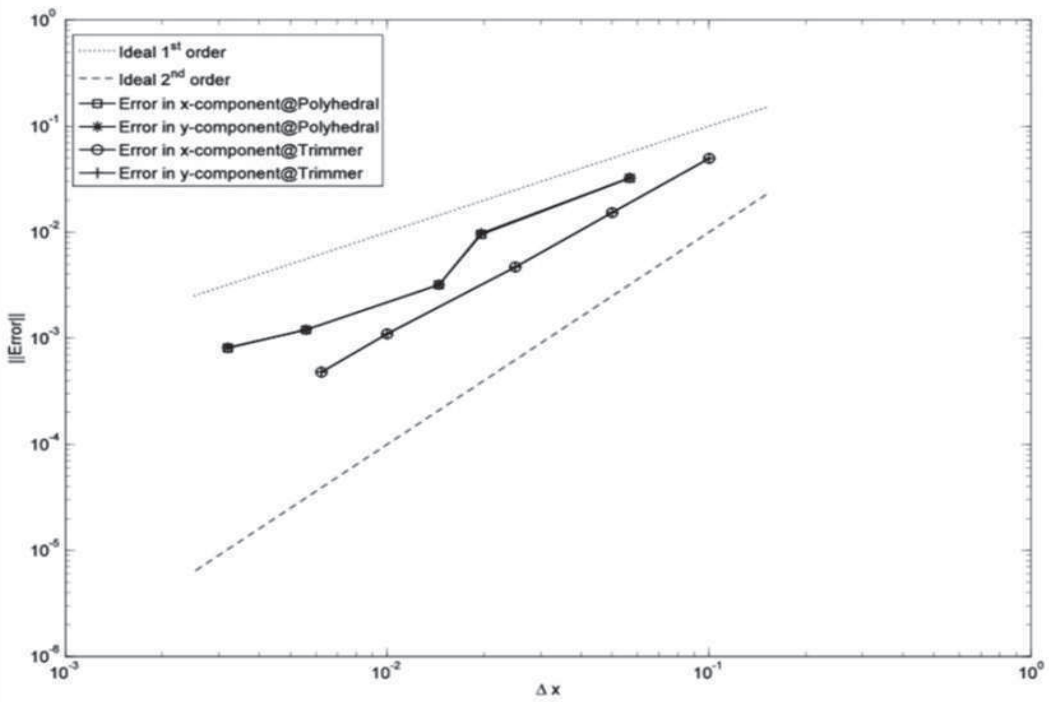

Fig 2.1: Case 1- Execution of One Time Step, with $\varepsilon\Delta t$, Where ε is a Very Small Number and $\mu = 0$.

The results for Case 2 (Figure 2.2) were very similar to Case 1, resulting in non-stabilized convergence (close to 1st order) for the polyhedral mesh and monotonic error convergence (close to 2nd order) for the trimmer mesh. The purpose of this case was to examine the convergence error of the convection and diffusion terms together (spatial derivatives) in order to minimize the temporal error. One sees minimal difference in the results from the previous case, as the diffusion term is multiplied by the viscosity of air, a relatively small number compared to the magnitude of the error.

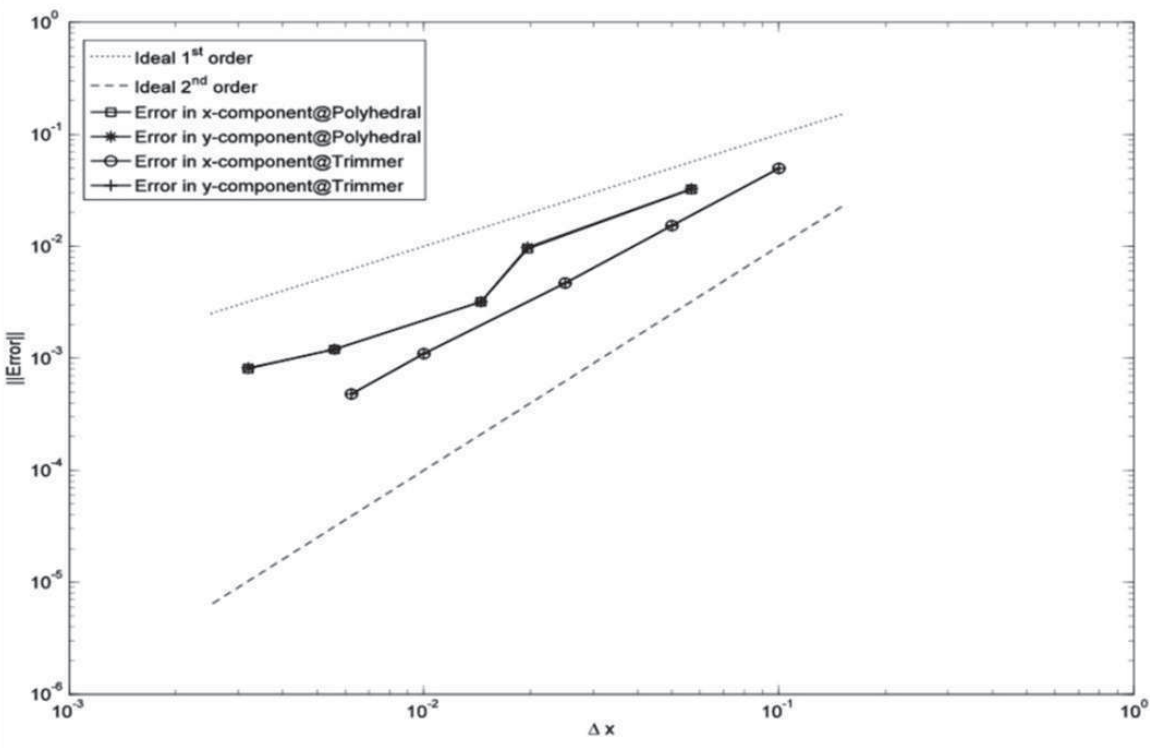

Fig 2.2: Case 2- Execution of One Time Step, with $\varepsilon\Delta t$, Where ε is a Very Small Number and μ = Air Viscosity.

The objective of the next case in the study was to understand the energy-conserving properties of the numerical scheme. This error convergence is particularly important in LES modeling. Figure 2.3 shows that for both meshing schemes, the error convergence has not stabilized with a successively finer mesh size. Thus, it is difficult to determine the order of convergence. However, we observed that the magnitude of error for the trimmer mesh is less than that of the polyhedral mesh. The last case in the sequence was to examine the convergence error of the entire scheme, both temporal and spatial. The results for this case are given in Figure 2.4, with error convergence of velocity components plotted against Δx. Again, as in Case 3, non-monotonic error convergence is observed, with the trimmer mesh having a smaller magnitude of error.

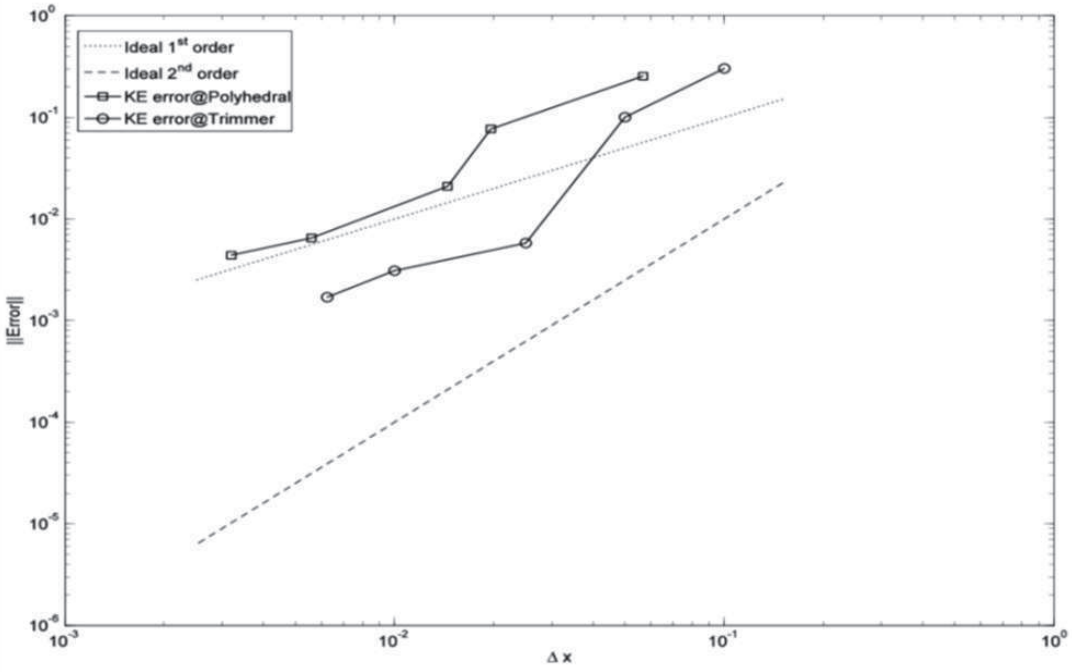

Fig 2.3: Case 3- Multiple Time Steps (Until t = 1 Second), with Δt Computed by a Standard Stability Condition and μ = 0

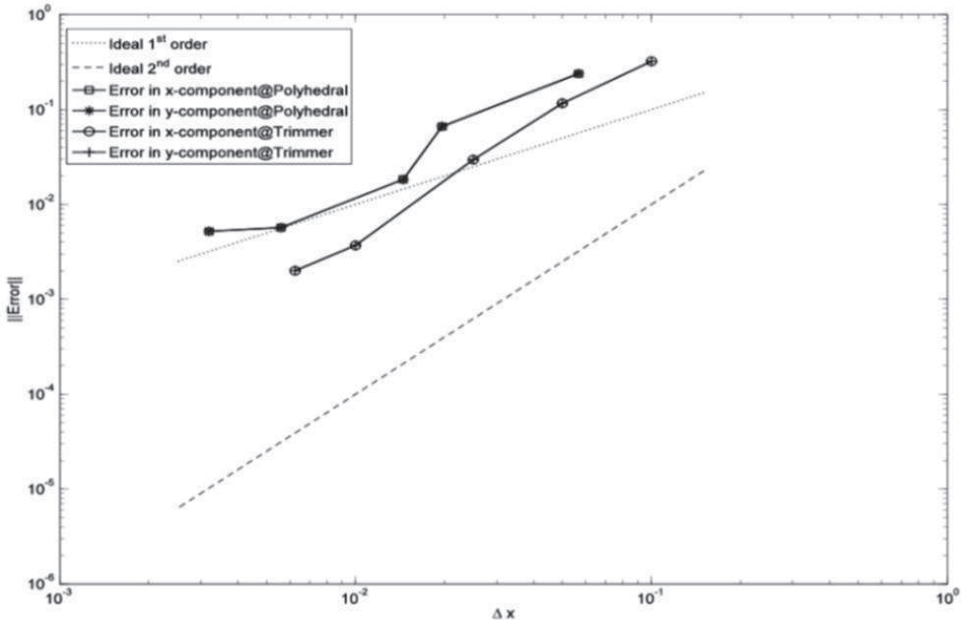

Fig 2.4: Case 4- Multiple Time Steps (Until t = 1 Second), with Δt Computed by a Standard Stability Condition and μ =Air Viscosity

2.5.1.2. Scaling

Large-eddy simulation carries a substantial computational cost, and thus, codes are designed for high-performance computing environments. A critical aspect of using a high-performance computing environment is its scalability [25]. This paper deals with 2 types of scaling processes: strong and weak scaling. Strong scaling is helpful in finding an optimum number of processors for a given problem and reducing its computational cost. It measures the computational speed-up by varying the number of processors for a constant size problem. Weak scaling analysis involves varying the problem size and the number of processors together, such that the execution time for each problem is nearly the same. This indicates how the computational work due to parallelism overhead (communication) increases. Information on strong and weak scaling helps a user run a simulation efficiently. Figure 2.5 shows a schematic and models used in the simulation for both strong and weak scaling.

Models

- Implicit unsteady (2nd order temporal discretization)
- Multicomponent gas
- Nonreacting
- Segregated Flow (Bounded central differencing)
- Segregated Species (2nd order)
- Segregated Fluid Isothermal
- Ideal Gas
- Large Eddy Simulation
- WALE (Wall-Adapting Local-Eddy Viscosity) Subgrid-scale
- All y+ Wall Treatment
- Gravity

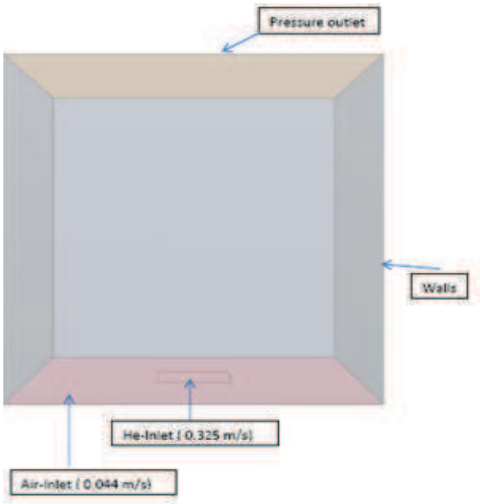

Fig 2.5: Details of Simulation Used for Scaling Studies: Models and Schematic

Table 2.2 shows the list of cases run for the scaling studies. Strong scaling results show that as problem size increases, better scaling capabilities are obtained (Figure 2.6). In fact, for the biggest problem size, good (near linear) scaling is achieved for up to 768 processors, as compared to linear scaling of a mere 48 processors for the smallest problem size. Figure 2.7 shows the results of the weak scaling studies. It can be observed that with a decrease in work load on a processor, the scaling improves. Yet with a very small load on a processor, communication delay comes into play. Thus, we need an optimum processor load for good performance.

2.5.1.3. Solution Verification

This verification step helps reduce numerical uncertainty and ensures that a converged solution is used for the validation steps. To achieve the aforesaid goals, a grid refinement study was performed on the helium case. This study was used to find an optimum mesh size that strikes a balance in size of the problem and accuracy of the results.

Table 2.2. Weak and Strong Scaling Cases

Strong Scaling		**Weak Scaling**	
Serial No.	Size (In terms of number of cells)	Serial No	Average no. of cells per processor
1	1 million	WS1	10,416 cells
2	2 million	WS2	20,833 cells
3	4 million	WS3	41,666 cells
4	8 million	WS4	83,333 cells
5	16 million	WS5	166,666 cells
6	32 million	WS6	333,333 cells

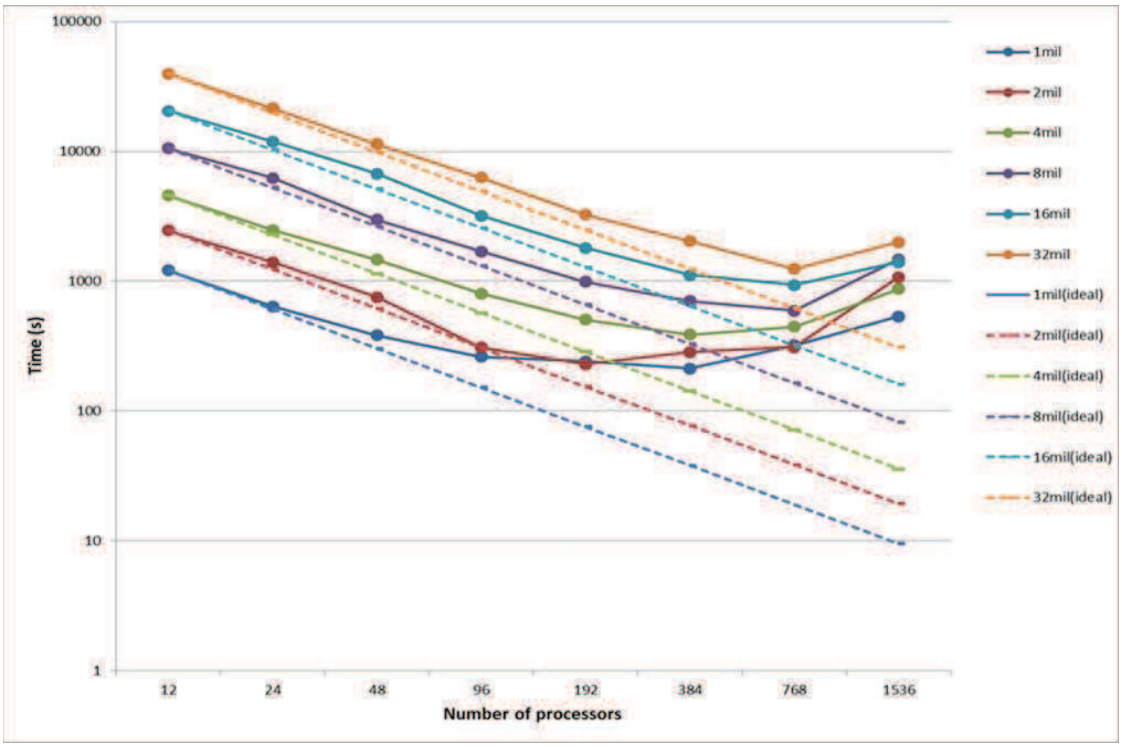

Fig 2.6: Strong Scaling Results for Nonreacting Helium Case

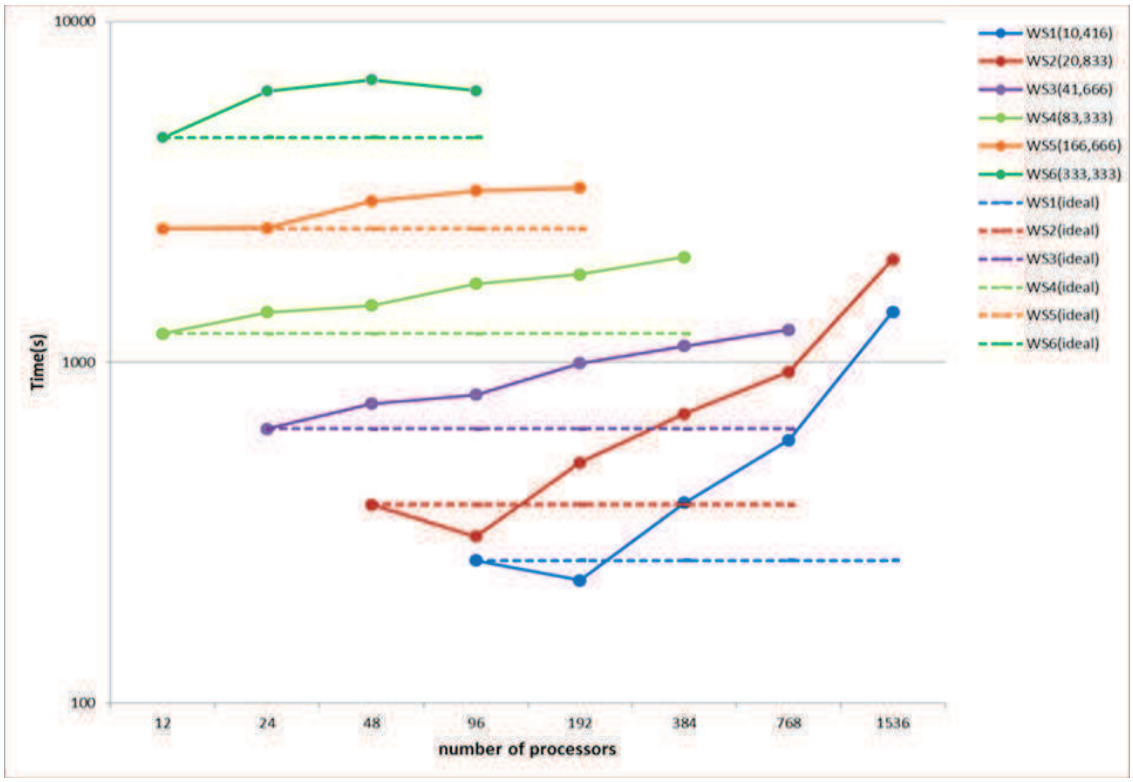

Fig 2.7: Weak Scaling Results for Nonreacting Helium Case

2.5.1.3.1. Experimental and Simulation Setup

The experimental data used for this step were collected at the SANDIA National Laboratories in their Fire Laboratory for Accreditation of Models by Experimentation (FLAME) Facility (Figure 2.8a). The central chamber is a 6.1 m^3 enclosure with a 2.4 m square chimney for outlet. The plume source at the center is at an elevation of 2.45 m from the floor. The facility is enclosed on all sides except for inlet air ducts. The diverters, screens, and honeycombs are placed such that the inlet air forms an annular low-velocity inlet flow surrounding the helium-plume [4,61] . As seen in Figure 2.8b, the experimental setup was simplified into a 4 m^3 enclosure with the helium inlet of 1 m diameter at 0.25 m height from the bottom. This size of enclosure was created after comparing the effects of wall distance on the airflow to find an optimum domain size

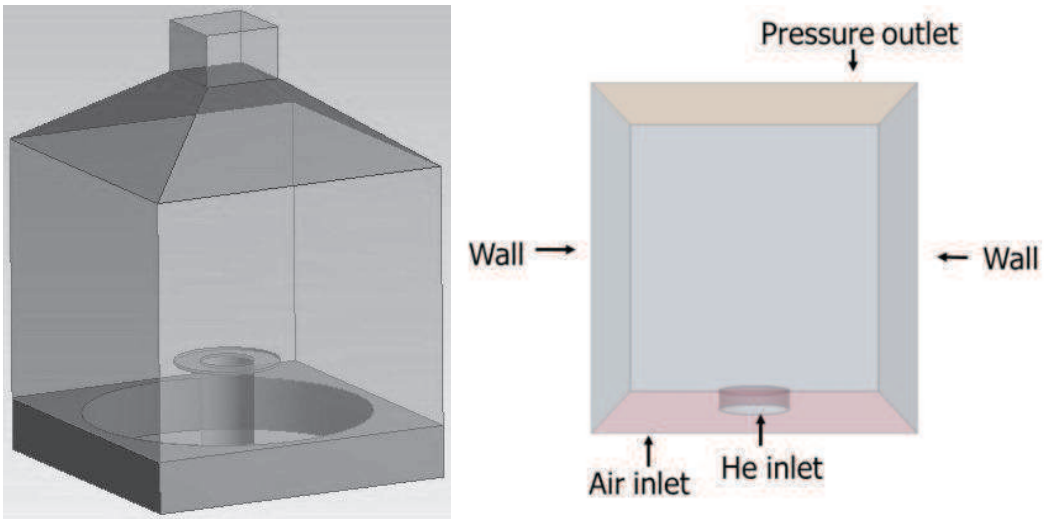

Fig 2.8: Flame Facility at Sandia National Laboratories a) Schematic b) Simulation Domain

with regards to run time and the accuracy of the results. The ground in the simulation was an inlet for airflow and its characteristics were calculated based on the mass balance of the original airflow specs.

The experimental mixture of helium, acetone, and oxygen with the molecular weight of 5.45 g/mol was also used in the simulation. The side surfaces were modeled as walls and the top as a pressure outlet. The domain was meshed using a trimmer meshing scheme. The large, state-of-the-art cluster, Ember [62], was used for simulations. The unsteady LES simulations were set up to run implicitly with a segregated flow solver. For the first 2 seconds of flow, a time step of 0.05 seconds was used to set up a flow filed in the domain. Then the step size was reduced to 0.0005 seconds for the next 3 seconds, thereby allowing for the computational flow transitions to reach quasi-steady flow conditions. Results from the next 5 seconds of simulation were processed to produce time-averaged quantities. The statistical stability was checked before using the results in this analysis.

2.5.1.3.2. Grid Refinement Study

To discover an optimum mesh size—not too large, but still able to give a converged solution for future use—a grid refinement study was performed. For this purpose, a case was run for 6 different mesh sizes, ranging from 2 million cells to 20 million cells. In each simulation, data were collected at 0.2 m, 0.4 m, and 0.6 m above the plume inlet. Favre-averaged vertical velocity values from 5-10 seconds of flow time were collected and compared. Figure 2.9 shows the mesh with 8 million cells. For the current study, values from a 20 million cell mesh were considered as base values. Measured velocities for 65 radial locations at each height were compared and an average error with respect to the base values was calculated. Figure 2.10 shows the comparison between values at 3 heights for different meshes. The results from this study provided an optimal mesh size to be used for simulation in validation studies. The simulations were run on parallel computers, using the findings from the scaling studies.

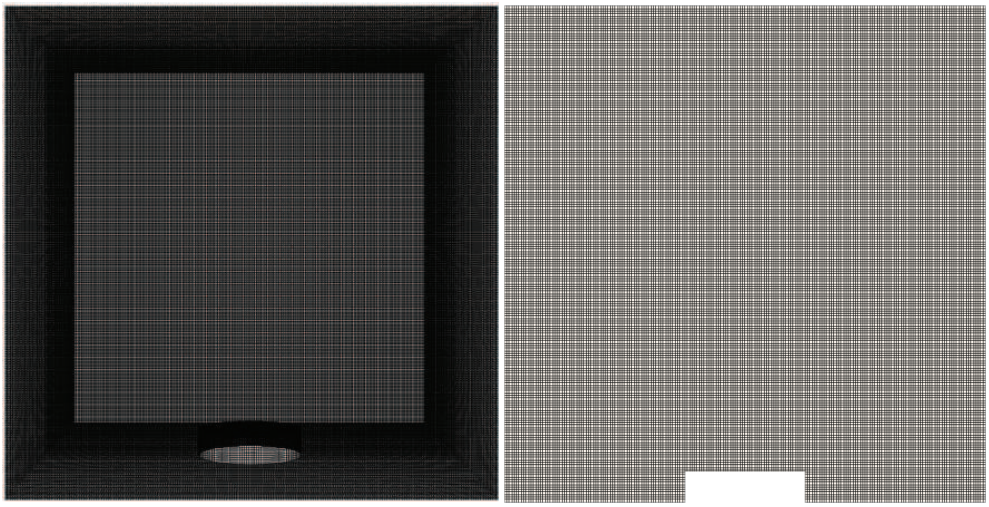

Fig 2.9: 3-D and Projected View of the Mesh, Respectively

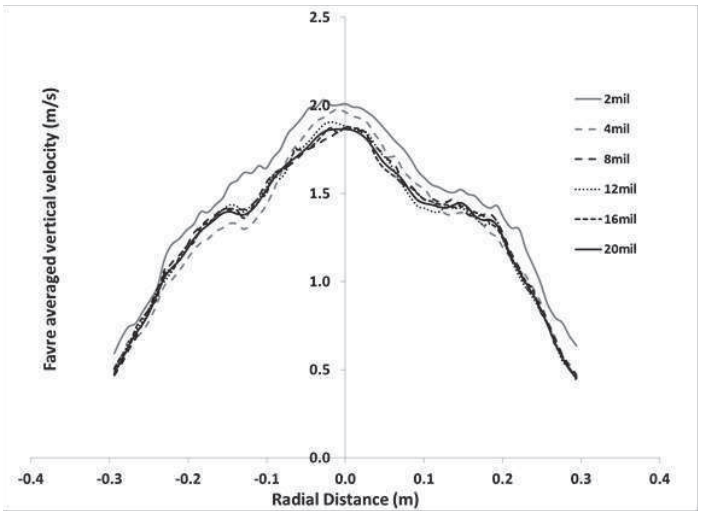

a)

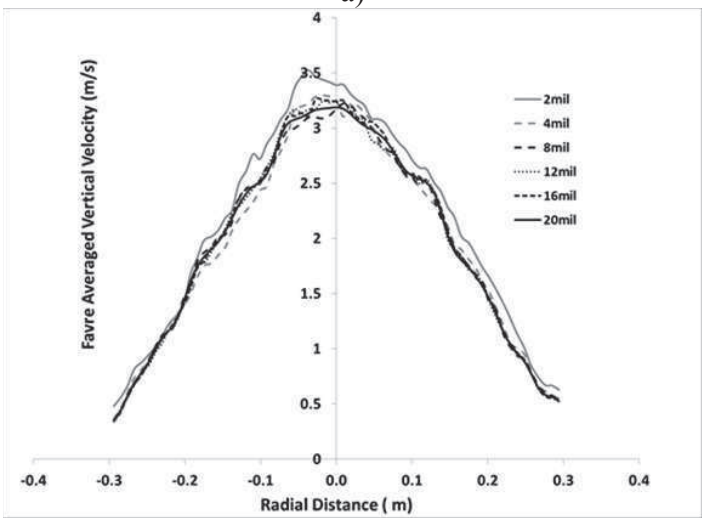

b)

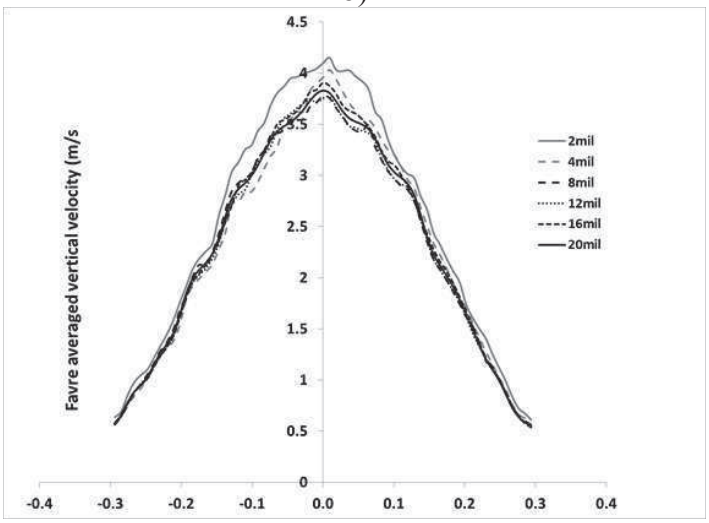

c)

Fig 2.10: Favre-Averaged Vertical Velocities for Different Meshes at a) 0.2 m b) 0.4 m c) 0.6 m Above the Helium Inlet

Table 2.3 shows that with increasing mesh size, error in the results decreases. It also gives the CPU hours required for each case. It can be observed that after 8 million cells, increase in cell size does not change the results significantly though CPU hours continue to rise. Thus, 8 million cells may be termed the optimum mesh size for this case. Also, the error for this mesh size (~1.9%) is in the acceptable range.

2.5.2 Validation and Uncertainty Quantification

2.5.2.1. Validation Framework

This step is important for providing quantitative and reliable uncertainty bounds on predictions from the simulations. The 6-step framework [31,63] was combined with a Monte-Carlo sampling approach to provide upper and lower bounds of the prediction. This section will define the steps of the framework, along with their application on helium-plume simulations.

Table 2.3: Average Error for Different Mesh Sizes at 3 Heights

Mesh Size	**Average Error % at 3 Heights Above the Helium Inlet**			**CPU Hours**
	0.2 m	**0.4 m**	**0.6 m**	
2 million	8.75	9.87	9.14	29,500
4 million	4.42	3.95	3.71	55,600
8 million	1.94	1.90	1.81	86,400
12 million	1.77	1.72	1.70	115,200
16 million	1.65	1.50	1.55	172,800

All the variable types and parameters present in a known system were classified into four major categories for the purpose of the VUQ study in this paper:

- *Active variables*: These subsets of parameters have a measurable influence on the property of interest. They consist of both model parameters and scenario parameters.
- *Design/Manipulated variables*: These are sets of variables that are changed by the experimentalists to create various scenarios for experiments—for example, locations of data collections in a system. In the terms of validation studies, these are the variables that distinguish between dataset units.
- *Controlled variables*: A variable that is kept fixed during the course of the experiment and strongly influences values is known as the control variable. It is held constant in order to test the relative impact of an independent variable. These variables can also be known as inactive scenario parameters.
- *Extraneous variables:* All other variables present in the systems are known as extraneous variables. They may introduce noise but do not systematically bias the results.

The applied framework is as follows:

Step 1: A list of model inputs and parameters with uncertainties or ranges (Input/Uncertainty (I/U) map) [64] was created.

In this step, the model inputs and parameters were listed and ranked according to their impact on the prediction error. The list also included the uncertainties for each input and their current treatment status in the model. This dynamic I/U map could be revisited and updated after other steps. Table 2.4 shows the I/U map for a helium buoyant plume.

Table 2.4: I/U Map for 1 m Helium-Plume

INPUT		IMPACT	UNCERTANITY	CURRENT STATUS
Geometry	Pipe diameter	1	Unspecified	1 m
	Wall distance from inlet	3	Unspecified	Sensitivity analysis/optimized
	Outlet height	1	Unspecified	optimized
Input	Helium velocity	5	20 %	controllable
	Air co-flow	5	20 %	controllable
Model Parameters	Turbulence Sc number	4	[0.4 – 1.894]	Set by modeler
Numerical Parameters	Mesh	2	Unspecified	Convergence/speed compromise
	Boundary conditions	1	Unspecified	Fixed
	Initial conditions	1	Unspecified	Fixed

The impact factors were estimated based on prior experience, as well as sensitivity analyses and tuning. The distance of the inlet from the wall was reduced—as compared to the actual dimensions of the facility—to a point where it did not affect the final results. This also helped in the reduction of the overall computational cost. Also, an optimum mesh size was finalized before running the cases. As seen in the I/U map, 2 parameters were given impact factor 5, and thus, an analysis was first performed with those 2 scenario parameters, followed later by a model parameter with impact factor 4.

One of the parameters chosen for this analysis was turbulent Schmidt number. This parameter describes the momentum/scalar interactions in the flow. The modeling difficulty related to this parameter is highlighted by the wide range of values used in the literature [65- 69]. Xin et al. [80] have used 0.4 for Sc_t to create better predictions for the simulation of a methane pool fire and stated that Sc_t does not have a significant influence. On the other hand, Jiang and Campbell [68] have reported a wide range (0.2 to 0.85) of values and highlighted their effect on the flow field predictions. Wen et al. [69] and Zhang et al. [66] give completely different recommendations, claiming the choice of Sc_t is unimportant, compared with other variables. Due to these varied recommendations, turbulent Schmidt number was selected for the investigation of an optimum range and the effect on the results for the helium-plume simulations.

Step 2: Evaluation criteria were defined.

In this step, evaluation criteria were specified for model output. Based on the experimental data, favre-averaged centerline velocity at 3 different heights (0.2, 0.4, 0.6 m) from the inlet was decided to be an evaluation criterion. At these heights, the data for 65 radial locations were averaged at 2 perpendicular single cell rows in x and y direction.

This experimental procedure and data collection also helped to decide the range of chosen active variables.

Step 3: Using the collected data, a Design of Experiments (DOE) was created.

Amidst all the standard methods to create DOE, this paper creates optimum-sized DOE by strategically filling the variable space to capture detailed information in the most impactful regions. A DOE was prepared for both 2 active variable (2-D) and 3 active variable (3-D) cases. Table 2.5 shows the comprehensive design matrix for the helium-plume.

Step 4: The computer model output was approximated.

Validation process requires multiple code evaluations. The high cost of each LES simulation combined with the Monte-Carlo sampling procedure for the consistency test necessitated the use of an LES surrogate. Creating a good surrogate model is an important step in validation, since a bad surrogate model can insert additional errors and create relationships between variables which are not present in reality. These models must not only be a good mathematical fit but also follow the real physics accurately. The pioneers of surrogate models were Box and Wilson [70] who developed an approach known as Response Surface Methodology (RSM) in which polynomial surfaces are used to represent output. While generally reliable and widely used, a polynomial can insert additional information in terms of trends and physics between 2 points where data are sparse. This drawback was overcome in the current paper by the use of a flexible interpolation method, Delaunay Triangulation. In addition to being computationally less expensive, Delaunay Triangulation ensures boundedness, without being affected by the sampling order [71, 72].

Table 2.5: Design of Experiment for Helium-Plume

Design matrix for 3-D case				**Design matrix for 2-D case, Sc_t=0.9**		
Sim#	**V He (m/s)**	**MF Air (kg/s)**	**Sc_t**	**Sim#**	**V He (m/s)**	**MF Air (kg/s)**
1	0.29	0.355	1.894	1	0.29	0.355
2	0.36	0.355	1.894	2	0.36	0.355
3	0.29	0.755	1.894	3	0.29	0.755
4	0.36	0.755	1.894	4	0.36	0.755
5	0.29	0.355	0.508	5	0.264	0.555
6	0.36	0.355	0.508	6	0.385	0.555
7	0.29	0.755	0.508	7	0.325	0.208
8	0.36	0.755	0.508	8	0.325	0.901
9	0.29	0.555	0.8	9	0.325	0.555
10	0.385	0.555	0.8			
11	0.325	0.208	0.8			
12	0.325	0.901	0.8			
13	0.325	0.555	100000			
14	0.325	0.555	0.4			
15	0.325	0.555	0.8			

This method is also superior in feature capturing, since all original data points are located on the surrogate surface only.

Step 5: The consistency was measured.

This step drew on prior information and exploited a consistency requirement among the available experimental datasets and simulations of such sets to quantify the uncertainty in model parameters, boundary conditions, and experimental error and simulation outputs to produce predictivity [73]. Using this approach, the uncertainty interval for the data was obtained, which in turn was used as the likelihood in the consistency analysis. The most sensitive parameters were then identified and used in the subsequent quantification of predictivity. The consistency constraint used to measure and produce a posterior uncertainty consistent with all experimental and simulation data was defined as [52-54]:

$$\begin{cases} C_{\aleph} = \min \gamma \; subject\ to\ constraints: \\ \beta_i \geq x_i \geq \alpha_i \,, for\ i = 1, \ldots\ldots, n \\ (1-\gamma)u_e \geq |y_m(x) - y_e| \geq l_e(1-\gamma), for\ each\ e \in \aleph \end{cases} \tag{2.4}$$

where α_i , β_i are upper and lower uncertainty bounds of input parameter x_i , y_m is the model value, and y_e is the experimental value. u_e and l_e are the upper and lower bounds of experimental uncertainty or deviations. Equation 2.4 makes sure that all simulations are bounded by their individual experimental uncertainty. The term (1- γ) is added to the equation to make sure that we can quantify the consistency of the model. Each dataset point is checked through the constraint and value for (1- γ) is stored. C_D denotes the largest value of (1- γ). It gives a measure of an overall consistency of the dataset. The smaller value of C_D corresponds to better consistency.

The major difference between Data Collaboration (DC) and the consistency test used here was that it uses a pseudo-random selection of points (the Monte-Carlo method) to solve a similar set of equations, rather than the domain decomposition iterations of DC. The consistency test employs the following steps:

1) The range of active variables was specified.
2) Experimental data were sampled in order to find any uncertainties present. This was computed through mean and standard deviation with a user-specified confidence range.
3) Using Monte-Carlo sampling, a feasible region for active variables was obtained between the provided ranges.
4) The model was then evaluated at each of the sample points and for each of the experiments or scenarios.
5) A consistency analysis was performed by subjecting the results to the constraints (Equation 2.4). This step revealed how well the evaluated values matched the experimental values. For a point to be called consistent, it needed to satisfy the inequalities for each of the experiments.

Step 6: Information was fed back into the current validation exercise and fed-forward into future validation activities.

This step used the results from Step 5 to improve the model, as well as to refine the aspects of the validation process. The results were analyzed to highlight the impact region in variable space, and thus helped in populating the DOE points. The UQ results for the current model could also be used to predict the validity of future models, for which very sparse or no experimental data are present [74].

2.5.2.2. Results and Discussion

The framework described above was applied to buoyancy-driven, nonreacting helium-plume flow to validate the experimental data. Each step was followed in a systematic manner and time-averaged values were calculated from the simulations. Based on the grid refinement studies, a mesh size of 8 million cells was used for the validation studies. As mentioned in grid refinement studies favre-averaged vertical velocity values from 5-10 seconds of flow time were collected. This time interval of 5 seconds provided statistical reliability and was finalized by calculation of moving point average at the centerline point. The knowledge gained through the scaling studies was instrumental in running all the simulations on 360 to 420 processors. Figure 2.11 illustrates how the plume developed with time. It was observed that the helium-plume not only showed a significant number of structures, but it was numerically stable for long run times. This result also showed the presence of puffing phenomena. The rate of puffing is an important feature for the current application, as it is responsible for feeding oxygen to the plume flow. In order to characterize the puffing rate and compare it with previous studies in the literature, the centerline velocity at height 0.4 m for case 15 was measured.

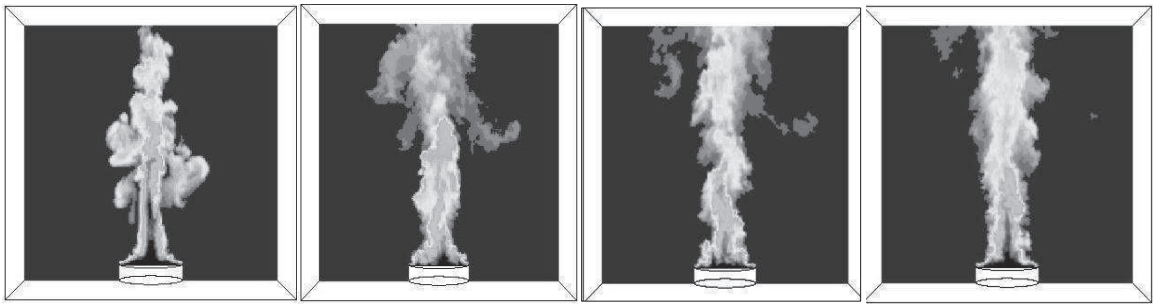

Fig 2.11: Greyscale Image of the Density at a Plane in the Helium-Plume Simulation at (from Left to Right): 1.86, 3.22, 4.07 & 5.04 Seconds

A periodic fluctuation was observed in the flow, and a power series spectrum of the results (Figure 2.12) showed a dominant puffing frequency of 1.44 sec^{-1}. Noted research from O'Hern et al. [4] and Cetegen et al. [75] have reported a puffing frequency of 1.37 sec^{-1} and 1.40 sec^{-1} , respectively, for similar configurations. Also, an analytical work in literature [76] proposed that puffing frequency may be related to the plume diameter as $1.5\sqrt{D_p}$. For a 1 m helium-plume, this relation gives a frequency of 1.5 sec^{-1}. The simulation value of 1.44 sec^{-1} is within 5% of all these literature values. After converting the simulation results into the experimental data format, a consistency analysis was performed using the Monte-Carlo Consistency test. First, a 2-D analysis was completed varying only co-flow of air and inlet helium velocity. 50,000 random points were selected within the range of these variables and results for each point were tested through the consistency constraint.

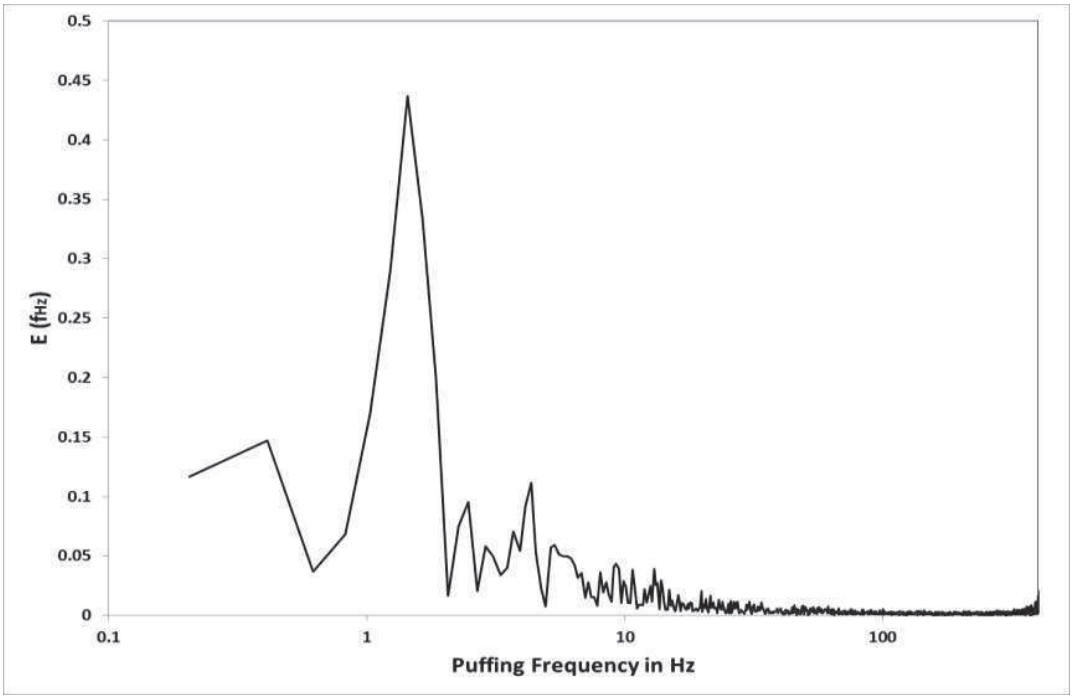

Fig 2.12: Power Spectrum of the Time Series, Showing Dominant Puffing Frequency of 1.44 sec^{-1}

Figure 2.13 shows all the points in the variable space which satisfy the constraints. The X and Y axes, respectively, show the range of helium inlet velocity and air co-flow. The color scheme is a value of (1- γ), with 0 being the most consistent point and 1 being the edge of consistency. Figure 2.14 shows the same result in the form of error bars. It shows the experimental data as well as the model data and the common consistent region for all 3 heights. Table 2.6 shows the range of parameters over which the dataset was consistent along with the most consistent point and overall consistency measure of the dataset for 2-D analysis.

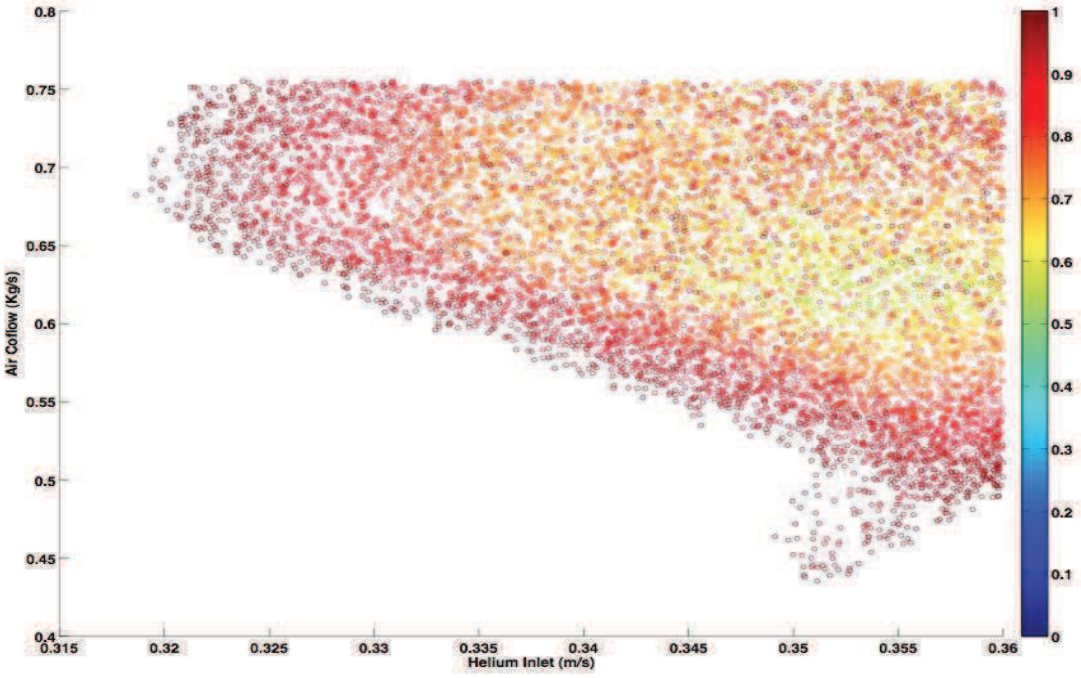

Fig 2.13: Consistency Space for 2-D Helium-Plume Case

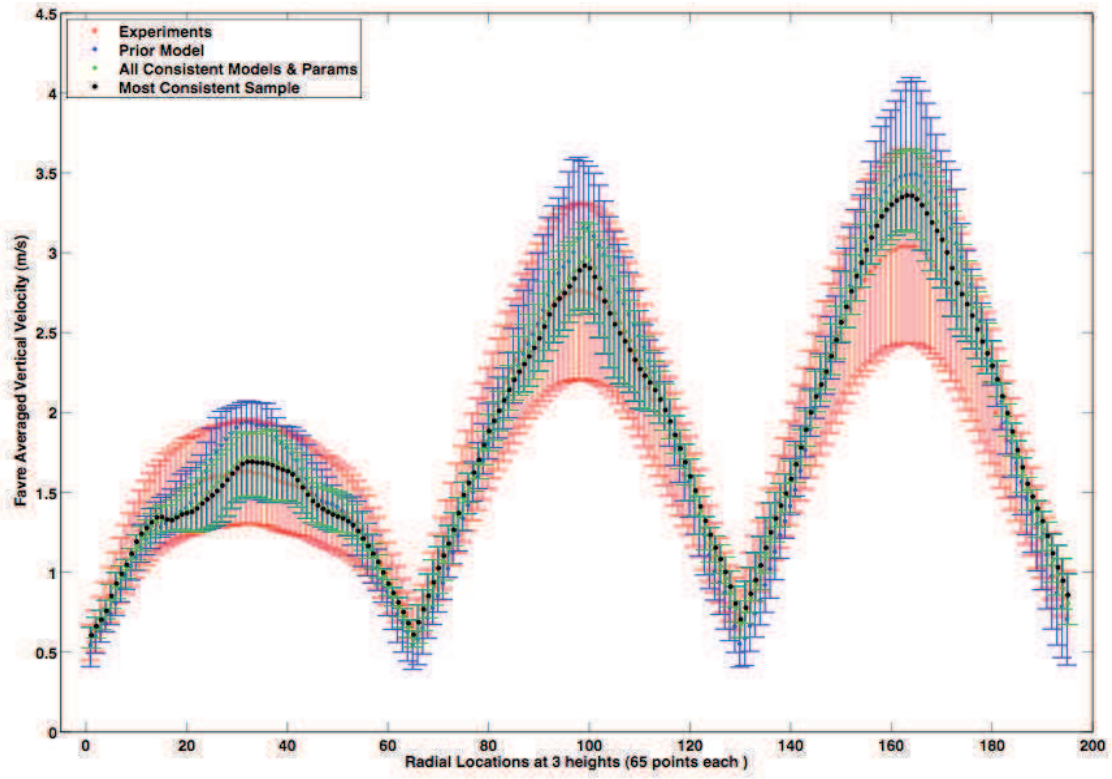

Fig 2.14: Error Bars for 195 Points at 3 Different Heights to Show the Consistent Space for 2-D Case

Table 2.6: Results for 2-D Analysis

Helium inlet range for consistent data	0.318 m/s to 0.36 m/s
Most consistent helium inlet value	0.341 m/s
Air co-flow range for consistent data	0.428 Kg/s to 0.75 Kg/s
Most consistent air co flow value	0.52 Kg/s
Overall consistency measure, C_D	0.528

The design matrix of the 2-D case was expanded with the introduction of a model parameter, turbulent Schmidt number (Sc_t), into the mix. An analysis similar to the 2-D case above was performed for the 3-D case. The results and findings from the 2-D case were used to improve the matrix. Again, 50,000 random points were selected within the range of these variables and results for each point were put to the consistency constraint. Table 2.7 shows the range of parameters over which the dataset was consistent along with the most consistent point and overall consistency measure for 3-D analysis. Figure 2.15 shows all the points in the variable space which satisfy the constraints. The X, Y, and Z axes respectively show the range of helium inlet velocity, air co-flow, and turbulent Schmidt number. The color scheme is the same as in the 2-D case. Figure 2.16 shows the comparison between the experimental data and the model data. The common consistent region for all 3 heights is also shown.

Table 2.7: Results for 3-D Analysis

Helium inlet range for consistent data	0.32 m/s to 0.36 m/s
Most consistent helium inlet value	0.349 m/s
Air co-flow range for consistent data	0.355 Kg/s to 0.70 Kg/s
Most consistent air co flow value	0.46 Kg/s
Sc_t range for consistent data	0.61 to 1.89
Most consistent Sc_t value	0.99
Overall consistency measure, C_D	0.651

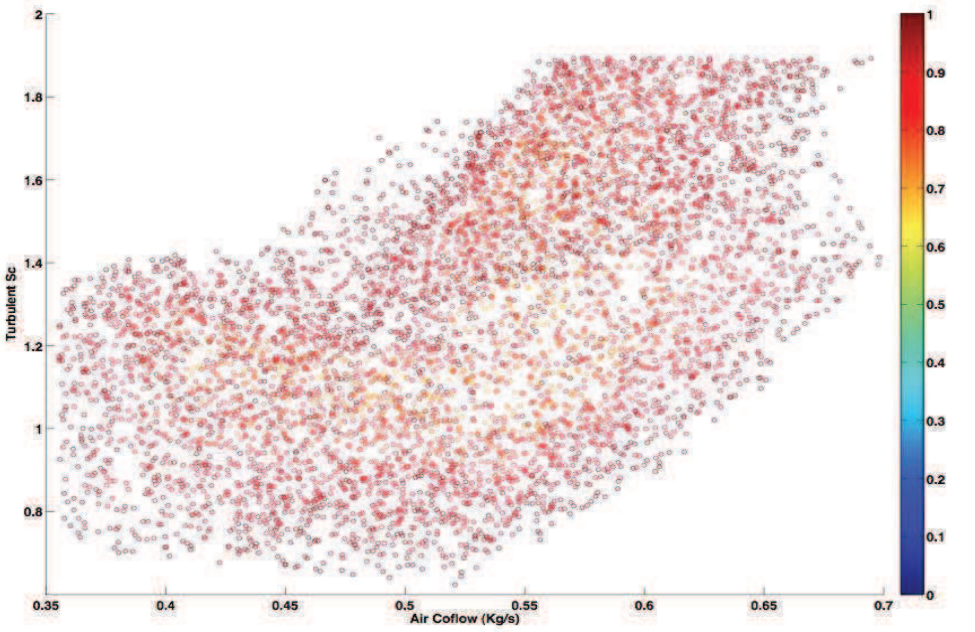

a)

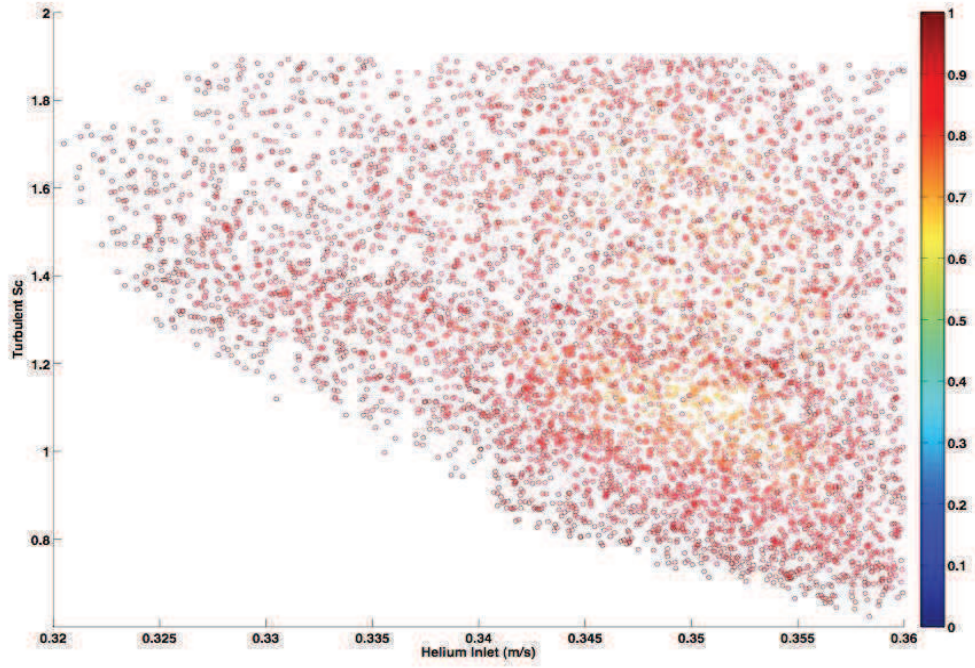

b)

Fig 2.15: Consistent Region for 3-D Helium Case a) Consistent Region in Sc_t & Air Flow Space b) Consistent Region in Sc_t and Helium Inlet Space

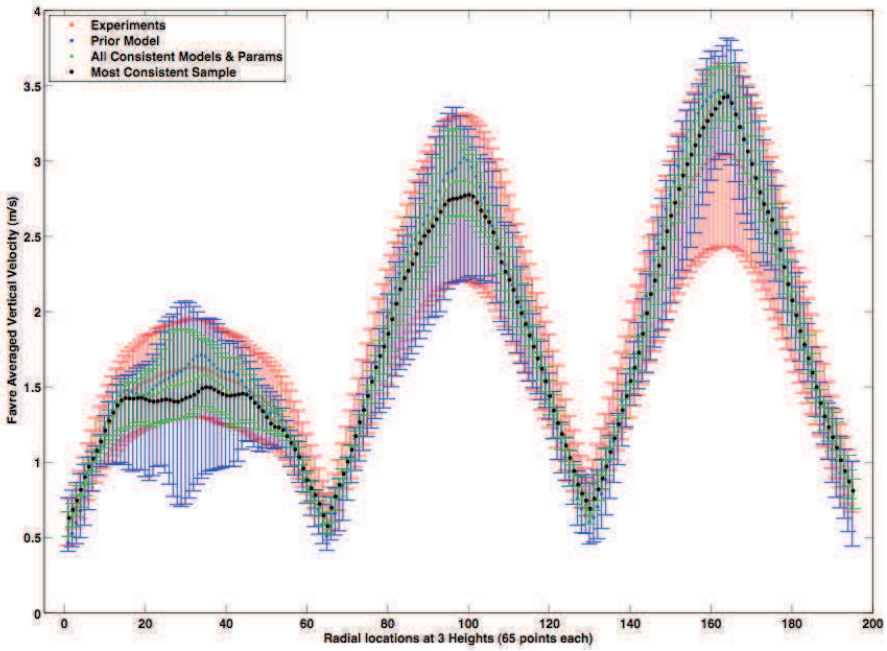

Fig 2.16: Error Bars for 195 Points at 3 Different Heights to Show the Consistent Space for 3-D Case

The application of this framework was completed by feed forwarding the information from the 2-D case results. This helped refine the lower limit of range of helium velocity from 0.264 to 0.29. The reduction in range allowed for better model predictions in the 3-D case. Also, the information gained for other parameters will be used in future validation processes through the hierarchical approach [74]. The effect of dimensionality was also evident from the results. A 2-D case was more consistent with the experimental data as compared to the 3-D case; i.e., CD for the 2-D case was smaller.

2.6. Conclusions

Studies [18] performed earlier have shown that one cannot assume a commercial code, or any code for that matter, to be numerically well-behaved. Although non-monotonic error convergence was observed for the problem of study, the STAR-CCM+ code consistently showed a reduction of error with finer mesh sizes. The results also

provided a good comparison between polyhedral and trimmer mesh, suggesting trimmer mesh might have better conservation properties for LES simulations. An extensive scaling study was also performed as a part of verification activities, to run the simulation in an optimized manner on many CPUs.

The validation and uncertainty framework was successfully applied on a helium-plume experimental dataset. The results not only showed the model to be consistent, but also gave a measure of model consistency. The range for the model parameter Sc_t [0.61 to 1.89] and 2 scenario parameters was obtained for consistent results. Validation results, also answered the question raised by some researchers, regarding the influence of Sc_t on flow characteristics.

CHAPTER 3

MEASUREMENT OF COMBUSTION EFFICIENCY FOR WIND-TUNNEL FLARES WITH UNCERTAINTY QUANTIFICATION

Anchal Jatale, Philip J. Smith, Jeremy N. Thornock, Sean T. Smith, Michal Hradisky
(To Be Submitted)

3.1 Abstract

The objective of this paper is to predict the combustion efficiency of industrial flares by using Large Eddy Simulations (LES). Since the practical utility of the results of a computer simulation is proportional to the degree to which the error and uncertainty in the simulation results have been quantified, the model is validated with experimental data. For this paper, experimental data from the 4-inch flare tests performed at the CANMET wind-tunnel flare facility were used. An approach to validate the model for these experimental data was demonstrated. The implemented approach used prior information about the models or data and the associated likelihood functions to determine informative posterior distribution. The model values were subjected to consistency constraint, which requires that all experiments and simulations be bounded by their individual experimental uncertainty. The final result was a predictive capability for flare combustion efficiency where no/sparse experimental data are available but where the validation process produces error bars for the predicted combustion efficiency.

3.2. Introduction

A flare is an important technology with the primary objective of safely and effectively burning unwanted combustible gases released during various industrial operations. Both government and industry are concerned with the effect of flaring hydrocarbon on air quality, since hydrocarbon gases are much more likely to trap heat in the atmosphere when compared with combustion products such as CO_2 [7]. Thus, research in the field of flare effectiveness has been intensified. The best and most common method used to describe flare effectiveness is combustion efficiency, making it an essential quantity to quantify.

Flaring systems carry numerous problems because of high operating temperatures, varying external winds, lack of suitable sampling locations, etc. It is also difficult to measure combustion efficiency since one must know, simultaneously, both the composition and velocity to obtain a mass flux surrounding the reacting flare. Hence, very limited published research is available on the combustion efficiency of flares in open environment scenarios. Most prominent studies were performed in smaller pilot-scale setups [8-11]. Such studies have shown a wide range of values for the combustion efficiency of flares, ranging from very high values (>98%) to as low as 62% [12-13]. One parameter identified to cause lower combustion efficiencies is the crosswind velocity. Strong crosswinds strip the unreacted fuel from the main flame body and reduce the fuel-oxidizer mixing. Once stripped, this portion of the fuel will have highly incomplete combustion, resulting in an overall reduction in efficiency. Thus, in order to design an effective flare, knowledge of mixing phenomena in a wide variety of conditions is important. However, neither is it feasible to create experiments nor define optimal

operating conditions for the flare in all scenarios. One way to tackle this problem, cost effectively, is to use computational combustion simulations. The simulation also provides a method for mapping out the best operating space as a function of the controlled and uncontrolled variables present in typical flare operations. This paper focuses on one such simulation approach.

The combustion physics of industrial flares is very turbulent and features multiple reactions. The temperature ranges in flares also give rise to radiation heat transfer. Turbulent combustion applications have such complex physics coupled with a wide range of length and timescales. In order to completely resolve these scales for numerical simulations, extremely unrealistic computing powers are required. Thus, a majority of industry uses standard Reynolds Averaged Navier-Stokes (RANS) methods, which are less resource intensive and provide results in less time. The RANS methods, however, are unable to represent any timescale dependency, an important aspect of flare physics. They are also incapable of capturing fuel separation mechanism at high winds or any unsteady information, such as instantaneous mixing and flame shape. Due to these limitations, the Large Eddy Simulation (LES) model was used for performing the flare simulations in the current study. LES takes advantage of the recent increase in computing power and captures a large range of turbulent time and length scales. This, in turn, provides a better measurement of combustion efficiency.

The practical utility of the results of any numerical simulation is proportional to the degree to which error and uncertainty have been quantified. Once they are quantified, tools can be used to predict results accurately for any scenario, even if such predictions are impossible in experiments. This critical question of building confidence in results is

also associated with flare simulations. Currently, most available strategies rely on the notion that simulation data should be in close conjunction with experimental results. One such technique is Verification, Validation and Uncertainty Quantification (V&VUQ). This technique focuses on a combination of 3 processes, which, together, quantifies both numerical and physical accuracy. The third step of the technique is to measure the deviation of the model output from the experiments. This will simultaneously build and quantify the confidence of the results. Figure 1.1 from Chapter 1 describes this approach. The cyclical nature of the process allows for repeated back-and-forth transfer of information, thus improving the model as a whole by reducing the difference between the experimental and simulation results.

Before performing validation and uncertainty quantification, the code was verified in the authors' previous work, by using the Method of Manufactured Solution (MMS) approach [77]. Manufactured solutions allow for arbitrary complexity in the solutions because they have no physical meaning and are created to verify all parts of the equation [3, 60]. This study ensured that code behaved mathematically as intended. The current paper focuses on comparing the simulation data with the experiments by quantifying the difference between them. In this study, the wind-tunnel flares of the CETC (CANMET Energy Technology Centre) flare testing facility in Ottawa, Canada, were simulated using LES. The implemented approach used prior information about the models and data and their associated likelihood functions to determine informative posterior distribution. The numerical simulations were conducted using the commercial code STAR-CCM+ v5.06.010. The VUQ framework estimated the uncertainty in applicable ranges of model parameters as well as scenario parameters.

3.3. Numerical Setup

The LES-based model in STAR-CCM+ solves the flow equations (velocity and pressure) in a segregated pattern. In this model, pressure and velocity are coupled using the Standard Semi-Implicit Method for Pressure Linked (SIMPLE) algorithm [55]. The compressible Navier-Stokes equations are closed using subgrid-scale turbulence models, which employ the Boussinesq hypothesis [56] to provide the relation between turbulent flux and subgrid-scale turbulent viscosity, μ_t. The turbulent viscosity, in turn, is estimated by the WALE (Wall-Adapting Local- Eddy Viscosity) subgrid-scale model [57].

3.3.1. Combustion Model

The simulation solves the total energy equation by using chemical thermal enthalpy as the independent variable. Temperature in the system is calculated by an equation of state. Various definitions of combustion efficiencies are published in the literature [8-13]. In common practice, it is defined as the ratio between the carbon present in unburned flare gases and the carbon in products in the form of CO_2 [8]. This paper uses a progress variable approach to define combustion efficiency [16]. The Progress Variable Model (PVM) is designed to incorporate complex chemical mechanisms with a reduced computational cost. A progress variable transport equation, based on chemical enthalpy, in addition to using transport equations for the mixture fraction and the mixture fraction variance, is used to describe the combustion process for LES. It is a dimensionless parameter that shows the progress of the combustion by tracking chemical enthalpy of the mixture from its initial state to the equilibrium state. It is defined as:

$$C = \frac{h_{298} - h_{298\,|c=0}}{h_{298\,|c=1} - h_{298\,|c=0}} \tag{3.1}$$

where h_{298} is the chemical enthalpy of the mixture at 298 K. When C = 0, the mixture is unburnt, and conversely, at C = 1, the mixture is fully burnt, i.e. it is in an equilibrium state. The mixture chemical enthalpy is transported on the LES mesh based on the following equation:

$$\frac{\partial(\rho h_{298})}{\partial t} + \frac{\partial(\rho u_j h_{298})}{\partial x_j} = \frac{\partial}{\partial x_j}\left(\Gamma_{h_{298}} \frac{\partial h_{298}}{\partial x_j}\right) + \alpha\omega_{h_{298}} \tag{3.2}$$

where source term $\omega_{h_{298}}$ is taken from the precomputed table, alpha (α) is a source-term scaling factor specified by the user, and $\Gamma_{h_{298}}$ is the diffusion constant. The value of α is a free parameter and is used later in the V/UQ study. A PVM look-up table is constructed using the DARS package on the basis of specified information on fuel and oxidizer types, as well as combustion conditions. DARS assumes that each cell is a small, constant pressure batch reactor. For all simulations, a detailed chemical mechanism from Wang et al. [78] was imported into DARS and used to generate the PVM look-up table. DARS data are integrated over a PPDF beta function computed for each of the mixture fraction and mixture fraction variance entries, in order to generate the table with turbulence closure. The density, temperature, and all species concentrations for the mixture during the simulations are determined from the look up table.

3.4. Experimental and Simulation Setup

The experiments used in this study were performed at a flare testing facility at CETC (CANMET Energy Technology Centre) in Ottawa, Canada. This facility uses a high speed fan to produce a range of crosswind speeds in a tunnel. The main chamber is 1.2 m wide and 8.2 m long, with a ceiling height of 1.8 m. The 4″ carbon steel flare pipe is 40″ long [79]. The facility is illustrated schematically in Figure 3.1.

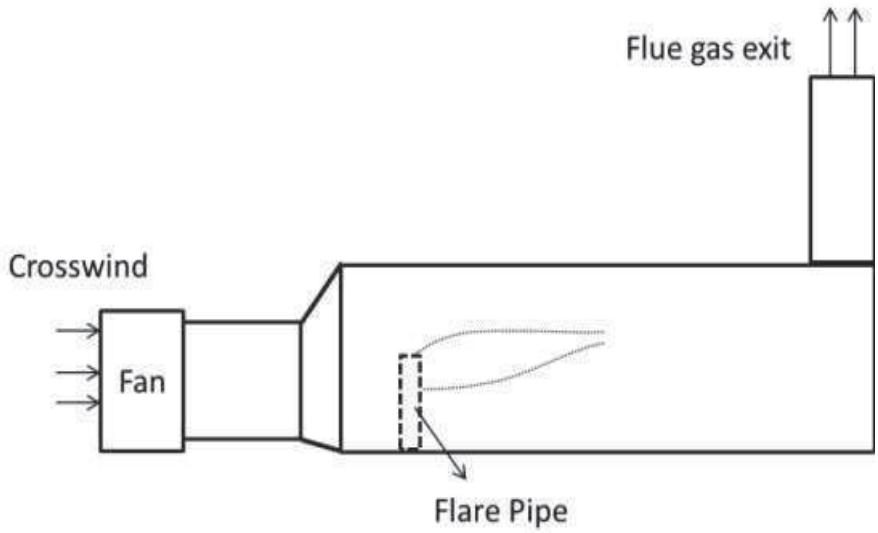

Fig 3.1: Schematic of Flare Testing Facility (Adapted from [79])

The composition of fuel coming in through the flare pipe at 20 Kg/h is (vol %): CH_4-95.33, C_2H_6-2.1, C_3H_8-0.13, C_4H_{10}-0.02, N_2-1.8, CO_2-0.62. These data were measured in the stack, using a 0.46 m sintered metal tube placed at the centerline. Figure 3.2 shows the data collected for this set of experiments with respect to different crosswind velocities. The combustion efficiency was determined by the ratio of carbon as CO_2 in the stack gas (excluding the amount of any CO_2 that came in with the inlet air) to the carbon coming in fuel gases [79]. Figure 3.3 shows the domain and meshing scheme used for the simulations. Fuel comes out of the pipe at 300K. The left boundary is the cross-flow inlet. Here, the air comes in at 287 K and contains 350-400 PPM of CO_2, similar to the current concentration in the atmosphere. This CO_2 was taken into consideration while computing the combustion efficiency. The domain was meshed using a trimmer meshing scheme with approximately 10.5 million cells (Figure 3.3). In order to keep the computational cost less for this large domain, regions with mostly steady flow received coarser mesh.

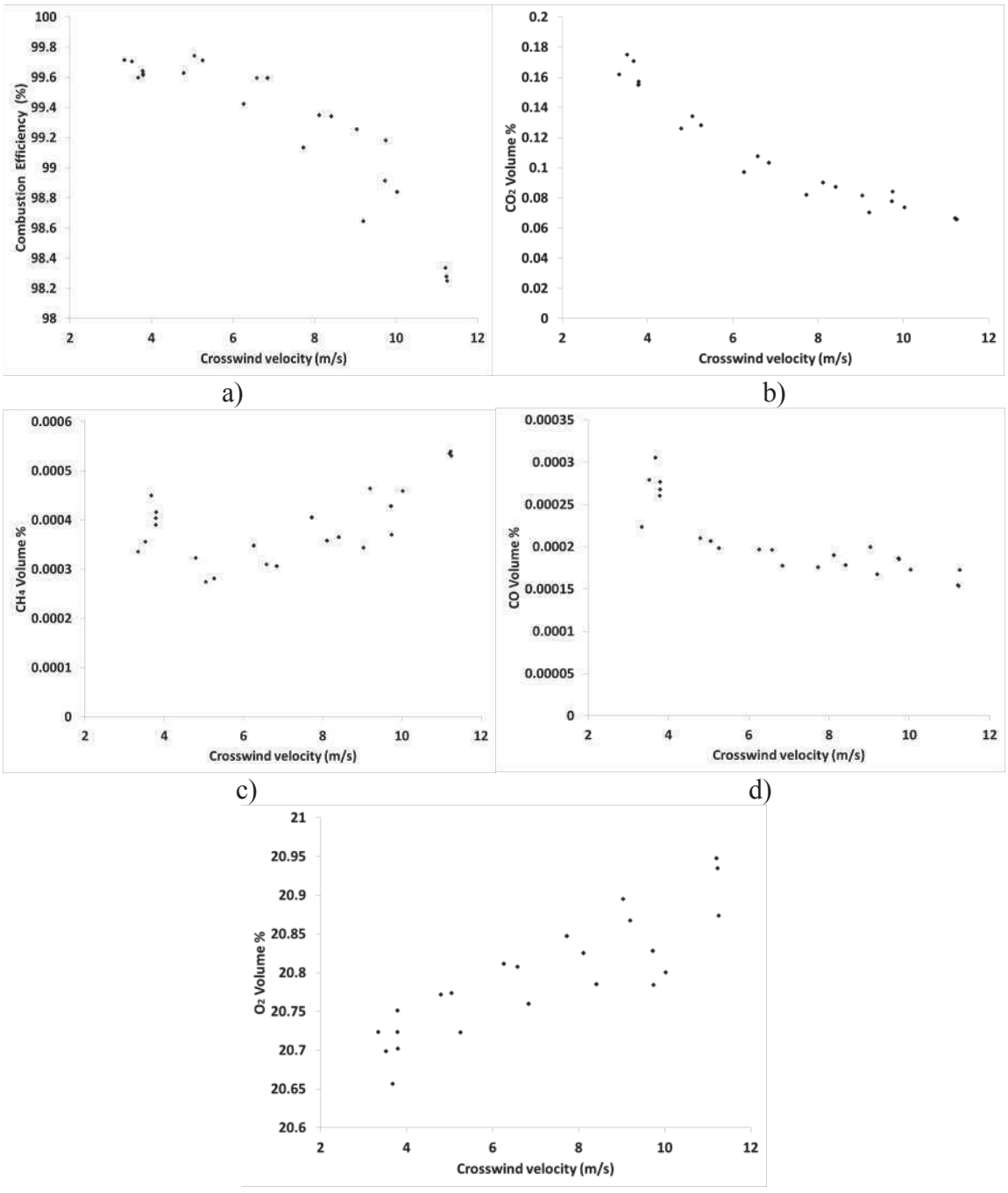

Fig 3.2: Experimental Data w.r.t. the Crosswind: a) Efficiency b) CO_2 Concentration c) CH_4 Concentration d) CO Concentration e) O_2 Concentration

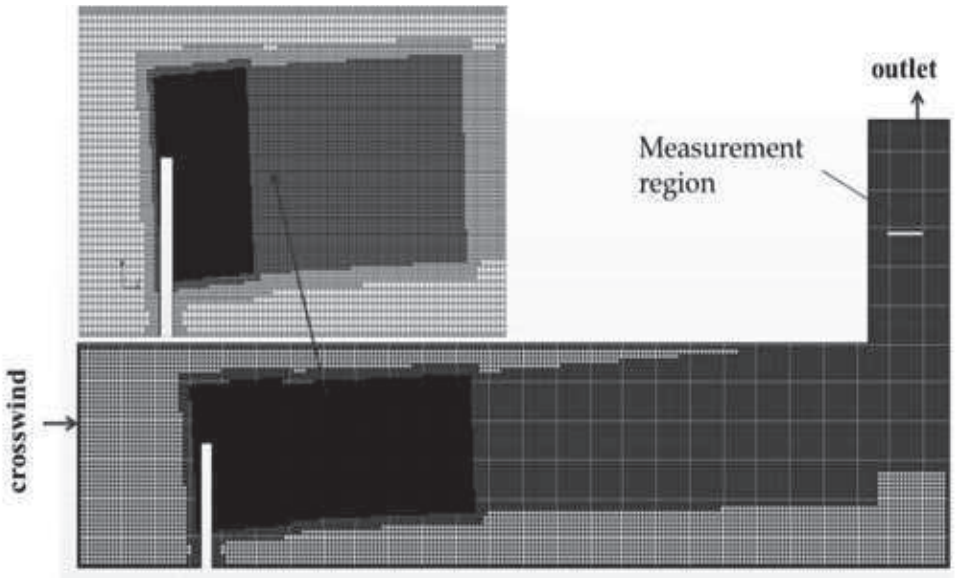

Fig 3.3: Meshing Scheme Used (10.5 Million Cells)

3.5. Results

The simulations for the wind-tunnel flare system were performed using various crosswinds conditions. These simulations used 480-600 processors. For the initial 3 seconds, a time step of 0.05 seconds was used to set up a flow filed in the domain. Then the time step size was reduced to 0.0005 seconds. The next 3 seconds allowed for computational flow transitions to reach quasi-steady flow conditions. After the establishment of a developed flow, the mass flow average values of the desired quantities were collected at the measurement location (Figure 3.3) for 4 seconds. Typically, the computational time varied between 190 hours and 240 hours. The combustion efficiency computed from the model is given by progress variable C.

Figure 3.4 show that an increase in crosswind velocity reduces the combustion efficiency. This can be attributed to decreased air/fuel mixing time which results in high unburnt fuel. The trend of combustion efficiency observed here was also reported in previously published works [8-10].

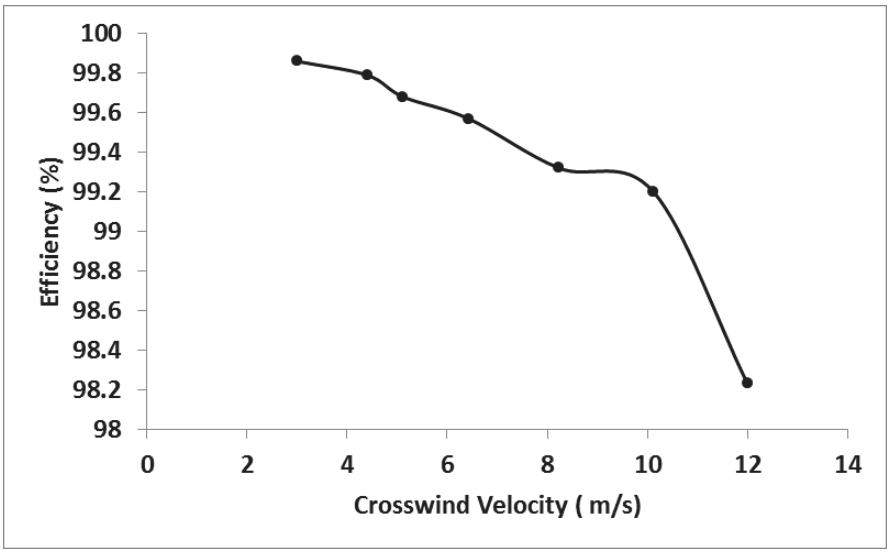

Fig 3.4: Efficiency w. r. t. the Crosswind Velocity.

Figure 3.5 shows the flame structures, efficiencies, and temperature distribution of flare at crosswind velocity of 6 m/s. The color bar was modified to show C from 0.99 to 1 for better differentiation. All the areas with efficiency values less than 0.99 are in grey. Also, pure air was assigned an efficiency of 1. It can be seen that the effect of crosswind is limited to the near tip region of the flame. Beyond that, buoyancy effects are prominent because of the low-density properties of the combustible gases. Also, the phenomenon of fuel strip can be observed at the stack side of the flare. Fuel strip refers to the breaking of fuel from the main flame structure, resulting in its transport as a separate fuel pocket.

3.6. Validation Framework

Validation is important in providing quantitative and reliable uncertainty bounds on predictions from the simulations. The 6-step framework [31] is combined with a Monte-Carlo sampling approach that provides upper and lower bounds of the prediction.

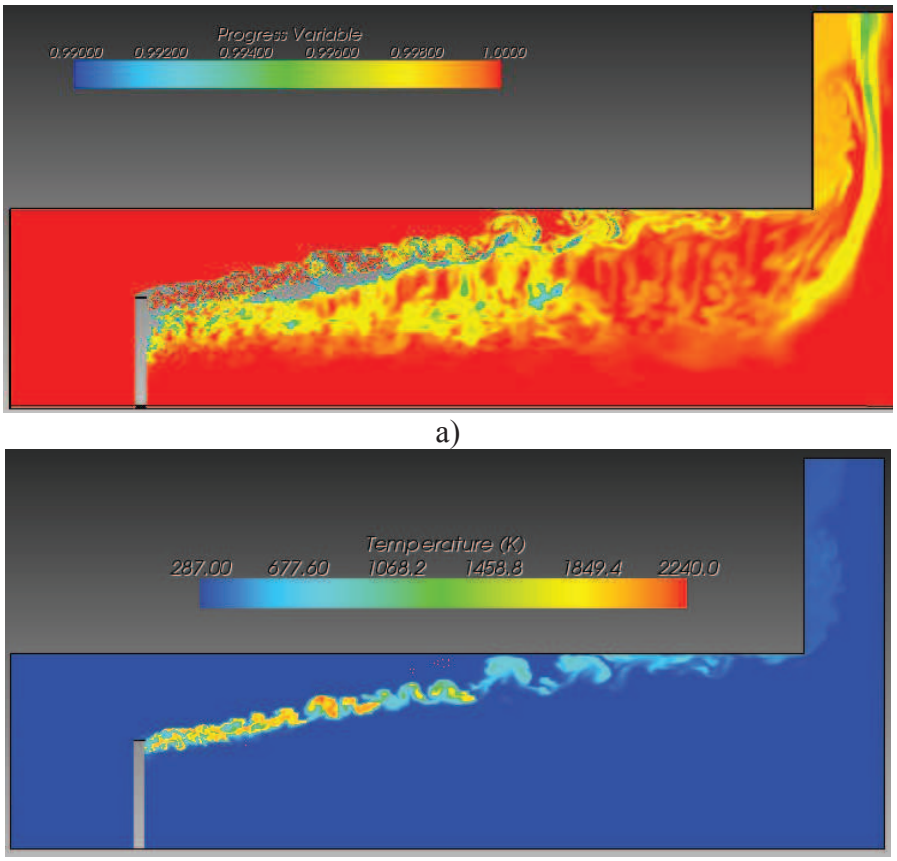

Fig 3.5: Variables at a Plane in the Domain for a Crosswind Velocity of 6 m/s
a) Progress Variable C (Efficiency) b) Temperature Profile,

This section will define the steps of the framework, along with its application on flare simulations. For the purpose of VUQ study in this paper, all the variable types and parameters present in a known system were classified into four major categories. 2 of the 4 categories were defined here. Details of this categorization can be found in the authors' previous work [90].

- *Active variables*: These subsets of parameters have a measurable influence on the property of interest. They consist of both model parameters and scenario parameters.

- *Design/Manipulated variables*: These are sets of variables that are changed by the experimentalists to create various scenarios for experiments—for example, locations of data collections in a system. In the terms of validation studies, these are the variables that distinguish between dataset units.

The applied framework is as follows:

Step 1: A list of model inputs and parameters with uncertainties or ranges (Input/Uncertainty (I/U) map) [64] was created.

In this step, model inputs and parameters were ranked according to their impact on the prediction error. The list also includes the uncertainties for each input with their current treatment status in the model. This dynamic I/U map can be revisited and updated after running other steps. Table 3.1 shows the I/U map for the wind-tunnel flare. The impact factors were estimated based on prior experience and through sensitivity analyses and tuning. As seen in the I/U map, 2 parameters were given impact factor 5; thus, an analysis was first performed with those parameters, keeping the rest fixed. An optimum mesh size was finalized before running the cases.

The experimental data not only show the variation with changing crosswind velocity, but the measurements at multiple crosswind velocities. Thus, the choice of crosswind velocity as an active variable is interesting, as it is also a design variable. As such, it provides a very good opportunity for testing the framework for the analysis of uncertainties in multiple directions. In other words, the processing of experimental uncertainty includes both the measured values as well as crosswind velocity, giving an uncertainty region. This will be highlighted in detail in the results section.

Table 3.1: I/U Map for Wind-Tunnel Flares

INPUT		IMPACT	UNCERTANITY	CURRENT STATUS
Geometry	Pipe diameter	1	Unspecified	Fixed(4 inch)
	Pipe height	1	Unspecified	fixed
Input	Fuel velocity	1	Unspecified	fixed
	Crosswind Velocity	5	[3.34-11.26] m/s	controllable
Model Parameters	Turbulence Sc number	4	Unspecified	Set by modeler
	Turbulence Pr number	4	Unspecified	Set by modeler
	Source term scaling factor (α)	5	[1-12.071]	Set by modeler
Numerical Parameters	Mesh	2	Unspecified	Convergence/speed compromise
	Boundary conditions	1	Unspecified	Fixed
	Initial conditions	1	Unspecified	Fixed

In addition, various researchers [8-13, 80] have identified crosswind as an important factor for variable combustion efficiencies of flares. The second active variable chosen is a model parameter, which scales the reaction-rate source term in the combustion model.

This term controls the extent of combustion for a given condition, which, in turn, affects the efficiency. Thus, determining the correct value of a source term is important. Turbulent Schmidt number and Prandtl number are 2 other variables with high ranking. They were considered as active variables in the authors' other validation work [74]. This article focuses on finding a consistent range for only 2 variables.

Step 2: Evaluation criteria were defined.

In this step, evaluation criteria were specified for model output. Based on the experimental data, the mass averaged values of stack gas species were selected as evaluation criteria. The data were averaged over 2 perpendicular 0.46m long lines of cells at the centerline of the stack (Figure 3.3). This experimental procedure and data collection also helped to decide the range of chosen active variables.

Step 3: Using the collected data, a Design of Experiments (DOE) was created.

This paper did not use any standard method to create DOE. The variable space was strategically filled on the go to capture detailed information in the most impactful regions and create an optimum-sized DOE. A DOE was prepared for 2 active variables (Table 3.2). Values for other model parameters, Sc_t and $Pr_{t,}$ were fixed at 0.9 for the complete set of experiments.

Step 4: The computer model output was approximated.

The validation process requires multiple code evaluations. The high cost of each LES simulation combined with the Monte-Carlo sampling procedure for the consistency

Table 3.2: Design of Experiment for Wind-Tunnel Flare System

Sim#	**Crosswind velocity (m/s)**	**Model parameter alpha (α)**	**Sim#**	**Crosswind velocity (m/s)**	**Model parameter alpha (α)**
1	3	1	11	12	6
2	4.4	1	12	6.9563	10
3	6.9563	1	13	9.5144	10
4	9.5144	1	14	3	12.071
5	12	1	15	4.4	12.071
6	6.4265	5	16	5.12	12.071
7	8.2353	5	17	6.4265	12.071
8	10.12	5	18	8.2353	12.071
9	3	6	19	10.12	12.071
10	4.4	6	20	12	12.071

test necessitated the use of an LES surrogate. Creating a good surrogate model is an important step in validation, since a bad surrogate model can insert additional errors and create relationships between variables which are not present in reality. These models must not only be a good mathematical fit but also follow the real physics accurately. The pioneers of surrogate models were Box and Wilson [70], who developed an approach known as Response Surface Methodology (RSM), in which polynomial surfaces are used to represent output. While polynomials are generally reliable and thus widely used, in the case of sparse data, a polynomial can insert additional information in terms of trends and

physics between 2 points. This drawback was overcome in the current paper by the use of a flexible interpolation method, Delaunay Triangulation. In addition to being computationally less expensive, Delaunay Triangulation ensures boundedness, without being affected by the sampling order [71, 72]. This method is also superior in feature capturing, since all original data points are located on the surrogate surface only.

Step 5: The consistency was measured.

This step required a consistency test. It drew on prior information and exploited a consistency requirement among the available experimental datasets and the simulations of these sets to quantify the uncertainty in model parameters, boundary conditions, and experimental error and simulation outputs to produce predictivity [73]. Using this approach, the uncertainty interval for the data was obtained, which, in turn, was used as the likelihood in the consistency analysis. The most sensitive parameters were then identified and used in the subsequent quantification of predictivity. The consistency constraint used to measure and produce a posterior uncertainty consistent with all experimental and simulation data was defined as [52-54]:

$$\begin{cases} C_{\aleph} = \min \gamma \; subject\ to\ constraints: \\ \beta_i \geq x_i \geq \alpha_i \,, for\ i = 1, \ldots\ldots, n \\ (1-\gamma)u_e \geq |y_m(x) - y_e| \geq l_e(1-\gamma), for\ each\ e \in \aleph \end{cases} \tag{3.3}$$

where α_i , β_i are upper and lower uncertainty bounds of input parameter x_i , y_m is the model value, and y_e is the experimental value. u_e and l_e are the upper and lower bounds of experimental uncertainty or deviations. Equation 3.3 makes sure that all simulations are bounded by their individual experimental uncertainty. The term (1- γ) is added to the equation to make sure that we can quantify the consistency of the model. Each dataset point is checked through the constraint and value for (1- γ) is stored. C_D denotes the

largest value of (1- γ). It gives a measure of an overall consistency of the dataset. The smaller value of C_D corresponds to better consistency.

The major difference between Data Collaboration (DC) and the consistency test used here was that it uses a pseudo-random selection of points (the Monte-Carlo method) to solve a similar set of equations, rather than the domain decomposition iterations of DC. The consistency test employs the following steps:

1) The range of active variables was specified.
2) Experimental data were sampled in order to find any uncertainties present. This was computed through mean and standard deviation with a user-specified confidence range.
3) Using Monte-Carlo sampling, a feasible region for active variables was obtained between the provided ranges.
4) The model was then evaluated at each of the sample points and for each of the experiments or scenarios.
5) A consistency analysis was performed by subjecting the results to the constraints (Equation 3.3). This step revealed how well the evaluated values matched the experimental values. For a point to be called consistent, it needed to satisfy the inequalities for each of the experiments.

Step 6: Information was fed back into the current validation exercise and fed-forward into future validation activities

This step used the results from Step 5 to improve the model, as well as to refine the aspects of the validation process. The results were analyzed to highlight the impact region in variable space, thus helped in populating the DOE points. The UQ results for

the current model could also be used to predict the validity of future models, for which very sparse or no experimental data are present [74].

3.6.1. Validation and Uncertainty Quantification

After converting simulation results into the experimental data format, consistency analysis was performed using the consistency test. This was done by varying both the active variables (crosswind velocity and source term scaling factor alpha) together. 50,000 pseudo-random points were selected from a uniform distribution of active variables, and the result for each point was tested against the consistency constraint. Before performing consistency analysis, the experimental data were analyzed and crosswind velocities were divided to create 6 dataset units. The members of each group were meant to be replicates. This approach helped compute the uncertainty in the values of measured variables (efficiency, CO_2, O_2, CO etc.), as well as the crosswind velocities. Since data are very sparse, a confidence interval of 1.5 was used for experimental uncertainties. The analysis was completed for CO_2, O_2, and CH_4 concentrations only. Since the combustion efficiencies were calculated based on other measurements in the experiment, they were not tested against the consistency constraints, and were therefore computed for the consistent data points using the PVM model. CO was also excluded, since the applied combustion model did not account for quenching, which is a major source of CO generation.

Figures 3.6-3.9 show the prior and posterior consistent regions for measured variables. In these plots, red denotes the experimental data, and the box signifies the uncertainty region. Simulation results and their uncertainties are shown in green. This analysis has 6 different crosswind groups for 3 different desired variables (Concentration

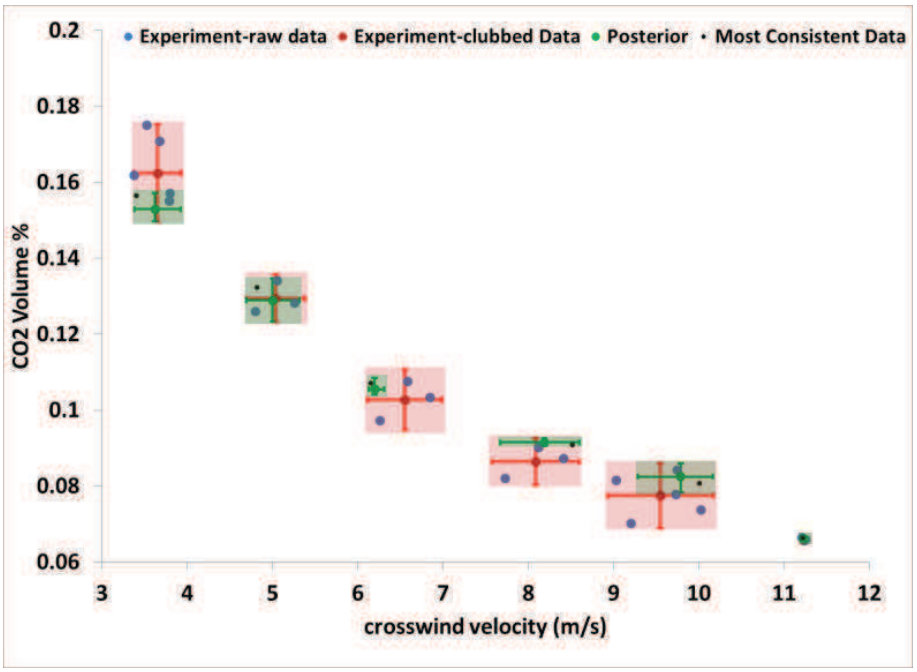

Fig 3.6: Prior and Posterior Consistent Regions for CO_2 Concentration in All 6 Groups

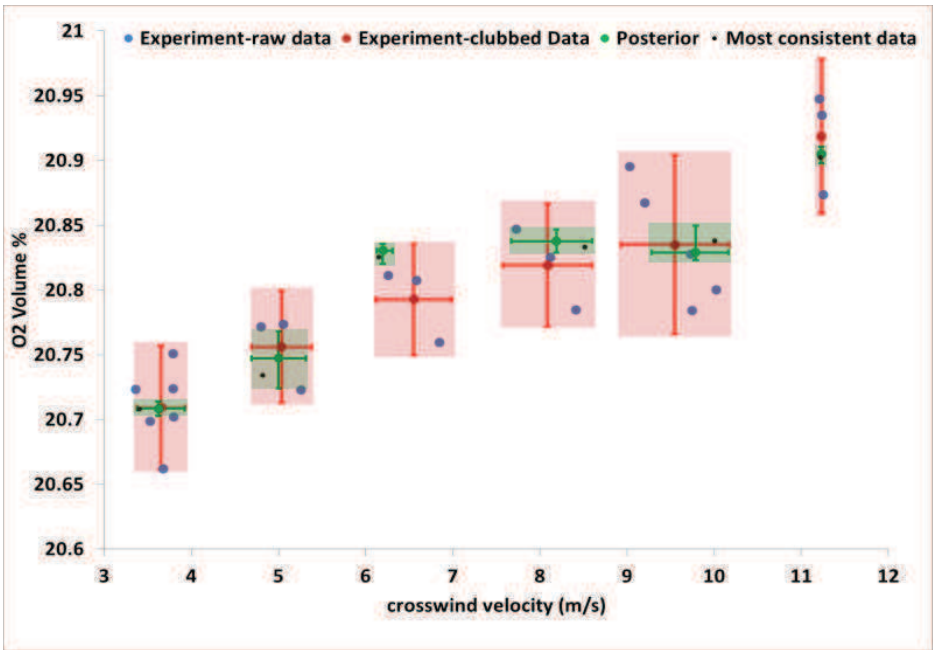

Figure 3.7: Prior and Posterior Consistent Regions for O_2 Concentration in All 6 Groups

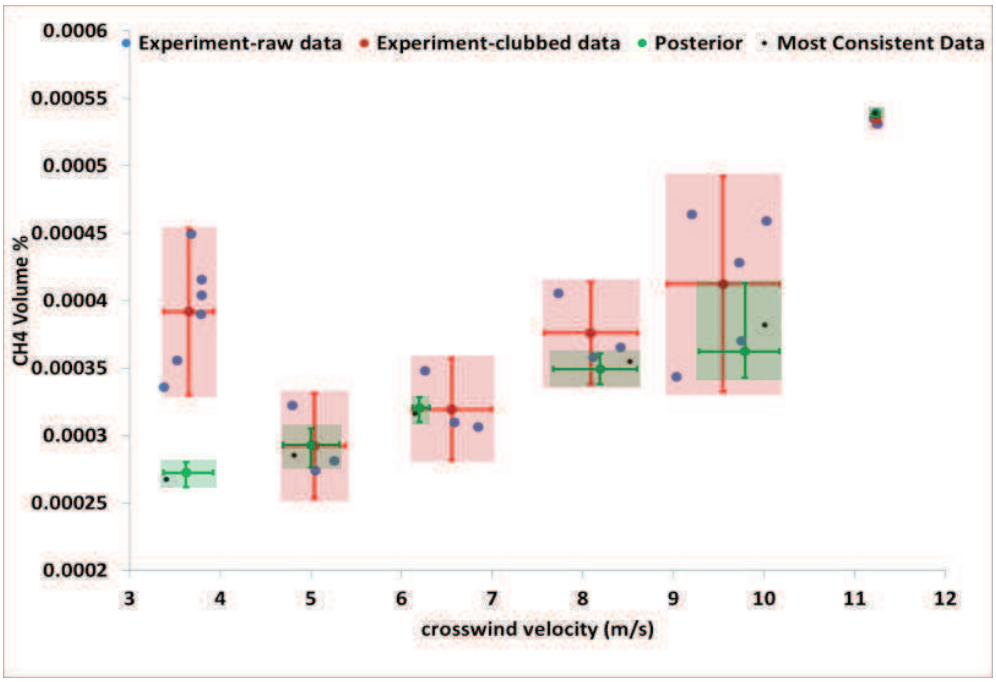

Fig 3.8: Prior and Posterior Consistent Regions for CH_4 Concentration in All 6 Groups

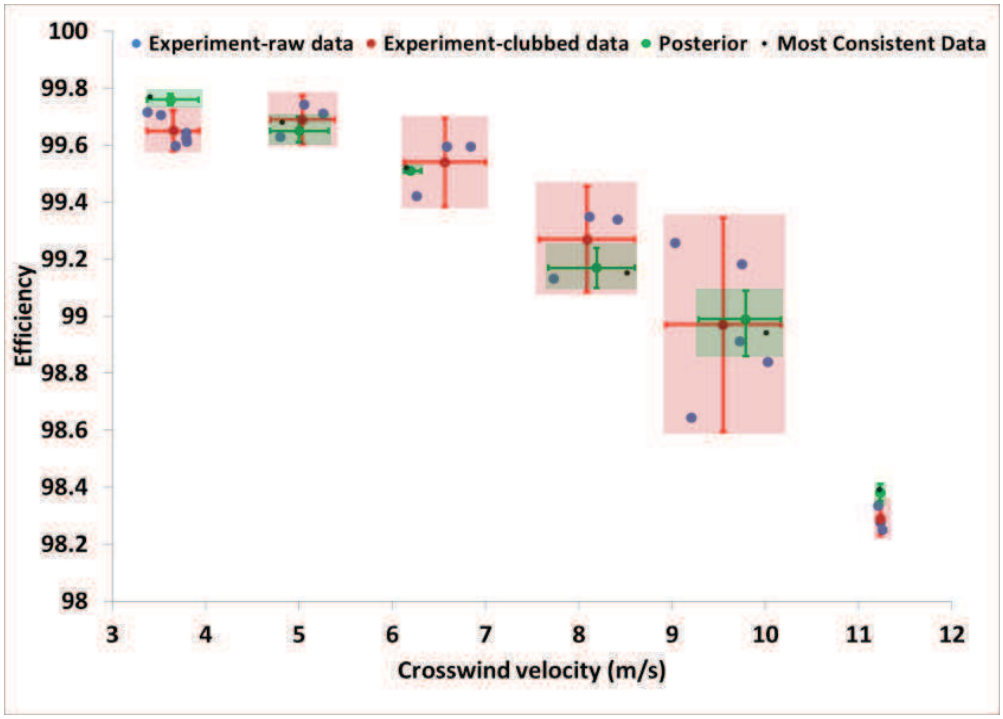

Fig 3.9: Prior and Posterior Consistent Regions for Combustion Efficiency in All 6 Groups

of CO_2, CH_4, and O_2), making a total of 18 dataset points. Each of the 50,000 points was checked for consistency in all 18 dataset units. Simulation results were consistent in all 6 groups for CO_2 and O_2 concentration.

This is shown by the overlapping of prior and posterior regions in Figures 3.7-3.8. For the CH_4 concentration, simulation results were consistent for only 5 of 6 groups. Crosswind group 1, from 3.373 m/s to 3.932 m/s, shows a lower CH_4 concentration for the model (Figure 3.8). Hence, the combustion efficiencies matched the experimental data well, except in the low crosswind group (Figure 3.9). In all, consistency over 17 dataset units was achieved. The discrepancy of CH_4 concentration for the low crosswind group may be either a model issue or a data collection issue. Since the model was able to generate results consistent with experimental data for CO_2 and O_2 concentration in this low crosswind case, we consider that maybe few of the experiments in the CH_4 dataset unit had errors in reporting. Experimental data suggest that as crosswind velocity decreases, efficiencies increase. Theoretically, increase in efficiency signifies more burned fuel and a higher conversion to CO_2. Though the data presented show an increase in CO_2 concentration, they do not show the decrease in CH_4. Another reason for this difference may be the measurement technique used in the simulations. As mentioned earlier, the values were averaged for couple of 0.46 m perpendicular rows of single cells at the stack centerline which may not be capturing the complete picture here. This discrepancy requires both the experimentalist and the modeler to work together to identify and analyze the issue which caused the error.

Table 3.3 shows the range of alpha for consistent data and overall consistency measurement of this dataset.

Table 3.3: Results for Consistency Analysis

Range of alpha for consistent data	6.85 to 8.5
Overall consistency measure, C_D	0.57

This range of model parameter can be used as prior information for future validation studies [74]. Figure 3.10 shows the consistency space for each of the 6 crosswind groups. It also gives the range of alpha for which results are consistent.

3.7. Conclusions

The combustion efficiency for a wind-tunnel flare system was successfully measured by using the progress variable approach. This approach, in conjunction with LES, eliminates various problems of measurement, including a large range of scales and dilution of the species. The effect of crosswind on the flame structure and combustion efficiency was also studied. The flares seemed to be less efficient at higher crosswind velocities. The results were also successfully validated using a framework, and they were consistent with the experimental data (with the exception of CH4 concentration in the lowest crosswind group). This exception, however, illuminates an advantage of performing VUQ. The analysis requires the modeler to collaborate with the experimentalist in order to determine if the discrepancy is an error in experiments or the result of missing information from the model or with the measuring technique. VUQ analysis also handles the uncertainties of multidirections efficiently. A range for the model parameter alpha [6.85-8.5] was obtained as an output, which gave consistent results. The validation approach and the results obtained suggest that this model is a positive step in predicting efficiencies for actual industrial flares with desired accuracy.

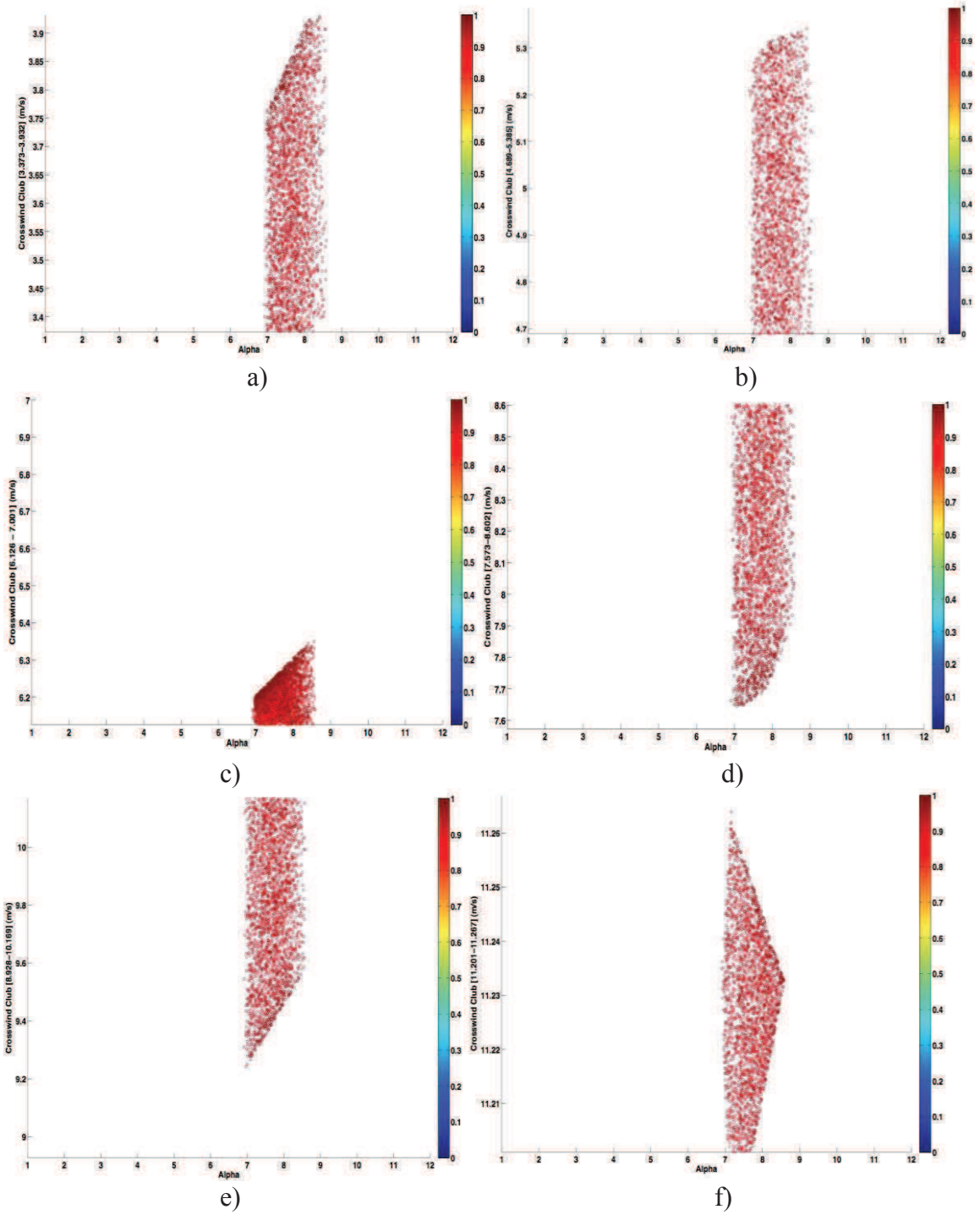

Fig 3.10: Consistency Regions for All 6 Crosswind Groups: a)[3.373-3.932] b)[4.689-5.385] c)[6.126-7.001] d)[7.573-8.602] e)[8.928-10.169] f)[11.201-11.267] m/s

CHAPTER 4

VALIDATION AND UNCERTAINTY QUANTIFICATION: PREDICTION FOR PROBLEM WITH NO EXPERIMENTAL DATA

Anchal Jatale, Philip J. Smith, Sean T. Smith, Jeremy N. Thornock, Michal Hradisky
(To Be Submitted)

4.1. Abstract

The practical utility of the results of a numerical simulation is proportional to the degree to which the error and uncertainty in the simulation results have been quantified. Such quantification becomes difficult for complex systems with little or no experimental data. This paper describes an approach which integrates computational and experimental data through a range of experimental scales and an hierarchy of complexity levels. In this hierarchy, data and models from simpler common physics systems featured at lower levels. The uncertainty information was transferred from one level of hierarchy to another. This implemented approach draws on prior information and exploits a consistency requirement among the available experimental datasets and simulations of these sets, in order to quantify the uncertainty in model parameters, boundary conditions, and experimental error and simulation outputs necessary to produce predictivity. The application chosen for this purpose is a measurement of combustion efficiency for industrial flares using LES. Experimental data for this application were acquired from expensive wind-tunnel measurements. The most sensitive parameters were identified and

used in the subsequent quantification of predictivity. The use of quantitative validation methodology to improve the models and parameters among the multiphysics components was also demonstrated.

4.2. Introduction

Computer simulations are very important in engineering and design. Be it the aerospace, chemical, construction, or mechanical industry, all use simulation extensively to improve their productivity. Even government agencies use simulations to effectively develop public policies and prepare safety procedures. This growing dependency on computer simulations makes it essential to have confidence in the results [1]. The practical utility of the results of a numerical simulation is proportional to the degree to which the error and uncertainty in the simulation results have been quantified. Once this is done, a tool can be used to predict results accurately for any scenario, even if such measurement is not possible in experiments. Computational Fluid Dynamics (CFD) code also needs to be validated before its use. Most of the available strategies to validate a code are based on the logic that simulation data should be in close conjunction with experimental results. One such technique is Verification Validation and Uncertainty Quantification (V&VUQ). This technique focuses on a combination of 3 processes, which, together, determines both numerical and physical accuracy. This technique also measures the deviation of the model output from the experiments. Figure 1.1 from Chapter 1 describes this approach schematically. The cyclical nature of the process allows the transfer of information back and forth many times, thus improving the model as a whole by reducing the errors. The scope and complexity of many real-world problems result in very sparse and expensive ‘a priori’ experimental data. Such a lack of

data does not allow validation of the model. Yet this issue may be tackled by building a hierarchical validation framework. In this framework, the computational and experimental data are integrated through a range of experimental scales and a hierarchy of complexity levels, ultimately creating the prediction of the complex application with data and models from simpler systems lower in the tree.

The V&VQ analysis is undertaken by organizing data around a central overarching problem, with a goal of producing quantified error bounds for the important metrics of the central problem. The lower bricks of the hierarchy include smaller-scale problems. The selection of the smaller-scale problems is based on some similarity with the overarching problem's physics and the presence of experimental data [5]. The hierarchy provides a concept for isolating the physics that contribute to the intended use of the model and quantifying errors at each of the different levels. It also provides insight into error propagation from the various isolated submodels.

The intended use of the validation/uncertainty quantification (V/UQ) hierarchy in this paper is to deliver a computational LES tool for the measurement of combustion efficiency for an industrial flare with predictive error bounds. The primary objective of flares is to burn unwanted combustible gases released during industrial operations in an effective and safe manner [6]. Since hydrocarbon gases like methane are twenty times more effective at trapping heat in the atmosphere when compared with combustion products such as CO_2, the effect of flaring hydrocarbon on air quality is of major concern to both government and industry [7]. Thus, an understanding of flare effectiveness is very important. At this point, combustion efficiency is the most commonly used quantity to

describe the effectiveness of such systems. Yet the lack of experimental data for combustion efficiency is a main worry in the flare community.

Flaring systems carry numerous problems, such as the effect of high temperatures and radiant heat on equipment, the effect of external winds and intrinsic turbulence on the nature of flare flames, the unclear dilution of flare emission plume with ambient air, the lack of suitable sampling locations, etc. It is also difficult to measure combustion efficiency, since one must know simultaneously both the composition and velocity to obtain a mass flux surrounding the reacting flare. Hence, very limited published research on the combustion efficiency of flares in open environment is available. Most of the prominent studies were performed in smaller pilot-scale setups [8-11]. Researchers have shown that the combustion efficiency of flares can be very high (>98%) for a wide range of flow rates and flare gas compositions [12]. However, studies also found that some flares had efficiencies as low as 62% [13]. In order to design a highly efficient flare system, knowledge of the unsteady mixing phenomena is important. That being said, the wide variety of fuel composition, fuel velocities, ambient wind conditions, and the size of the flare equipment make these experimental studies unreasonable.

One way to tackle this problem cost-effectively is by using computational combustion simulations. Still, the process of validating a model to predict desired quantities with certain confidence is hampered by the lack of experimental data. This paper proposes a hierarchical method in order to validate a model and make it useful for prediction of an overarching problem, like measurement of combustion efficiencies from industrial flare systems, where experimental data are not readily available. The 2 validation studies performed individually by the author for cases with a priori

experimental data and relevant physics were represented as lower level bricks in the hierarchy: A nonreacting buoyant helium-plume [77], and the wind-tunnel flare experiments [17]. V&VUQ studies on these cases were performed separately in the author's previous work. Here a validation study was performed by taking these 2 different sets of experimental data into consideration together. Numerical simulations were conducted using the commercial code STAR-CCM+ v5.06.010. The VUQ framework provides the uncertainty, in applicable ranges, of model parameters and scenario parameters. LES was used as the turbulence model for the simulations.

4.3. V&VUQ Frameworks

The modeling and simulation community is actively working to create a complete and detailed framework for performing V&VUQ. References [20–30] highlight various lines of thinking and progress in this area. All the methods used for VUQ can be placed in 2 major categories: Predictive and Physical [31]. The predictive approach believes that accurate comparison between predictions and field data is the primary indicator of model evaluation. On the other hand, the physical approach focuses on the accuracy of individual elements of the model itself. The framework used in this paper most closely resembles the predictive approach. It draws on prior information and exploits a consistency requirement among the available experimental datasets and simulations of these sets, thereby quantifying the uncertainty in model parameters, boundary conditions, experimental error, and simulation outputs to produce predictivity.

All of the V&VUQ frameworks discuss uncertainties in the predicted results. These uncertainties are commonly classified according to their core: Aleatoric or Epistemic [33-37]. Another way to categorize uncertainties is based on their source [38],

such as parameter uncertainty, model inadequacy, algorithmic uncertainty, experimental uncertainty, interpolation uncertainty, etc.

Oberkampf et al. developed a comprehensive framework for model validation and verification [22]. This proposed framework coincides with predictive uncertainty and is known as Probability Bounds Analysis (PBA) [39-41]. Within the PBA framework, all uncertainties are classified according to their mathematical structure before estimating the numerical uncertainty. Methods such as Richardson Extrapolation [4], Discretization Error Transport Equations [42, 43], and Residual/Recovery methods in finite elements [44-45] may be used. Because the estimated values are not completely accurate within this method, upper and lower bounds must be applied. The total uncertainty in the framework is a combination of numerical error, error in input parameters, and model form uncertainties. The input uncertainties are circulated through the model using Monte-Carlo sampling methods. The model uncertainty is quantitatively estimated at the scenarios where experimental data are available [39, 46-47], then extrapolated to the other points of interest.

Another widely-recognized framework is provided by the American Society of Mechanical Engineers (ASME) [24]. In contrast to the PBA framework, experimental uncertainties in the ASME framework are processed in the same way as uncertainties in the simulation results. The uncertainty in each error source is estimated as the standard deviation of all possible errors. Thus, a range for modeling errors is found. The main objective of this methodology is to calculate validation uncertainty, which is defined as:

$$U_{val} = \sqrt[2]{U_{num}^2 + U_{input}^2 + U_D^2} \tag{4.1}$$

where U_{num} is the numerical uncertainty calculated using code and solution verification techniques similar to the first framework; U_{input} is the uncertainty in the input parameters of the model, measured by the Sensitivity Coefficient method or Monte-Carlo sampling methods; and U_{exp} is the uncertainty in the experimental results, determined using well-accepted techniques [24].

Recently, V. Romero [20] proposed a new validation approach known as Real Space validation. This approach works backwards from an end objective to estimate the accuracy of predictions. It adopts and refines some elements from the literature, while also constructing other elements. There are still more frameworks available in the literature, most of which are based on Continuous Monte-Carlo [49] and Polynomial Chaos [50, 51].

The validation framework used in this paper is inspired by Bayarri et al. [9] and Frenklach et al. [52-54]. The Bayarri et al. framework is based on the Bayesian approach. The purpose of this framework is to produce tolerance bounds for model validity, using Bayesian and likelihood techniques. It provides a quantitative understanding of the model validation. The accuracy of the model is estimated by comparison with field data. This methodology was combined with the Data Collaboration (DC) approach proposed by Frenklach et al. [52]. The main goal of DC is to provide quantitative and reliable uncertainty bounds on predictions from simulations [52-54].

4.4. Overarching Problem

As stated previously, the main objective of this paper is to validate a code for predictive use of the overarching problem with no experimental data by using available, lower-scale experimental datasets. This was accomplished by constructing a bridge

between the experimental data and simulation results in the form of a VUQ analysis. This bridge uses prior information about the models and data, as well as the associated likelihood functions, to get informative posterior distribution. This approach sheds light on the transfer of information and uncertainties from one brick to another. The application highlighted here is the measurement of combustion efficiency for an industrial flare system. 2 smaller-scale problems with common physics are included in the hierarchy. These cases have sufficient experimental data to perform the analysis. Figure 4.1 shows the structure of the hierarchy for the chosen overarching problem. Because of the expensive computational nature of LES simulations, buoyant-flow experiments play an important role in validating a model used for predictions of systems with high complexity, like combustion. Though they sound simple, buoyancy-driven flows provide their own challenges in the form of an inverse energy cascade. Gravitational forces acting on the fluids give rise to density stratifications, which, in turn, produce Rayleigh-Taylor instabilities [14, 15].

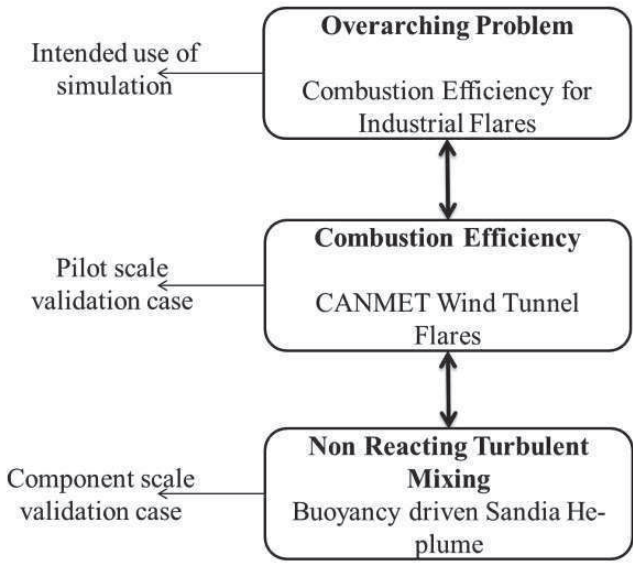

Fig 4.1: Hierarchy for Overarching Problem: Combustion Efficiency for Industrial Flares

A 1 m nonreacting helium-plume flow makes a good case for studying generation of turbulence due to buoyancy without the complexities of combustion and radiation that would take place in a fire; hence, it was chosen as the component-scale brick of the hierarchy. The pilot-scale brick was made up of wind-tunnel flare experiments. This experiment reports combustion efficiency data, which is a quantity of interest for the overarching problem. Various definitions of combustion efficiencies are present in the literature [8-13]. Commonly, it is defined as the ratio of carbon present in unburned flare gases to carbon in products in the form of CO_2 [8].

The Progress Variable Model (PVM) is designed to incorporate complex chemical mechanisms with a reduced computational cost. A progress variable, based on chemical enthalpy, in addition to using a mixture fraction and mixture fraction variance, was used to describe the combustion process for LES [17].

One of the key aspects of VUQ is the transfer of uncertainties and information from one tier of the system to another. In this paper, the framework was first applied on the component-scale tier, and the relevant information discovered was then used for validation of the pilot-scale case. For this step, only some information was used from the output of the first case. This information helped reduce the uncertainty in priors for the upper tier. Because this is a two-way stream, similar information can also be transferred back to inform the lower case. The secret to transferring uncertainties from one tier to another is to find the relationship of uncertainties between the 2 domains. These relationships can be based on model parameters. The information transfer from one brick to another brick is treated differently than the transfer of information from the lower tiers to the overarching problem. Model parameters are the vehicle of transfer for both of the

above cases. However, for brick-to-brick transfer, the output for the model parameter range from one VUQ run acts as input in the receiver brick. This is not true for the overarching analysis. In the case of overarching analysis, all of the lower levels are considered different dataset points of one system, and a global consistency analysis is performed on a combined set of experimental data. The output from this analysis will give a range of model parameters which can be used for overarching problem prediction with a high degree of confidence. Individual bricks in the hierarchy are linked via a common active model parameter for performing interlevel validation analysis. For linking any set of bricks, scenario parameters can also be used, along with model parameters. One can link as many levels as necessary with this method and can calculate a consistent region for the system as a whole. Figure 4.2 shows an example of a random nature of linkage between bricks based on a common parameter. In this example, A, B, and C are common variables, linking cases within the same level as well as cases from different levels. There may also be a case when a lower-level problem includes the physics used in the overarching problem, but it does not have any common parameter (Level 1-3 in Figure 4.2). These kinds of bricks are also useful, since validating them individually will improve confidence in the model as a whole for predictive purposes.

4.5. Experimental and Simulation Setup

4.5.1 Component-Scale Case

The experimental data used for this level were collected at the SANDIA National Laboratories in their Fire Laboratory for Accreditation of Models by Experimentation (FLAME) facility (Figure 2.8).

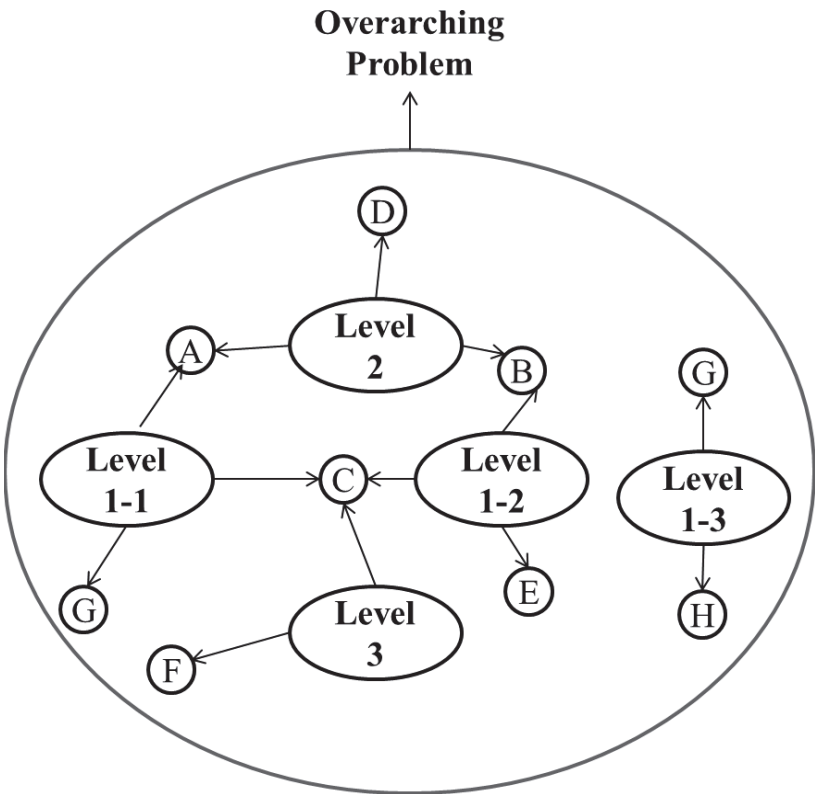

Fig 4.2: Intralevel and Interlevel Linkage in a Hierarchy

The central chamber is a 6.1 m^3 enclosure with a 2.4 m square chimney for outlet. The plume source at the center is at an elevation of 2.45 m from the floor. The facility is enclosed on all sides except for inlet air ducts. The diverters, screens, and honeycombs are placed such that the inlet air forms an annular low-velocity inlet flow surrounding the helium-plume [14, 15, 61].

As seen in Figure 2.8, the experimental setup was simplified into a 4 m^3 enclosure with the helium inlet of 1 m diameter at 0.25 m height from the bottom. This size was created after comparing the effects of wall distance on the airflow in order to find an optimum domain size with regards to run time and result accuracy. The ground in the simulation was an inlet for airflow, and its characteristics were calculated based on the mass balance of the original airflow specs. The experimental mixture of helium, acetone,

and oxygen, with the molecular weight of 5.45 g/mol, was used in the simulation. The side surfaces were modeled as walls and the top as a pressure outlet. The domain was meshed using a trimmer meshing scheme, which ensured that the resulting mesh was composed primarily of hexahedral cells, with trimmed cells next to the surface. Trimmed cells are hexahedral cells with one or more corners and/or edges removed. Figure 2.9 shows the 8 million cell mesh. The large, state-of-the-art cluster, Ember [62], was used to run simulations in parallel.

The unsteady LES calculations were set up to run implicitly with a segregated flow solver. For the first 2 seconds of flow, a time step of 0.05 seconds was used to set up a flow field in the domain. Then the step size was reduced to 0.0005 seconds for the next 3 seconds, thereby allowing for the computational flow transitions to reach quasi-steady flow conditions. Results from the next 5 seconds of simulation were processed to produce time-averaged quantities. The statistical stability was checked before using the results in any analysis.

4.5.2. Pilot-Scale Case

The second tier of the system is comprised of wind-tunnel experiments performed at the Flare Testing Facility (FTF) at CANMET, Ottawa. This facility uses a high speed fan to produce a range of crosswind speeds in a tunnel. The main chamber is 1.2 m wide and 8.2 m long, with a ceiling height of 1.8 m. The 4″ carbon steel flare pipe is 40″ long [79]. The facility is illustrated schematically in Figure 3.2.

The composition of fuel coming in through the flare pipe at 20 Kg/h was (vol %): CH_4-95.33, C_2H_6-2.1, C_3H_8-0.13, C_4H_{10}-0.02, N_2-1.8, CO_2-0.62. The experimental data were measured in the stack, using a 0.46 m sintered metal tube placed at the centerline

[17]. The combustion efficiency was determined by the ratio of carbon as CO_2 in the stack gas (excluding the amount of any CO_2 that came in with the inlet air) to the carbon present in fuel gases [79]. Figure 3.4 shows the domain and meshing scheme used for the simulations. Fuel exited the pipe at 300K. The left boundary was the cross-flow inlet. Here, the air came in at 287 K and contained 350-400 PPM of CO_2, similar to the current concentration in the atmosphere. This CO_2 was taken into consideration while computing the combustion efficiency. The domain was meshed using a trimmer meshing scheme with approximately 10.5 million cells (Figure 3.3). In order to keep the problem size realistic for such a huge domain, regions with mostly steady flow received coarser mesh.

4.6. Application of V&VUQ on the Hierarchy

4.6.1. Verification

Along with validation and uncertainty quantification, the Method of Manufactured Solution (MMS) approach was used to verify the code in the authors' previous work [77]. Manufactured solutions allow for arbitrary complexity in the solutions because they have no physical meaning and are created to verify all parts of the equation [3, 60]. This study not only ensured that code behave mathematically as intended, but also helped to decide the meshing scheme for the simulations. The current paper focuses primarily on the validation and uncertainty quantification part of the cycle.

4.6.2. Validation Framework

This step is important for providing quantitative and reliable uncertainty bounds on predictions from the simulations. The 6-step framework [31] was combined with a Monte-Carlo approach that provided upper and lower bounds of the prediction. This

section will define the steps of the framework, complete with their application on overarching problem. All the variable types and parameters present in a known system were classified into four major categories for the purpose of the VUQ study in this paper:

- *Active variables*: These subsets of parameters have a measurable influence on the property of interest. They consist of both model parameters and scenario parameters.
- *Design/Manipulated variables*: These are sets of variables that are changed by the experimentalists to create various scenarios for experiments—for example, locations of data collections in a system. In the terms of validation studies, these are the variables that distinguish between dataset units.
- *Controlled variables*: A variable that is kept fixed during the course of the experiment and strongly influences values is known as the control variable. It is held constant in order to test the relative impact of an independent variable. These variables can also be known as inactive scenario parameters.
- *Extraneous variables:* All other variables present in the systems are known as extraneous variables. They may introduce noise but do not systematically bias the results.

The applied framework is as follows:

Step 1: Create a list of model inputs and parameters with linked uncertainties or ranges (Input/Uncertainty (I/U) map) [64].

This step organized the known and unknown about the model. The I/U map consisted of a list of inputs with their importance rankings. It also included the uncertainties for each input and its current treatment status in the model. The dynamic

I/U map may be revisited after running other steps to update the information. The majority of the parameters that might affect the final measurements were included in the map. Because of the long list, the most important parameters were ranked to help construct the validation process. These rankings were based on previous work and experiences and were organized in a scale of 1-5, in order of increasing impact on the prediction error. Tables 4.1 and 4.2 show the I/U map for the helium-plume and wind-tunnel flare, respectively. For the helium-plume, 3 parameters were given impact factor 4 and 5. These 3 parameters were chosen as active variables. The distance of the inlet from the wall was reduced, as compared to the actual dimensions of the facility, to a point where it did not affect final results. This helped reduce the overall computational cost. Also, an optimum mesh size was finalized before running the cases. One of the parameters chosen for helium-plume analysis was turbulent Schmidt number. This number describes the momentum/scalar interactions in the flow. The modeling difficulty related to this parameter was highlighted by the wide range of values used in the literature [65- 69]. Xin et al. [67] have used 0.4 for Sc_t to create better predictions for the simulation of a methane pool fire and stated that Sc_t does not have a significant influence. On the other hand, Jiang and Campbell [68] have reported a wide range (0.2 to 0.85) of values and have highlighted their effect on flow field predictions. Wen et al. [69] and Zhang et al. [66] give completely different recommendations and claim the choice Sc_t is unimportant, compared with other variables. Due to such varied recommendations, the turbulent Schmidt number was selected for investigation of an optimum range and effect on the results for the helium-plume simulations. Similar to the helium-plume case, 3 parameters with impact factors of 4 and 5 were chosen as active variables for analysis of

Table 4.1: I/U Map for 1 m Helium-Plume

INPUT		IMPACT	UNCERTANITY	CURRENT STATUS
Geometry	Pipe diameter	1	Unspecified	1 m
	Wall distance from Inlet	3	Unspecified	Sensitivity analysis/optimized
	Outlet height	1	Unspecified	optimized
Input	Helium velocity	5	20 %	controllable
	Air co-flow	5	20 %	controllable
Model Parameters	Turbulence Sc number	4	[0.5-1,89]	Set by modeler
Numerical Parameters	Mesh	2	Unspecified	Convergence/speed compromise
	Boundary conditions	1	Unspecified	Fixed
	Initial conditions	1	Unspecified	Fixed

wind-tunnel flares. The experimental data not only showed variation with changing crosswind velocity, but it also measured at multiple crosswind velocities. The choice of crosswind velocity as an active variable is notable, as it was also a design variable. This created an excellent opportunity to test the framework for the analysis of uncertainties in multiple directions. Various researchers in literature [8-13] have also identified crosswind as an important factor for variable combustion efficiencies of flares.

Table 4.2: I/U Map for Wind-Tunnel Flare

INPUT		IMPACT	UNCERTANITY	CURRENT STATUS
Geometry	Pipe diameter	1	Unspecified	Fixed(4 inch)
	Pipe height	1	Unspecified	fixed
Input	Fuel velocity	1	Unspecified	fixed
	Crosswind velocity	5	[3.34-11.26] m/s	controllable
Model Parameters	Turbulence Sc number	4	[0.5-1.89]	Set by modeler
	Turbulence Pr number	4	Unspecified	Set by modeler
	Source term scaling factor (α)	5	[1-12.071]	Set by modeler
Numerical Parameters	Mesh	2	Unspecified	Convergence/speed compromise
	Boundary conditions	1	Unspecified	Fixed
	Initial conditions	1	Unspecified	Fixed

The second active variable chosen was a model parameter, which scaled the reaction-rate source term in the combustion model. This term controls the extent of combustion for a given condition, which, in turn, affects the efficiency. So determining a correct value of a source term is important. Turbulent Schmidt number (Sc_t) and Prandtl number (Pr_t) are 2 other variables with high ranking. Of these 2 variables, the current analysis only included $Sc_{t,}$ since it was also chosen in the helium case. This allowed the I/U map to take advantage of the information/output from the helium-plume analysis, while setting up the priors for the wind-tunnel case. This also showed an example of information transfer between the levels, the main focus of the current paper. The Pr_t may be included in future work, thus increasing the scope of the design of experiments and linking them to another experimental dataset. The way the framework was constructed, current results may be used for future analyses. Additionally, an optimum mesh size was finalized before running the cases.

Step 2: Define an evaluation criteria.

A model is evaluated for its quantity of interest, i.e., according to the context. This step includes specifying an evaluation criterion (or criteria) for model output and determining the domain of input variables over which evaluation of the model is desired. For the helium-plume case, favre-averaged centerline velocity at 3 different heights (0.2, 0.4, 0.6 m) from the inlet was assessed as evaluation criteria. At these heights, the data for 65 radial locations were averaged at 2 perpendicular single cell rows in x and y direction. While for the wind-tunnel flare, mass-averaged values of stack gas composition measured at 2 perpendicular 0.46 m long cell rows at the centerline of the stack were assessed as evaluation criteria. This choice was based on the experimental data. Also, the

experimental procedure and data collection helped to decide the range of chosen active variables.

Step 3: Collect the data and create a design of experiments.

Data were collected by preparing a Design of Experiments (DOE). This approach helped in effective and useful data collection for performing VUQ analysis. This paper did not use any standard method to create DOE. The variable space was strategically filled on the go to capture detailed information in the most impactful regions and create an optimum-sized DOE. For the wind-tunnel flare and helium cases, a DOE was prepared for 3 active variables. Tables 4.3 and 4.4 show the comprehensive design matrixes for wind-tunnel flare and helium-plume, respectively.

Step 4: The computer model output was approximated.

Validation process requires multiple code evaluations. The high cost of each LES simulation combined with the Monte-Carlo sampling procedure for the consistency test necessitated the use of an LES surrogate. Creating a good surrogate model is an important step in validation, since a bad surrogate model can insert additional errors and create relationships between variables which are not present in reality. These models must not only be a good mathematical fit but also follow the real physics accurately. The pioneers of surrogate models were Box and Wilson [70], who developed an approach known as Response Surface Methodology (RSM) in which polynomial surfaces are used to represent output. While polynomials are generally reliable and thus widely used, in the case of sparse data, a polynomial can insert additional information in terms of trends and physics between 2 points. This drawback was overcome in the current paper by the use of a flexible interpolation method, Delaunay Triangulation.

Table 4.3: Design of Experiment for Wind-Tunnel Flare System

Sim#	**Crosswind velocity (m/s)**	**alpha (α)**	**Sc_t**	**Sim#**	**Crosswind velocity (m/s)**	**alpha (α)**	**Sc_t**
1	3	1	0.9	21	3	1	0.4
2	4.4	1	0.9	22	8.2353	1	0.4
3	6.9563	1	0.9	23	12	1	0.4
4	9.5144	1	0.9	24	3	6	0.4
5	12	1	0.9	25	5.12	6	0.4
6	6.4265	5	0.9	26	8.2353	6	0.4
7	8.2353	5	0.9	27	12	6	0.4
8	10.12	5	0.9	28	3	12.071	0.4
9	3	6	0.9	29	8.2353	12.071	0.4
10	4.4	6	0.9	30	12	12.071	0.4
11	12	6	0.9	31	3	1	2
12	6.9563	10	0.9	32	8.2353	1	2
13	9.5144	10	0.9	33	12	1	2
14	3	12.071	0.9	34	3	6	2
15	4.4	12.071	0.9	35	5.12	6	2
16	5.12	12.071	0.9	36	8.2353	6	2
17	6.4265	12.071	0.9	37	12	6	2
18	8.2353	12.071	0.9	38	3	12.071	2
19	10.12	12.071	0.9	39	8.2353	12.071	2
20	12	12.071	0.9	40	12	12.071	2

Table 4.4: Design of Experiment for Helium-Plume

Sim#	V He (m/s)	MF Air (kg/s)	Sc_t
1	0.29	0.355	1.894
2	0.36	0.355	1.894
3	0.29	0.755	1.894
4	0.36	0.755	1.894
5	0.29	0.355	0.508
6	0.36	0.355	0.508
7	0.29	0.755	0.508
8	0.36	0.755	0.508
9	0.29	0.555	0.8
10	0.385	0.555	0.8
11	0.325	0.208	0.8
12	0.325	0.901	0.8
13	0.325	0.555	100000
14	0.325	0.555	0.4
15	0.325	0.555	0.8

In addition to being computationally less expensive, Delaunay Triangulation ensures boundedness, without being affected by the sampling order [71, 72]. This method is also superior in feature capturing, since all original data points are located on the surrogate surface only.

Step 5: The consistency was measured.

This step drew on prior information and exploited a consistency requirement. The consistency constraint was exploited among the available experimental datasets and simulations of such sets to quantify the uncertainty in model parameters, boundary conditions, and experimental error and simulation outputs to produce predictivity [73]. Using this approach, the uncertainty interval for the data was obtained, which in turn was used as the likelihood in the consistency analysis. The most sensitive parameters were then identified and used in the subsequent quantification of predictivity. The consistency constraint used to measure and produce a posterior uncertainty consistent with all experimental and simulation data was defined as [49]:

$$\begin{cases} C_{\aleph} = \min \gamma \; subject\ to\ constraints: \\ \beta_i \geq x_i \geq \alpha_i \,, for\ i = 1, \ldots\ldots, n \\ (1-\gamma)u_e \geq |y_m(x) - y_e| \geq l_e(1-\gamma), for\ each\ e \in \aleph \end{cases} \tag{4.2}$$

where α_i , β_i are upper and lower uncertainty bounds of input parameter x_i , y_m is the model value, and y_e is the experimental value. u_e and l_e are the upper and lower bounds of experimental uncertainty or deviations. Equation 4.2 makes sure that all simulations are bounded by their individual experimental uncertainty. The term (1- γ) is added to the equation to make sure that we can quantify the consistency of the model. Each dataset point is checked through the constraint and value for (1- γ) is stored. C_D denotes the

largest value of (1- γ). It gives a measure of an overall consistency of the dataset. The smaller value of C_D corresponds to better consistency.

The major difference between Data Collaboration (DC) and the consistency test used here was that it uses a pseudo-random selection of points (the Monte-Carlo method) to solve a similar set of equations, rather than the domain decomposition iterations of DC. The consistency test employs following steps:

1) The range of active variables was specified.
2) Experimental data were sampled in order to find any uncertainties present. This was computed through mean and standard deviation with a user-specified confidence range.
3) Using Monte-Carlo sampling, a feasible region for active variables was obtained between the provided ranges.
4) The model was then evaluated at each of the sample points and for each of the experiments or scenarios.
5) A consistency analysis was performed by subjecting the results to the constraints (Equation 4.2). This step revealed how well the evaluated values matched the experimental values. For a point to be called consistent, it needed to satisfy the inequalities for each of the experiments.

Step 6: Feed information back into current validation exercise and feed information forward into future validation activities.

This step used the results from Step 5 to improve the model, as well as to refine the aspects of the validation process. The results were analyzed to highlight the impact region in variable space, thus helped in populating the DOE points.

4.6.3. Validation and Uncertainty Quantification

4.6.3.1. Component-Scale: Helium-Plume Case

The validation results in this section were taken from the author's previous work, in which the helium case was individually examined for consistency [77]. Each step of the framework was followed in a systematic manner, and favre-averaged values were calculated from the simulations. The simulations used a time step of 0.0005 seconds. Data were collected at 5-10 seconds of flow time. This time interval of 5 seconds provided statistical reliability and was finalized by calculation of moving point average at the centerline point. Based on grid refinement studies [77], a mesh size of 8 million cells was used. All the simulations were run on 360 to 420 processors. After converting the simulation results into the experimental data format, a consistency analysis was performed using the Monte-Carlo Consistency test. This analysis was completed by varying the 3 chosen active variables. 50,000 pseudo-random points were selected within the range of these variables and results for each point were put to the consistency constraint. Table 4.5 shows the range of parameters over which the dataset was consistent along with the most consistent point and overall consistency measure of the dataset. Figure 4.3 illustrates the comparison between the experimental data and the model data along with the common consistent region for all 3 heights. Figure 4.4 shows the points in the active variable space which satisfy all the constraints. The color scheme denotes the value of $(1-\gamma)$, with 0 as the most consistent point and 1 as the edge of consistency. With regard to the colors themselves, blue is the most consistent and red is at the edge of consistency.

Table 4.5: Results for Helium-Plume Case

Helium inlet range for consistent data	0.32 m/s to 0.36 m/s
Most consistent helium inlet value	0.349 m/s
Air co-flow range for consistent data	0.355 Kg/s to 0.70 Kg/s
Most consistent air co-flow value	0.46 Kg/s
Sc_t range for consistent data	0.61 to 1.89
Most consistent Sc_t value	0.99
Overall consistency measure, C_D	0.651

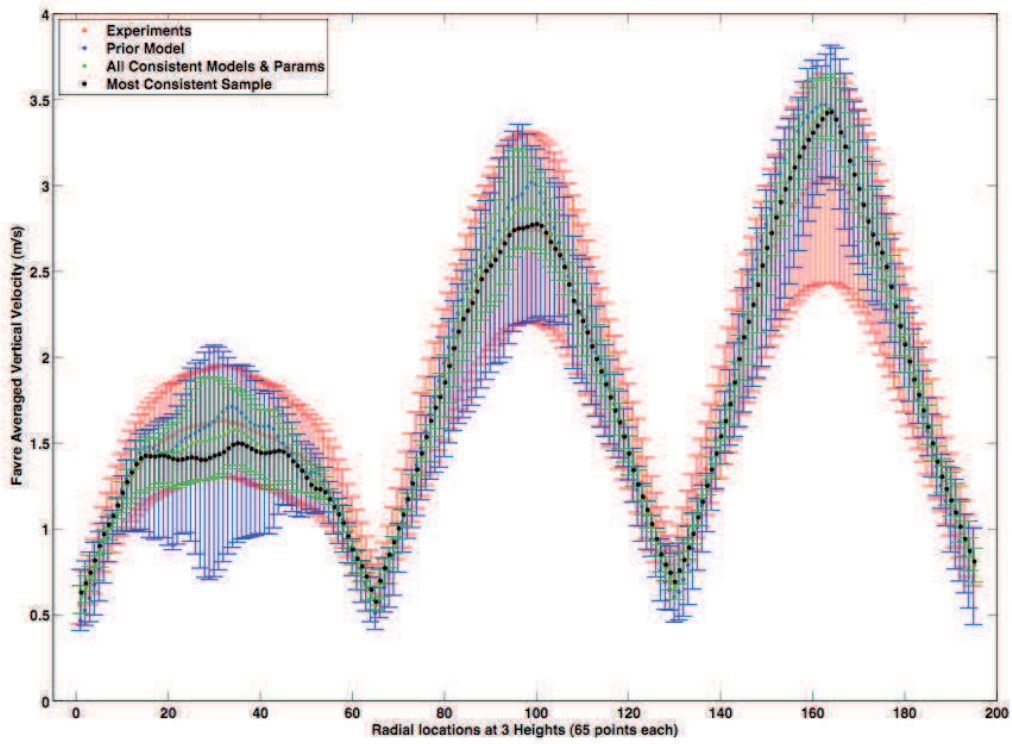

Fig 4.3: Error Bars for 195 Points at 3 Different Heights to Show the Consistent Space

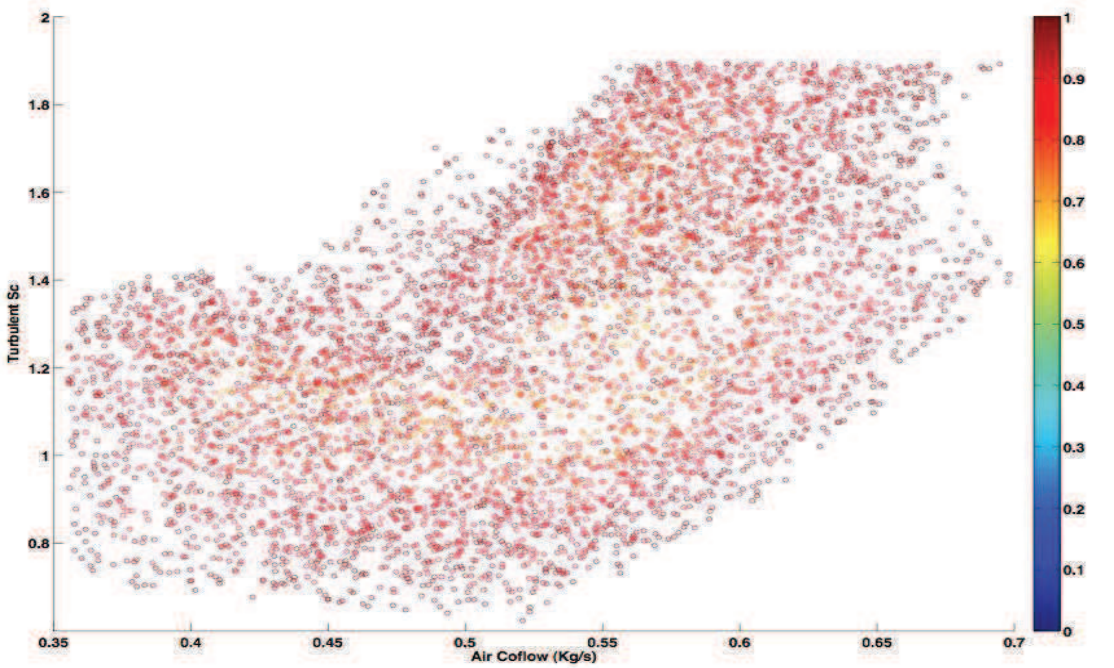

a)

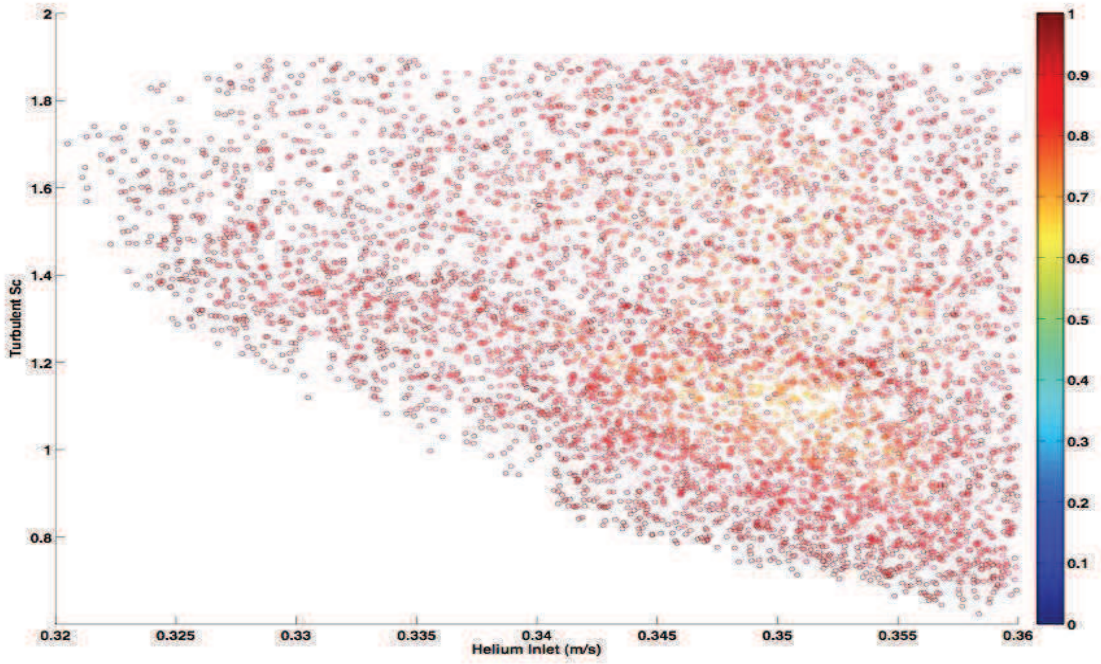

b)

Figure 4.4: Consistent Region for 3-D Helium Case a) Consistent Region in Sc_t & Air Flow Space b) Consistent Region in Sc_t and Helium Inlet Space

4.6.3.2. Pilot-Scale: Wind-Tunnel Flare Case

This section describes the validation of the pilot-scale level of the hierarchy. The wind-tunnel flare system was simulated with various crosswinds, source-term scaling factor, and Turbulent Schmidt number, as described in the design of experiments. These simulations were carried on 480-600 processors. For the initial 3 seconds, a time step of 0.05 seconds was used to set up a flow filed in the domain. Then the time step size was reduced to 0.0005 seconds. The next 3 seconds allowed for computational flow transitions to reach quasi-steady flow conditions. After the establishment of a developed flow, the mass flow average values of the desired quantities were collected at the measurement location (Figure 3.3) for 4 seconds. Typically, the computational time varied between 190 hours and 240 hours. The combustion efficiency computed from the model is given by progress variable C. The details of combustion efficiency data can be found in the author's previous work [17]

After converting simulation results into the experimental data format, consistency analysis was performed using the consistency test. This was done by varying all 3 active variables (crosswind velocity, source term scaling factor, alpha, and Turbulent Schmidt number). 500,000 pseudo-random points were selected from a uniform distribution of active variables, and result for each point was tested against the consistency constraint. Before performing consistency analysis, the experimental data were analyzed and crosswind velocities were divided to create 6 dataset units. The members of each group were meant to be replicates. This approach helped compute the uncertainty in the values of measured variables (efficiency, CO_2, O_2, CO etc.), as well as the crosswind velocities. Since data are very sparse, a confidence interval of 1.5 was used for experimental

uncertainties. The analysis was completed for CO_2, O_2, and CH_4 concentrations only. Since the combustion efficiencies were calculated based on other measurements in the experiment, they were not tested against the consistency constraints, and were therefore computed for the consistent data points using the PVM model. CO was also excluded, since the applied combustion model did not account for quenching, which is a major source of CO generation.

Figures 4.5-4.8 show the prior and posterior consistent regions for measured variables. In these plots, red denotes the experimental data, and the box signifies the uncertainty region. Simulation results and their uncertainties are shown in green. This analysis has 6 different crosswind groups for 3 different desired variables (Concentration of CO_2, CH_4, and O_2), making a total of 18 dataset points. Each of the 500,000 points was checked for consistency in all 18 dataset units. Simulation results were consistent in all 6 groups for CO_2 and O_2 concentration, shown by the overlapping of prior and posterior regions in Figures 4.5-4.6. For the CH_4 concentration, simulation results were consistent for only 5 of 6 groups. Crosswind group 1, from 3.373 m/s to 3.932 m/s, shows a lower CH_4 concentration for the model (Figure 4.7). Hence the combustion efficiencies matched the experimental data well, except in the low crosswind group (Figure 4.8). In all, consistency over 17 dataset units was achieved. The discrepancy of CH_4 concentration for the low crosswind group may be either a model issue or a data collection issue. Since the model was able to generate results consistent with experimental data for CO_2 and O_2 concentration in this low crosswind case, we consider that maybe few of the experiments in the CH_4 dataset unit had errors in reporting.

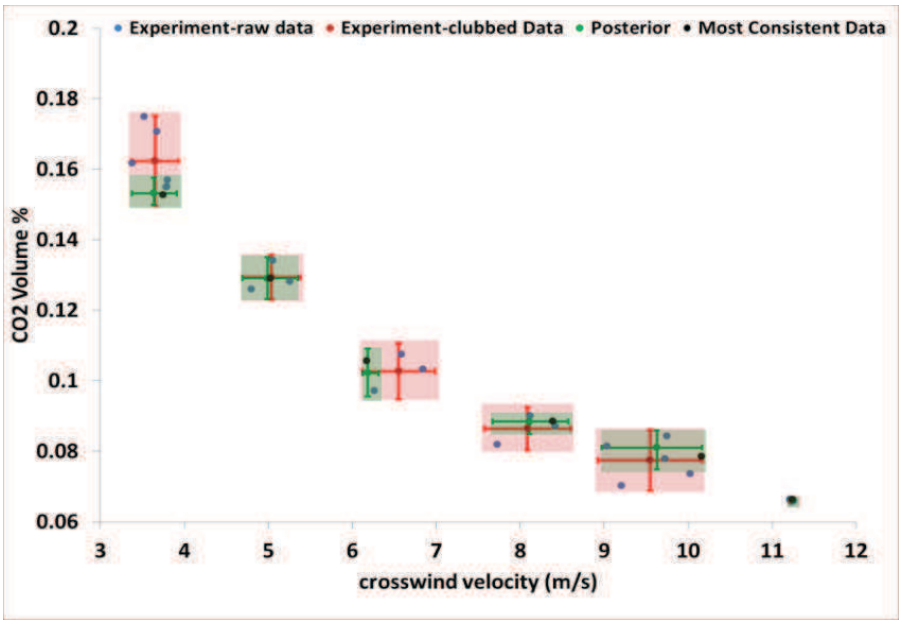

Fig 4.5: Prior and Posterior Consistent Regions for CO_2 Concentration in All 6 Groups

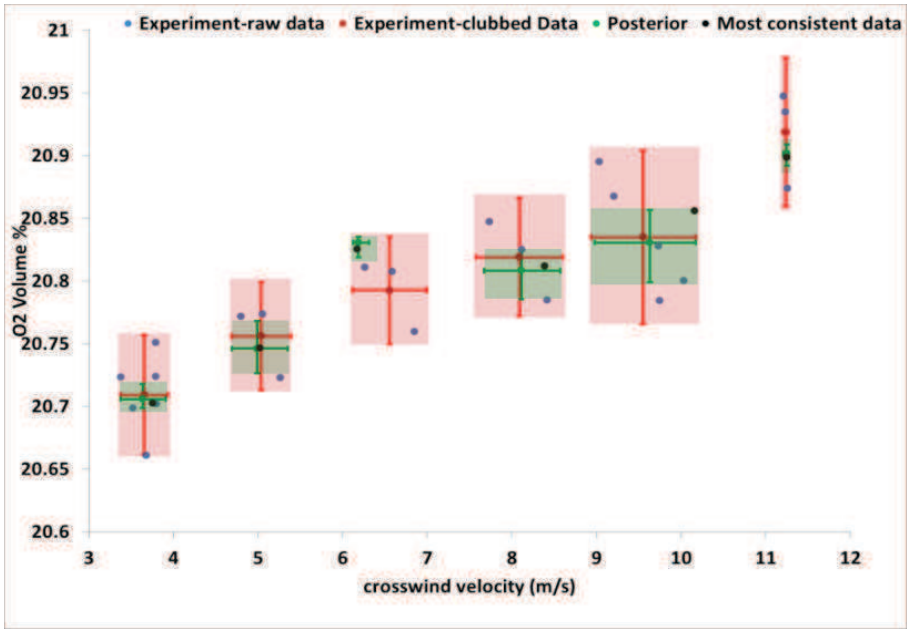

Fig 4.6: Prior and Posterior Consistent Regions for O_2 Concentration in All 6 Groups

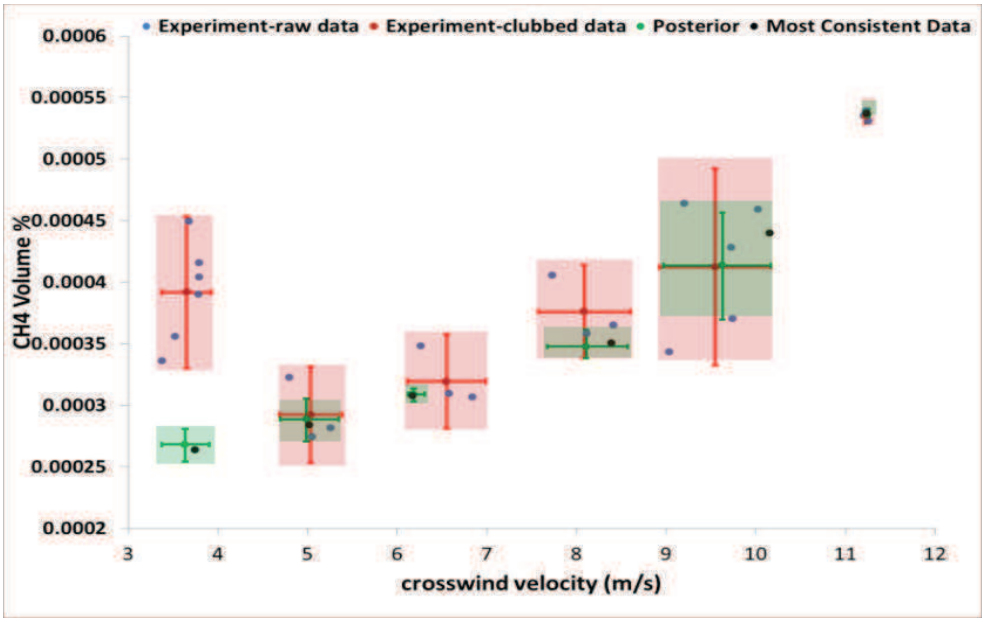

Fig 4.7: Prior and Posterior Consistent Regions for CH_4 Concentration in All 6 Groups

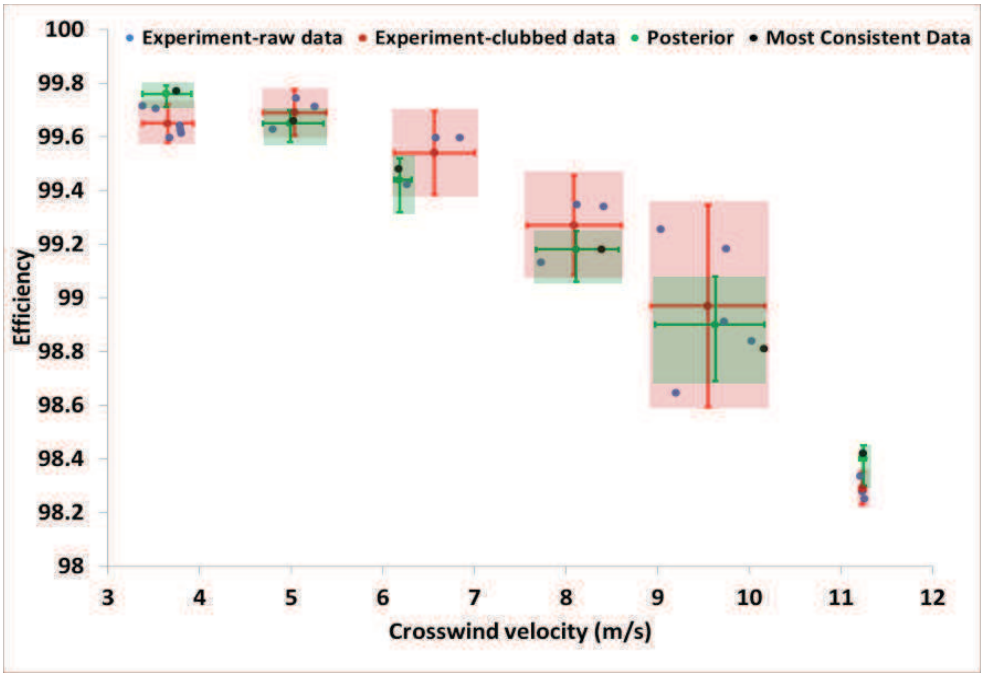

Fig 4.8: Prior and Posterior Consistent Regions for Combustion Efficiency in All 6 Groups

Experimental data suggest that as crosswind velocity decreases, efficiencies increase. Theoretically, increase in efficiency signifies more burned fuel and a higher conversion to CO_2. Though the data presented show an increase in CO_2 concentration, it does not show the decrease in CH_4. Another reason for this difference may be the measurement technique used in the simulations. As mentioned earlier, the values were averaged for couple of 0.46 m perpendicular row of single cells at the stack centerline which may not be capturing the complete picture here. This discrepancy requires both the experimentalist and the modeler to work together to identify and analyze the issue which caused the error.

Table 4.6 shows the range of alpha for consistent data and overall consistency measurement of this dataset. These ranges of model parameters can be used as prior information for future validation studies. These results, when compared to the validation study for the flare system performed using only 2 active variables [17], show that by increasing the active variables uncertainties can be reduced, and the model can be refined. In comparison to that analysis, the range for the model parameter alpha got refined for consistent results. Figures 4.9 and 4.10 show the consistency space for each of the 6 crosswind groups. They also give the range of alpha and Sc_t for which results are consistent.

Table 4.6: Results for Wind-Tunnel Flare System

Range of alpha for consistent data	7.15 to 9.2
Range of Sc_t for consistent data	0.878-0.97
Overall consistency measure, C_D	0.72

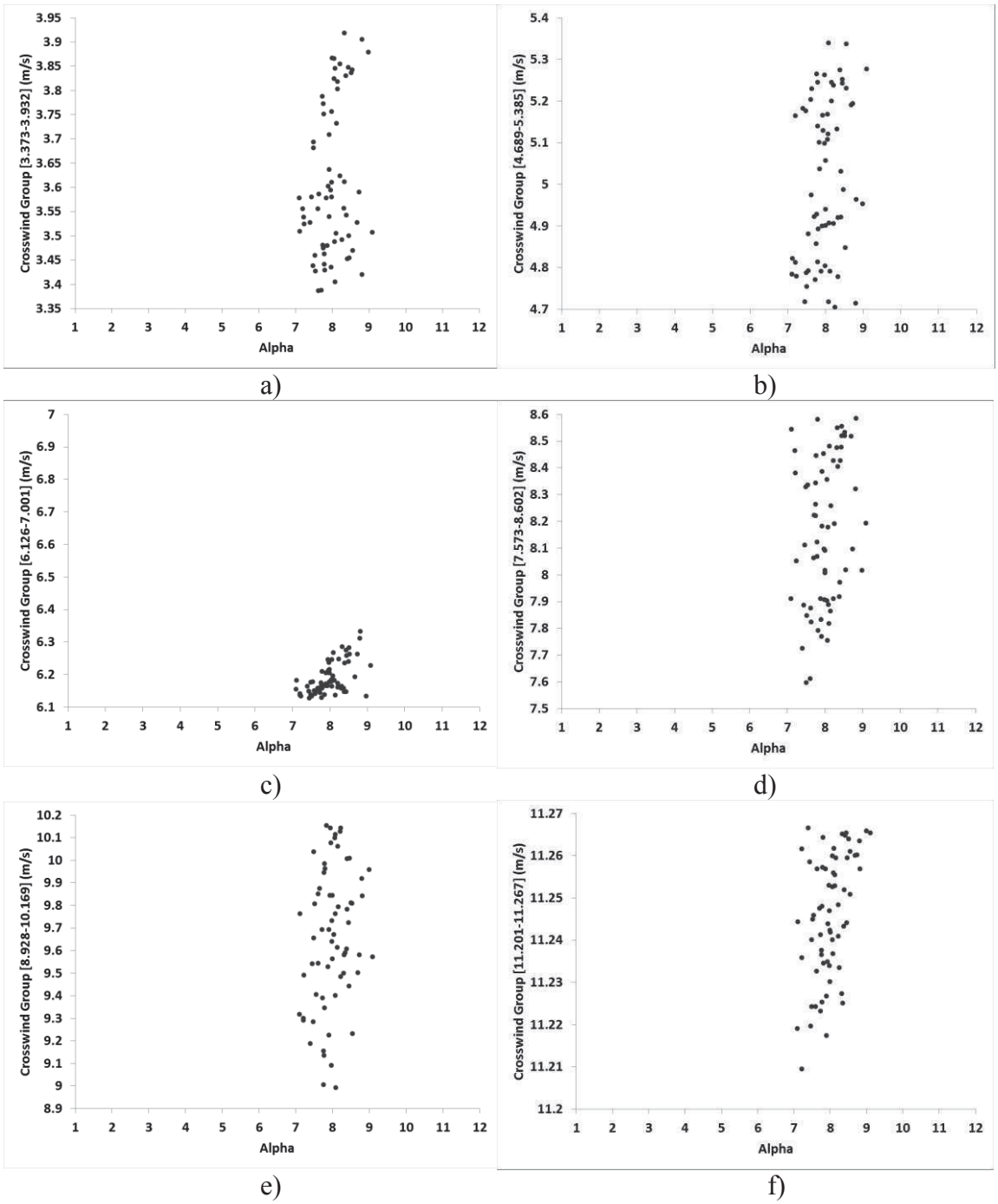

Fig 4.9: Consistency Region for All 6 Crosswind Groups in Alpha Space: a)[3.373-3.932], b)[4.689-5.385], c)[6.126-7.001], d)[7.573-8.602], e)[8.928-10.169], f)[11.201-11.267] m/s

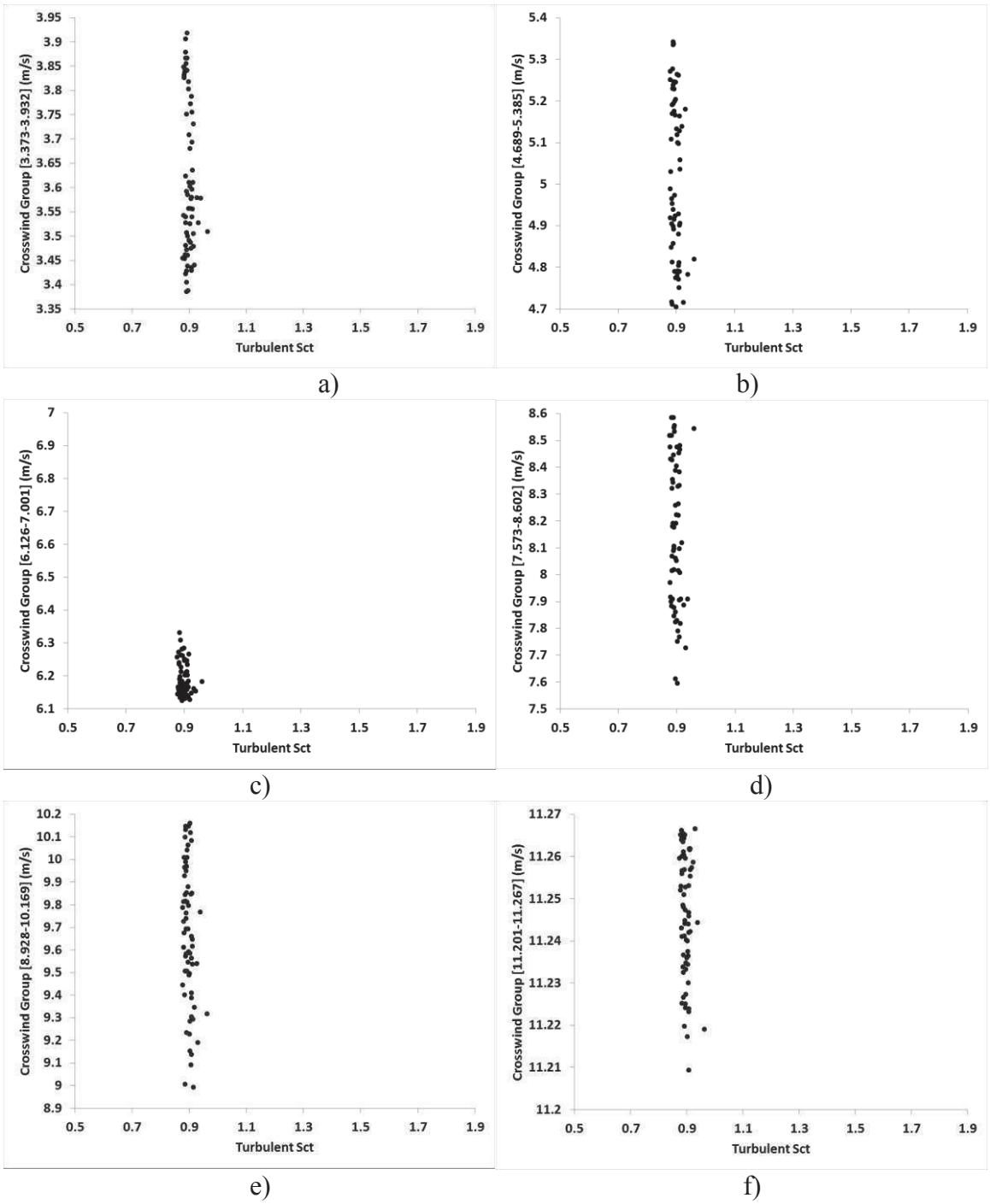

Fig 4.10: Consistency Region for All 6 Crosswind Groups in Turbulent Sc_t Space :a)[3.373-3.932], b) [4.689-5.385], c)[6.126-7.001], d)[7.573-8.602], e)[8.928-10.169], f)[11.201-11.267] m/s

4.6.3.3. Combined Validation

The individual-brick validations laid a good foundation for interlevel validation. In this section, the 2 levels, the component-scale and the pilot-scale, were linked in one validation analysis with the help of a model parameter Turbulent Schmidt number. All the experimental data went through the consistency constraints as one system. In total, there were 213 datasets (65 points each for 3 heights in the helium-plume case and 6 crosswind groups for 3 species compositions in the wind-tunnel flare). A total of 500000 random points were selected within the range of the active variables. The result for each selected point was tested through the consistency constraint. Figure 4.11 shows the consistency region in the variable space for the helium-plume case. Figure 4.12 compares the experimental data and the model data. The common consistent region for all 3 heights is also shown. After comparing these results with the results in Figures 4.3 and 4.4, it was observed that global analysis gives a smaller consistency space, thus more refined range for active variables were obtained for use in predictive modeling. Table 4.7 shows range of active variables over which the entire system is consistent and overall consistency measurement for the whole system.

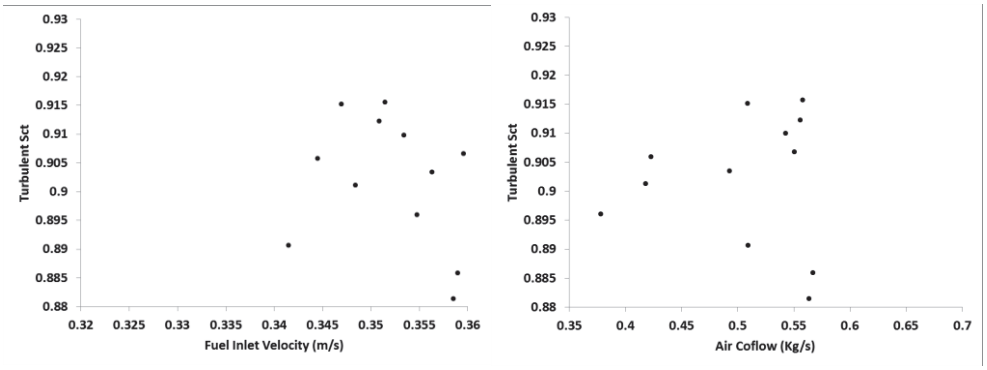

(a) (b)

Figure 4.11: Consistent Region for 3-D Helium Case a) Consistent Region in Sc_t and Helium Inlet Space b) Consistent Region in Sc_t & Air Flow Space

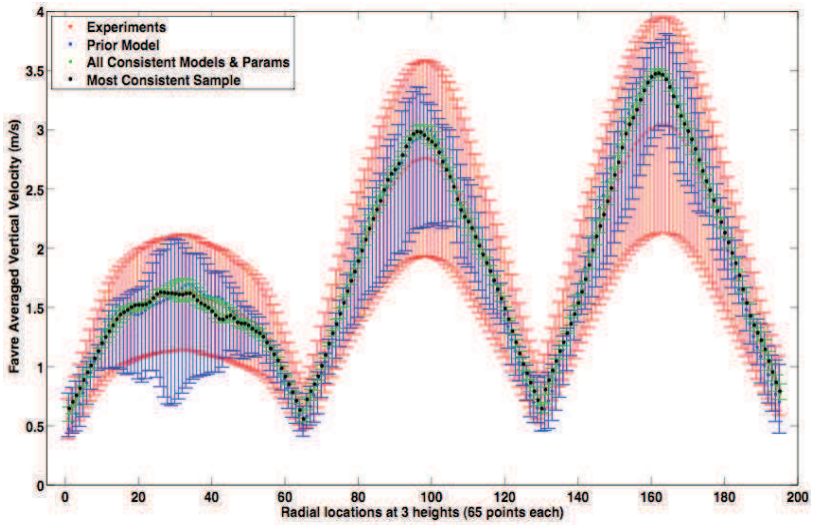

Figure 4.12: Error Bars for 195 Points at 3 Different Heights to Show the Consistent Space for the Helium-Plume Case.

Table 4.7: Consistency Analysis Results for the Combined Validation

Component-scale : Helium-plume	
Helium inlet range for consistent data	0.342 m/s to 0.36 m/s
Most consistent helium inlet value	0.35 m/s
Air co-flow range for consistent data	0.355 Kg/s to 0.55 Kg/s
Most consistent air co-flow value	0.46 Kg/s
Sc_t range for consistent data	0.882 to 0.918
Most consistent Sc_t value	0.89
Pilot-scale: Wind-tunnel flare	
Range of alpha for consistent data	7.45-8.68
Range of Sct for consistent data	0.882-0.918
Overall consistency measure, C_D	0.78

For the wind-tunnel flare case, Figures 4.13-4.15 show the prior and posterior consistent regions for active variables, and Figure 4.16 shows the computed combustion efficiency in all 6 crosswind groups. In these plots, once again, red denotes the experimental data, and the box signifies the uncertainty region within it. Simulation results and their uncertainties are in green. Figures 4.17 and 4.18 illustrate the consistent region in active variable space. The attained range of alpha and Sc_t were an improvement upon the values obtained in local analysis of the pilot-scale level.

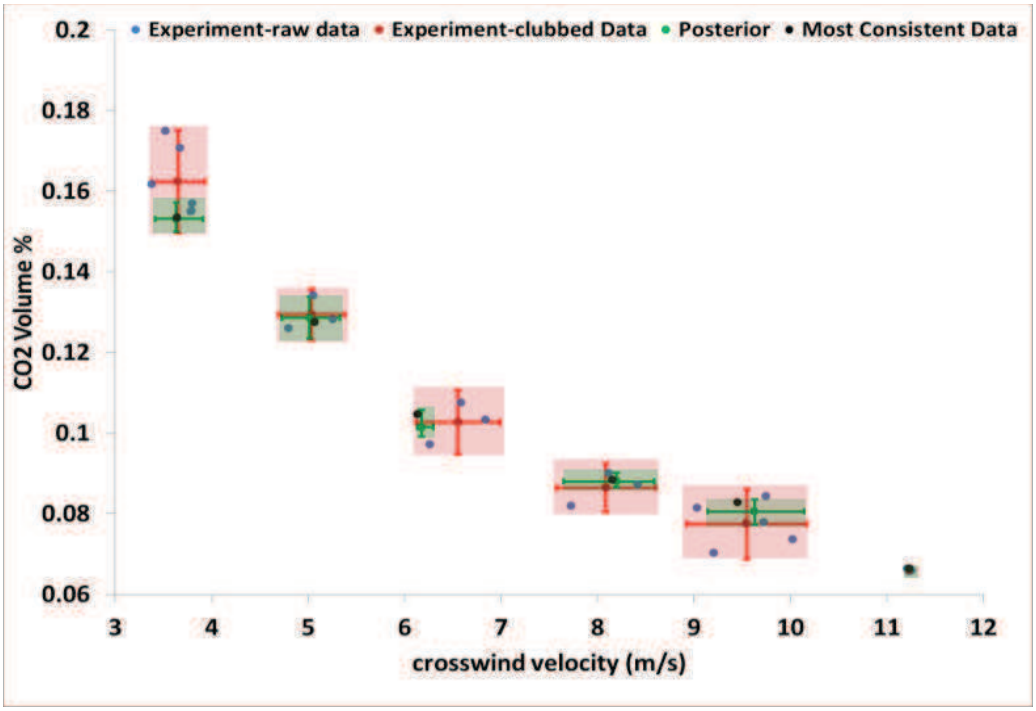

Fig 4.13: Prior and Posterior Consistent Regions for CO_2 Concentration in All 6 Groups

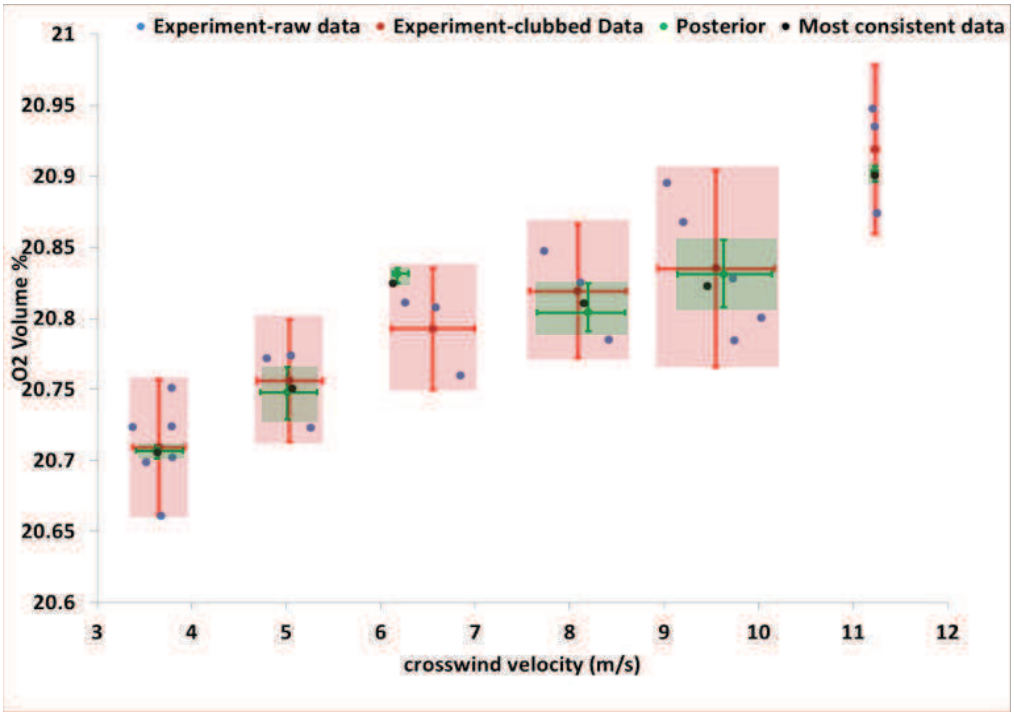

Fig 4.14: Prior and Posterior Consistent Regions for O_2 Concentration in All 6 Groups

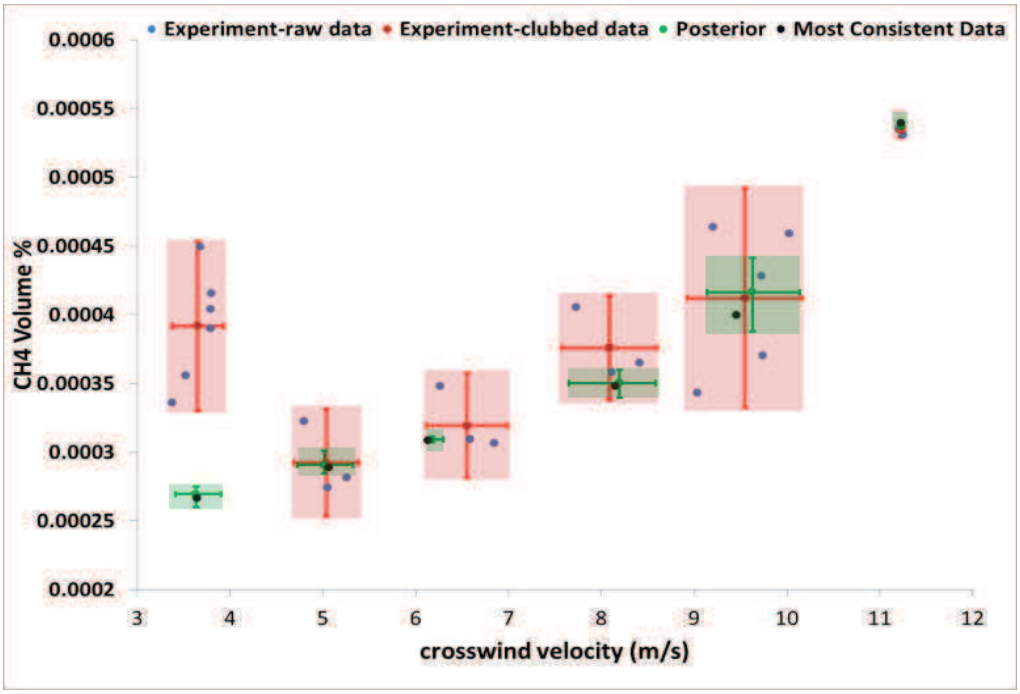

Fig 4.15: Prior and Posterior Consistent Regions for CH_4 Concentration in All 6 Groups

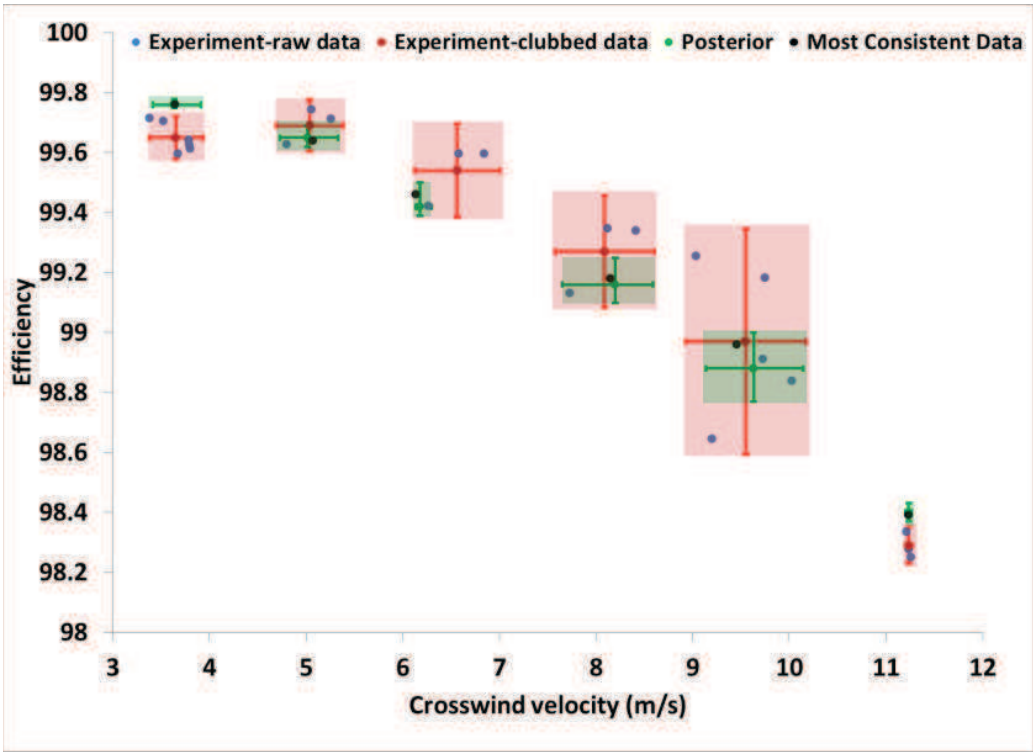

Fig 4.16: Prior and Posterior Consistent Regions of Combustion Efficiency for Global Analysis

The overall consistency measure C_D for this global analysis was measured at 0.78, which is higher than both individual brick C_D values. Although global analysis shows that the model is less consistent, it provides a much more accurate range for parameters where we can get consistent results. The output for all the model parameters can be used as input for the overarching problem. Their values were much more refined, compared with the values from a lower scale. By moving up in the hierarchy and performing local as well as global validation analysis, the uncertainty in model parameters was reduced. This, in turn, refines the model and increases confidence in the model. This can also be seen as the intersection of the model parameter range set from 2 local analyses.

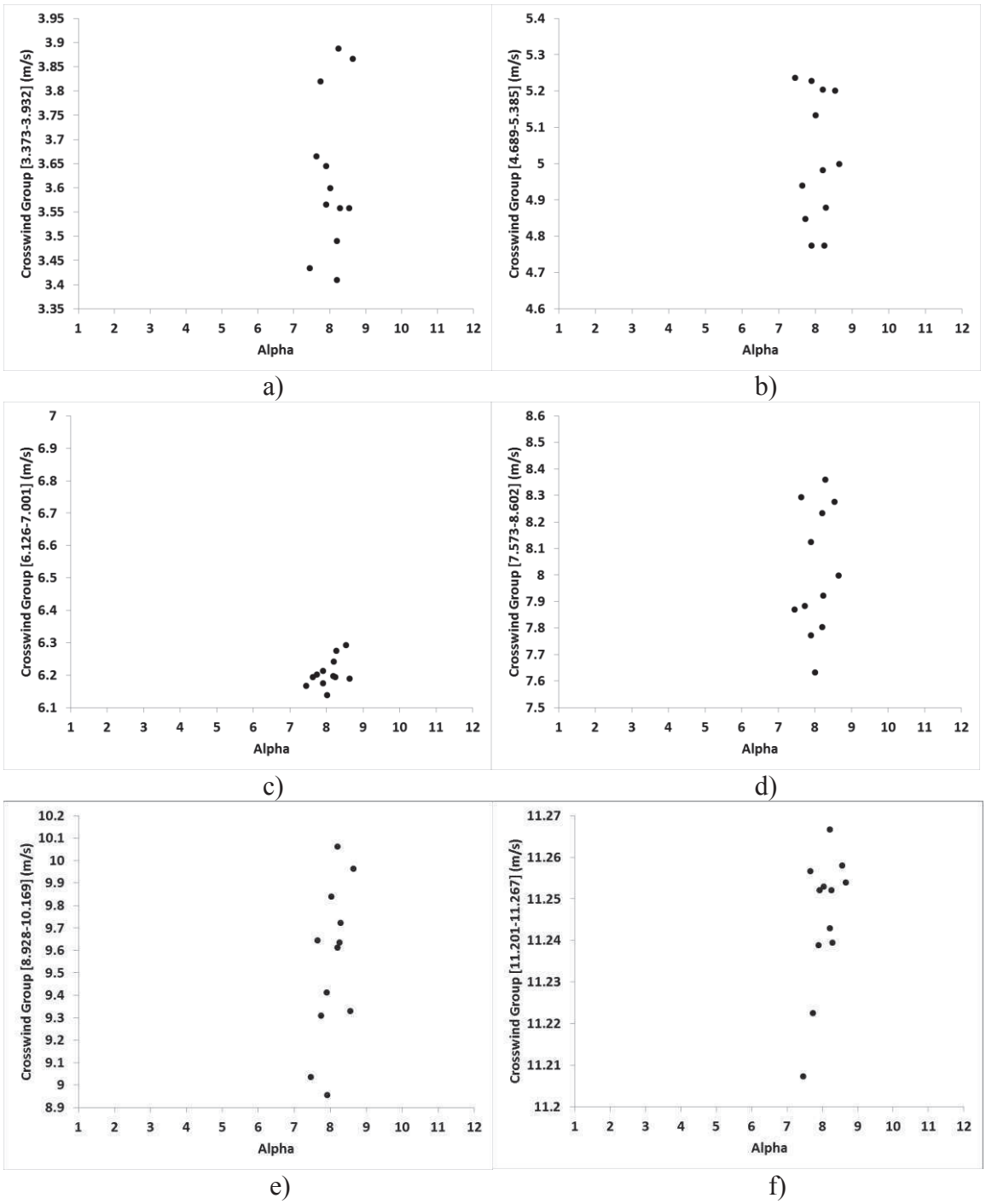

Fig 4.17: Consistency Region for All 6 Crosswind Groups in Alpha Space for Global Analysis: a)[3.373-3.932], b)[4.689-5.385], c)[6.126-7.001], d)[7.573-8.602], e)[8.928-10.169], f)[11.201-11.267] m/s

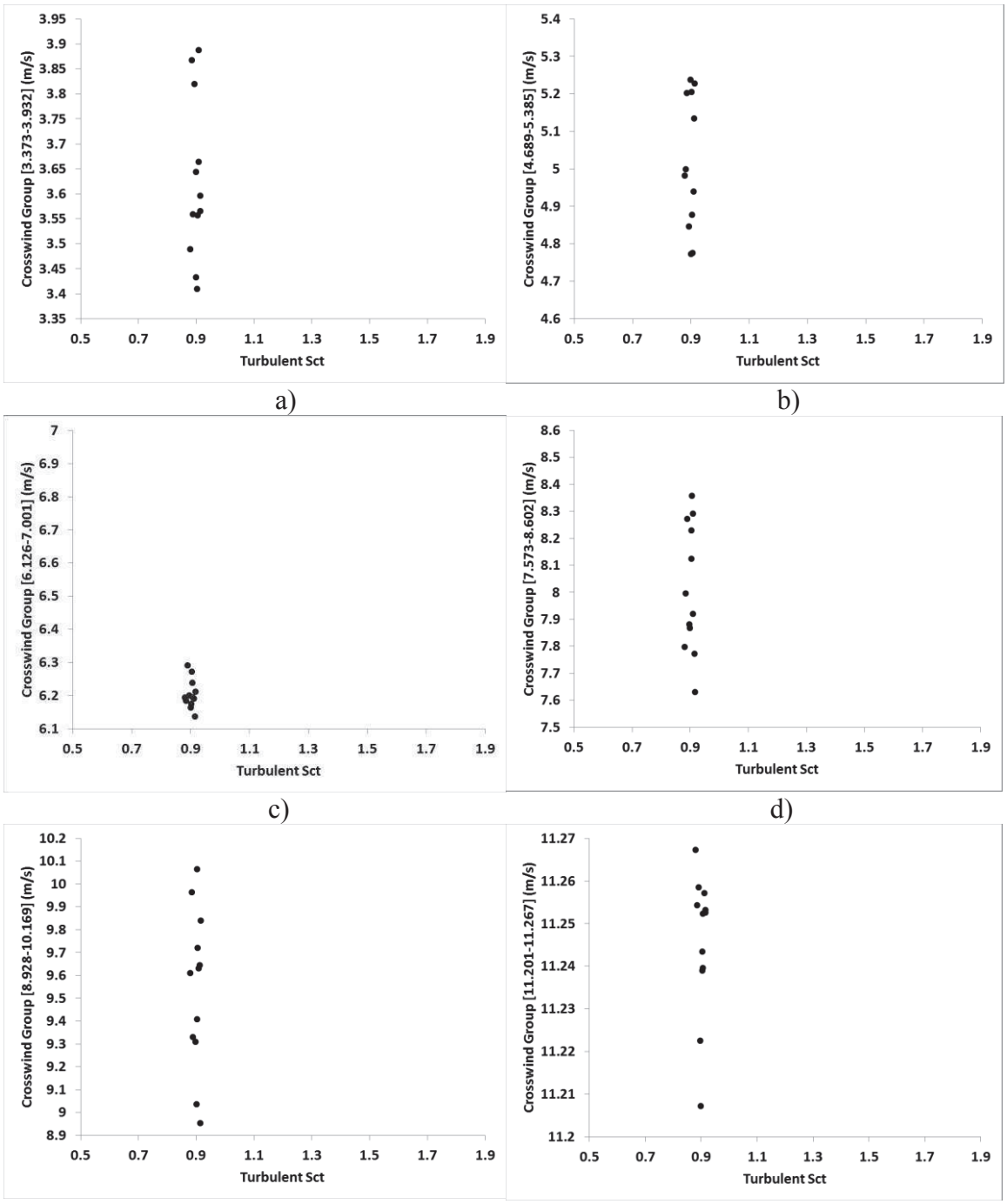

Fig 4.18: Consistency Region for All 6 Crosswind Groups in Turbulent Sc_t Space : a)[3.373-3.932], b)[4.689-5.385], c)[6.126-7.001], d)[7.573-8.602], e)[8.928-10.169], f)[11.201-11.267] m/s

4.7. Conclusions

The problem of building confidence in predictions for a problem without any experimental data was handled successfully in this paper. The model for measuring the combustion efficiency of an industrial flare system was improved, with the help of 2 smaller-scale problems: wind-tunnel flare system and buoyant helium-plume. A method for projecting uncertainties from one level to another was proposed. Also shown was the linkage of multiple levels of hierarchy, in order to perform a global validation analysis. Uncertainties in 2 model parameters were reduced by performing individual/local analysis and interlevel/global analysis. The range for the model parameter alpha [7.45-8.68] and Turbulent Schmidt number [0.882-0.918] was obtained for consistent results. With the extension of active variable dimensions and inclusion of more experimental data in the hierarchy, other model parameters may also be fine-tuned. The validation approach and results obtained suggest that this model is a positive step in predicting efficiencies for industrial flares with some confidence.

CHAPTER 5

CONCLUSIONS AND FUTURE WORK

This section provides a comprehensive summary of the conclusions from each of the preceding chapters and the recommendations for future work.

5.1. Conclusions

Chapter 2 was focused on presenting a systematic approach to address V&VUQ issues. A framework was adapted and applied on a buoyancy-driven 1 m helium-plume. The consistency of simulation results with the experimental results was checked and a measure of consistency was provided. The effect of dimensionally on the consistency measure was also demonstrated with a 2-D and 3-D analysis. A 2-D analysis used helium-plume inlet and air co flow as active variables and gave a C_D of 0.528 while for 3-D case turbulent Schmidt number was added to the list of active variables. The C_D for this case was 0.651. This analysis also showed the effect of turbulent Schmidt number on the results. The final output from the analysis refined the input parameter ranges for future VUQ analysis.

The next chapter was oriented towards measurement of combustion efficiency. A wind-tunnel system was chosen and an approach to tackle the hurdles with measurement of combustion efficiency was shown by the use of PVM combustion model. The measured quantities from this model were subjected to consistency analysis to increase the level of confidence in the predictions. Effect of crosswind on combustion efficiency

was also illustrated. The VUQ method used shows a way to handle the uncertainty in multiple directions. This case was different from the helium case for Chapter 2 in terms of treatments of variables and had a common design and active variable. With the help of this case, the range of model parameter alpha (source term multiplier) was estimated for consistent results.

Chapter 4 of the thesis uses the information from the first 2 chapters and showed a way to perform VUQ analysis for an overarching problem with no prior experimental data. A hierarchical approach was used to do the aforementioned analysis. Helium-plume and wind-tunnel flare systems were chosen as the subsystem of this hierarchy. A method to propagate the uncertainty and the confidence through the branches of hierarchy with the help of model or scenario parameters was proposed and illustrated. Along with the individual component VUQ, interlevel or global V/UQ was also performed by linking the subsystems. This analysis refined the range of the variables for consistent predictions and builds the confidence in the model.

5.2. Recommendations for Future Work

- The work in this research shows only one case in each sublevel of hierarchy to demonstrate the approach. More cases with common physics and experimental data can be identified and included into the VUQ hierarchy. This will lead to the better accuracy. One such component-level brick can be buoyancy-driven reacting turbulent methane pool fire.
- The VUQ analysis for each case can be repeated by updating the I/U map with the information gained from the previous iteration. This method will fine-tune the model and improve the confidence in the predictions.

- While repeating the VUQ analysis, the number of simulations in the DOE can also be increased to populate the feasible region and get better prediction.
- As seen in Chapter 3, the consistency analysis poses a question mark for one of the experimental datasets. This can be discussed with the experimentalist and can be used to develop model and experiment simultaneously.
- Finally, the output from the overall consistency analysis can be used to run simulations for a large-scale industrial flare like TCEQ (Texas Commission on Environmental Quality) flare study and combustion efficiencies can be predicted for them.

APPENDIX A

SIMULATION RESULTS

This appendix contains the simulation results for the design of experiment cases used for the validation analysis. Based on these results, a surrogate model was formed for the analysis. These results were presented in tabulated form. Table A-1 has results for wind-tunnel flare cases, and Table A-2 for helium-plume cases. The first 20 simulations in flare results with constant Schmidt number were used for a 2-D analysis and then the system was expanded for a 3-D analysis. The table for the helium-plume consists of values of vertical velocities at 65 radial locations for 3 heights above the inlet.

Table A-1: Results for Wind-Tunnel Flare Simulations

Sim#	Crosswind velocity (m/s)	Model parameter alpha (α)	Sc_t	CO_2 Vol %	CH_4 (E-4) Vol %	O_2 Vol %	Combustion efficiency
1	3	1	0.9	0.089	4.2524	20.8453	97.43
2	4.4	1	0.9	0.081	4.6789	20.8992	96.13
3	6.9563	1	0.9	0.1013	3.19	20.8769	95.20
4	9.5144	1	0.9	0.085	4.6	20.793	93.57
5	12	1	0.9	0.0534	5.518	20.9682	92.43
6	6.4265	5	0.9	0.0956	3.5754	20.8658	99.48
7	8.2353	5	0.9	0.0909	3.6559	20.8274	99.00
8	10.12	5	0.9	0.075	3.2808	20.8231	98.85
9	3	6	0.9	0.1581	2.8764	20.722	99.75

Table A-1: Continued

Sim#	Crosswind velocity (m/s)	Model parameter alpha (α)	Sc_t	CO_2 Vol %	CH_4 (E-4) Vol %	O_2 Vol %	Combustion efficiency
10	4.4	6	0.9	0.139	2.9982	20.714	99.70
11	12	6	0.9	0.0556	6.1592	20.9474	98.00
12	6.9563	10	0.9	0.0946	3.098	20.8679	99.44
13	9.5144	10	0.9	0.089	3.6362	20.8231	99.18
14	3	12.071	0.9	0.1702	2.1247	20.6852	99.86
15	4.4	12.071	0.9	0.1419	2.2354	20.6895	99.79
16	5.12	12.071	0.9	0.1335	2.5	20.7148	99.68
17	6.4265	12.071	0.9	0.1025	3.0939	20.7883	99.67
18	8.2353	12.071	0.9	0.0916	3.0175	20.8526	99.32
19	10.12	12.071	0.9	0.0835	3.3528	20.771	99.28
20	12	12.071	0.9	0.0584	6.6292	20.8931	98.23
21	3	1	0.4	0.09	3.1528	20.771	98.68
22	8.2353	1	0.4	0.088	4.1789	20.8092	96.58
23	12	1	0.4	0.0579	4.00	20.939	94.75
24	3	6	0.4	0.1612	2.248	20.7152	99.83
25	5.12	6	0.4	0.0942	2.98	20.8879	99.41
26	8.2353	6	0.4	0.0935	3.3528	20.771	99.25
27	12	6	0.4	0.0584	6.292	20.8931	98.23
28	3	12.071	0.4	0.1742	2.0248	20.652	99.95
29	8.2353	12.071	0.4	0.0996	3.0754	20.8258	99.56
30	12	12.071	0.4	0.0646	3.098	20.8679	99.42
31	3	1	2	0.0634	5.518	20.8882	92.54
32	8.2353	1	2	0.0543	5.918	20.852	90.66
33	12	1	2	0.05134	6.2918	20.9282	87.00
34	3	6	2	0.0919	3.2559	20.7874	99.05
35	5.12	6	2	0.095	3.4559	20.714	99.02
36	8.2353	6	2	0.06384	4.292	20.7531	98.51
37	12	6	2	0.089	4.524	20.8953	97.03
38	3	12.071	2	0.0895	3.3528	20.71	99.25

Table A-1: Continued

Sim#	Crosswind velocity (m/s)	Model parameter alpha (α)	Sc_t	CO_2 Vol %	CH_4 (E-4) Vol %	O_2 Vol %	Combustion efficiency
39	8.2353	12.071	2	0.079	3.4808	20.7431	98.81
40	12	12.071	2	0.089	4.2524	20.8853	97.63

Table A-2: Helium-Plume Results

Height above inlet (m)	Radial location (m)	Favre-averaged vertical velocity (m/s)														
		case1	case2	case3	case4	case5	case6	case7	case8	case9	case10	case11	case12	case13	case14	case15
0.2	-0.2940	0.5144	0.7780	0.4118	0.6310	0.4766	0.6649	0.5014	0.5927	0.3898	0.6467	0.5091	0.5193	0.4585	0.5998	0.4082
0.2	-0.2850	0.5753	0.8266	0.4368	0.6714	0.5176	0.7138	0.5405	0.6577	0.4502	0.7010	0.5587	0.5714	0.5329	0.6698	0.4813
0.2	-0.2760	0.6655	0.8779	0.4561	0.7224	0.5594	0.7577	0.6187	0.7150	0.5260	0.7503	0.6240	0.6063	0.6177	0.7168	0.5725
0.2	-0.2670	0.7543	0.9338	0.4942	0.7975	0.6314	0.8146	0.6942	0.7664	0.5932	0.8002	0.7135	0.6700	0.6910	0.7381	0.6685
0.2	-0.2570	0.8297	0.9970	0.5756	0.9024	0.7554	0.8964	0.7552	0.8226	0.6509	0.8653	0.8283	0.7821	0.7506	0.7511	0.7722
0.2	-0.2480	0.8785	1.0437	0.6823	0.9805	0.8780	0.9653	0.8141	0.8834	0.7112	0.9428	0.9042	0.8628	0.8014	0.7994	0.8643
0.2	-0.2390	0.9140	1.0772	0.8068	1.0232	0.9885	1.0159	0.8911	0.9602	0.7910	1.0392	0.9377	0.8955	0.8579	0.8981	0.9593
0.2	-0.2300	0.9430	1.1113	0.9123	1.0459	1.0808	1.0523	0.9737	1.0498	0.8732	1.1365	0.9659	0.9162	0.9081	0.9979	1.0653
0.2	-0.2210	0.9698	1.1571	0.9692	1.0678	1.1537	1.0811	1.0472	1.1460	0.9414	1.2181	1.0220	0.9588	0.9445	1.0565	1.1857
0.2	-0.2110	0.9883	1.2120	0.9896	1.1109	1.2266	1.1147	1.1053	1.2412	1.0017	1.2877	1.1033	1.0234	0.9956	1.0946	1.3151
0.2	-0.2020	0.9870	1.2544	0.9936	1.1769	1.2972	1.1541	1.1293	1.3017	1.0471	1.3337	1.1721	1.0805	1.0762	1.1348	1.4065
0.2	-0.1930	0.9804	1.2984	1.0112	1.2416	1.3617	1.1972	1.1409	1.3520	1.0883	1.3702	1.2310	1.1294	1.1753	1.1794	1.4743
0.2	-0.1840	0.9849	1.3557	1.0674	1.2688	1.4020	1.2357	1.1597	1.4135	1.1288	1.4045	1.2798	1.1675	1.2661	1.2170	1.5259
0.2	-0.1750	0.9914	1.4059	1.1574	1.2702	1.4135	1.2740	1.1836	1.4827	1.1698	1.4385	1.3223	1.2016	1.3348	1.2446	1.5619
0.2	-0.1650	0.9723	1.4060	1.2678	1.2914	1.3976	1.3311	1.1978	1.5450	1.2153	1.4743	1.3684	1.2497	1.3789	1.2659	1.5794
0.2	-0.1560	0.9379	1.3604	1.3573	1.3420	1.3793	1.3976	1.1964	1.5823	1.2565	1.5069	1.4042	1.3043	1.3932	1.2801	1.5736

Table A-2: Continued

Height above inlet (m)	Radial location (m)	Favre-averaged vertical velocity (m/s)														
		case1	case2	case3	case4	case5	case6	case7	case8	case9	case10	case11	case12	case13	case14	case15
0.2	-0.1470	0.9239	1.3204	1.4258	1.4055	1.3932	1.4696	1.1925	1.6109	1.2990	1.5452	1.4204	1.3605	1.3955	1.2939	1.5483
0.2	-0.1380	0.9364	1.3051	1.4704	1.4659	1.4470	1.5377	1.1953	1.6348	1.3463	1.5868	1.4184	1.4141	1.4006	1.3105	1.5129
0.2	-0.1290	0.9335	1.2881	1.5009	1.5105	1.5053	1.5914	1.2123	1.6501	1.4062	1.6168	1.4239	1.4689	1.4277	1.3317	1.4893
0.2	-0.1190	0.8879	1.2411	1.5304	1.5366	1.5443	1.6282	1.2523	1.6586	1.4883	1.6284	1.4612	1.5315	1.4888	1.3640	1.4955
0.2	-0.1100	0.8610	1.1768	1.5619	1.5592	1.5671	1.6503	1.3027	1.6778	1.5557	1.6367	1.5156	1.5775	1.5327	1.4069	1.5253
0.2	-0.1010	0.8926	1.1003	1.6036	1.5990	1.5933	1.6738	1.3607	1.7241	1.6028	1.6576	1.5778	1.6046	1.5391	1.4673	1.5685
0.2	-0.0919	0.9627	1.0253	1.6518	1.6545	1.6322	1.7125	1.4199	1.7946	1.6499	1.6820	1.6321	1.6208	1.5494	1.5440	1.6101
0.2	-0.0827	1.0378	0.9653	1.6994	1.7185	1.6902	1.7781	1.4743	1.8792	1.7219	1.6960	1.6640	1.6374	1.6138	1.6316	1.6357
0.2	-0.0735	1.1122	0.9075	1.7380	1.7835	1.7605	1.8586	1.5309	1.9506	1.8081	1.7007	1.6847	1.6589	1.7030	1.7125	1.6541
0.2	-0.0643	1.1939	0.8286	1.7601	1.8433	1.8309	1.9324	1.6018	1.9777	1.8833	1.7039	1.7163	1.6862	1.7547	1.7668	1.6846
0.2	-0.0551	1.2723	0.7408	1.7710	1.8999	1.8895	1.9918	1.6794	1.9630	1.9389	1.7109	1.7456	1.7165	1.7649	1.8053	1.7244
0.2	-0.0460	1.3240	0.6824	1.7842	1.9599	1.9243	2.0388	1.7407	1.9331	1.9777	1.7244	1.7358	1.7441	1.7708	1.8600	1.7547
0.2	-0.0368	1.3525	0.6674	1.8037	2.0133	1.9361	2.0724	1.7801	1.8979	2.0022	1.7394	1.6934	1.7679	1.7866	1.9327	1.7730
0.2	-0.0276	1.3889	0.6854	1.8202	2.0262	1.9372	2.0848	1.8078	1.8489	2.0116	1.7409	1.6766	1.7902	1.7983	1.9863	1.7931
0.2	-0.0184	1.4488	0.7241	1.8296	1.9907	1.9369	2.0732	1.8311	1.7934	2.0093	1.7247	1.7102	1.8119	1.7989	2.0014	1.8221
0.2	-0.0092	1.5129	0.7716	1.8371	1.9490	1.9362	2.0449	1.8483	1.7704	2.0061	1.7079	1.7489	1.8306	1.7972	1.9960	1.8521
0.2	0.0000	1.5604	0.8178	1.8454	1.9355	1.9329	2.0062	1.8564	1.7984	2.0113	1.7068	1.7567	1.8443	1.7989	1.9878	1.8733
0.2	0.0092	1.5782	0.8581	1.8459	1.9425	1.9178	1.9582	1.8520	1.8203	2.0260	1.7269	1.7490	1.8542	1.7938	1.9807	1.8773
0.2	0.0184	1.5591	0.8896	1.8314	1.9551	1.8832	1.9022	1.8329	1.7820	2.0478	1.7679	1.7479	1.8606	1.7732	1.9739	1.8579
0.2	0.0276	1.5227	0.9104	1.8164	1.9620	1.8376	1.8483	1.8049	1.7192	2.0599	1.8080	1.7572	1.8584	1.7508	1.9563	1.8201
0.2	0.0368	1.4931	0.9201	1.8179	1.9533	1.7940	1.8067	1.7760	1.6903	2.0447	1.8211	1.7740	1.8416	1.7449	1.9158	1.7731
0.2	0.0460	1.4609	0.9253	1.8148	1.9232	1.7611	1.7633	1.7538	1.6937	2.0121	1.8084	1.7916	1.8127	1.7486	1.8620	1.7339
0.2	0.0551	1.4011	0.9359	1.7693	1.8699	1.7449	1.6941	1.7450	1.6975	1.9861	1.7849	1.8015	1.7792	1.7430	1.8154	1.7218
0.2	0.0643	1.3139	0.9492	1.6939	1.8128	1.7419	1.6032	1.7484	1.6840	1.9724	1.7598	1.8052	1.7498	1.7193	1.7745	1.7353
0.2	0.0735	1.2247	0.9522	1.6459	1.7913	1.7418	1.5223	1.7567	1.6481	1.9631	1.7386	1.8119	1.7363	1.6783	1.7217	1.7554

Table A-2: Continued

Height above inlet (m)	Radial location (m)	Favre-averaged vertical velocity (m/s)														
		case1	case2	case3	case4	case5	case6	case7	case8	case9	case10	case11	case12	case13	case14	case15
0.2	0.0827	1.1573	0.9535	1.6378	1.8068	1.7305	1.4716	1.7600	1.6017	1.9488	1.7186	1.8154	1.7302	1.6298	1.6521	1.7614
0.2	0.0919	1.1331	0.9921	1.6190	1.8074	1.6892	1.4545	1.7465	1.5791	1.9189	1.6870	1.7880	1.6960	1.5951	1.5786	1.7311
0.2	0.1010	1.1516	1.0746	1.5619	1.7654	1.6218	1.4625	1.7072	1.5915	1.8715	1.6421	1.7190	1.6203	1.5809	1.5122	1.6637
0.2	0.1100	1.1677	1.1369	1.4968	1.7114	1.5783	1.4648	1.6391	1.5976	1.8205	1.6055	1.6354	1.5380	1.5599	1.4534	1.6019
0.2	0.1190	1.1457	1.1328	1.4511	1.6711	1.5906	1.4390	1.5451	1.5660	1.7760	1.5938	1.5605	1.4791	1.5120	1.4033	1.5753
0.2	0.1290	1.0990	1.1114	1.4146	1.6231	1.6024	1.3990	1.4422	1.5215	1.7239	1.5963	1.4876	1.4347	1.4542	1.3703	1.5452
0.2	0.1380	1.0683	1.1406	1.3825	1.5540	1.5433	1.3783	1.3800	1.5111	1.6635	1.5952	1.4259	1.4010	1.4270	1.3702	1.4753
0.2	0.1470	1.0623	1.1800	1.3625	1.4669	1.4429	1.3685	1.3406	1.5144	1.6004	1.5908	1.3701	1.3742	1.4137	1.3799	1.3964
0.2	0.1560	1.0869	1.1661	1.3713	1.3787	1.3560	1.3565	1.3064	1.5015	1.5491	1.5879	1.3239	1.3595	1.3923	1.3735	1.3612
0.2	0.1650	1.1273	1.1125	1.3878	1.3057	1.3114	1.3379	1.2683	1.4726	1.4967	1.5819	1.2808	1.3511	1.3557	1.3442	1.3696
0.2	0.1750	1.1576	1.0809	1.3626	1.2601	1.3232	1.3105	1.2167	1.4446	1.4014	1.5585	1.2216	1.3338	1.3000	1.2911	1.3890
0.2	0.1840	1.1588	1.0932	1.3026	1.2421	1.3545	1.2799	1.1603	1.4185	1.2880	1.5140	1.1596	1.3011	1.2433	1.2341	1.3852
0.2	0.1930	1.1389	1.1094	1.2548	1.2144	1.3314	1.2428	1.0951	1.3634	1.1892	1.4428	1.1047	1.2465	1.1903	1.1797	1.3397
0.2	0.2020	1.1031	1.1089	1.2311	1.1639	1.2327	1.1963	1.0261	1.2799	1.1196	1.3520	1.0637	1.1748	1.1424	1.1335	1.2573
0.2	0.2110	1.0580	1.0942	1.1869	1.1066	1.1187	1.1345	0.9643	1.2133	1.0535	1.2665	1.0307	1.1063	1.0873	1.0921	1.1817
0.2	0.2210	1.0055	1.0638	1.0788	1.0456	1.0309	1.0508	0.9106	1.1845	0.9610	1.1933	0.9921	1.0447	1.0065	1.0453	1.1363
0.2	0.2300	0.9645	1.0198	0.9550	0.9762	0.9799	0.9881	0.8623	1.1418	0.8690	1.1239	0.9398	0.9767	0.9181	0.9927	1.0955
0.2	0.2390	0.9338	0.9593	0.8362	0.8822	0.9396	0.9546	0.8016	1.0383	0.7782	1.0331	0.8619	0.8786	0.8195	0.9238	1.0244
0.2	0.2480	0.9043	0.8988	0.7344	0.7925	0.8949	0.9195	0.7277	0.9196	0.6851	0.9443	0.7780	0.7782	0.7201	0.8466	0.9434
0.2	0.2570	0.8629	0.8562	0.6559	0.7395	0.8322	0.8469	0.6452	0.8441	0.5853	0.8859	0.7118	0.7099	0.6294	0.7719	0.8798
0.2	0.2670	0.7874	0.8206	0.5850	0.7044	0.7456	0.7381	0.5706	0.7911	0.4788	0.8434	0.6600	0.6610	0.5412	0.7015	0.8099
0.2	0.2850	0.5619	0.7273	0.4578	0.5896	0.5819	0.5810	0.5496	0.6247	0.3521	0.7303	0.5787	0.5514	0.4196	0.6067	0.5959
0.2	0.2940	0.4708	0.6684	0.4128	0.5263	0.5003	0.5156	0.5240	0.5303	0.3136	0.6526	0.5144	0.4820	0.3933	0.5266	0.5027
0.4	-0.2940	0.6341	0.7713	0.5668	0.7433	0.4753	0.7751	0.6601	0.6911	0.4053	0.8186	0.5358	0.5179	0.4681	0.5866	0.5316
0.4	-0.2850	0.6895	0.8360	0.6310	0.8140	0.5055	0.8333	0.6994	0.7635	0.4791	0.9168	0.6201	0.5757	0.5347	0.6550	0.6270

Table A-2: Continued

Height above inlet (m)	Radial location (m)	Favre-averaged vertical velocity (m/s)														
		case1	case2	case3	case4	case5	case6	case7	case8	case9	case10	case11	case12	case13	case14	case15
0.4	-0.2760	0.7435	0.8903	0.7103	0.8926	0.5296	0.8720	0.7413	0.8341	0.5488	0.9938	0.7350	0.6370	0.6365	0.7120	0.7398
0.4	-0.2670	0.8004	0.9527	0.7894	0.9571	0.5987	0.9191	0.8159	0.9115	0.6435	1.0511	0.8393	0.7054	0.7308	0.7728	0.8439
0.4	-0.2570	0.8719	1.0365	0.8701	1.0092	0.7374	0.9983	0.9458	1.0120	0.7800	1.1043	0.9218	0.7918	0.8122	0.8561	0.9454
0.4	-0.2480	0.9475	1.1072	0.9458	1.0675	0.8572	1.0861	1.0757	1.1170	0.8886	1.1680	0.9856	0.8775	0.9018	0.9456	1.0571
0.4	-0.2390	1.0292	1.1639	1.0307	1.1513	0.9363	1.1785	1.1899	1.2320	0.9637	1.2596	1.0544	0.9712	1.0250	1.0466	1.2007
0.4	-0.2300	1.0955	1.2167	1.1220	1.2429	0.9973	1.2604	1.2673	1.3439	1.0363	1.3670	1.1283	1.0782	1.1539	1.1520	1.3426
0.4	-0.2210	1.1320	1.2758	1.2163	1.3280	1.0679	1.3243	1.3022	1.4420	1.1333	1.4760	1.2076	1.1990	1.2605	1.2545	1.4541
0.4	-0.2110	1.1668	1.3504	1.3208	1.4338	1.1795	1.4054	1.3560	1.5401	1.2545	1.5860	1.3120	1.3245	1.3467	1.3575	1.5612
0.4	-0.2020	1.2214	1.4226	1.4131	1.5559	1.3218	1.5152	1.4728	1.6271	1.3547	1.6680	1.4282	1.4082	1.3986	1.4367	1.6666
0.4	-0.1930	1.2821	1.4873	1.5100	1.6747	1.4849	1.6360	1.5957	1.7221	1.4472	1.7495	1.5515	1.4819	1.4485	1.5180	1.7799
0.4	-0.1840	1.3209	1.5312	1.6192	1.7503	1.6402	1.7290	1.6374	1.8327	1.5400	1.8512	1.6619	1.5745	1.5229	1.6206	1.8925
0.4	-0.1750	1.3487	1.5654	1.7269	1.7983	1.7708	1.7957	1.6266	1.9519	1.6399	1.9688	1.7528	1.6853	1.6253	1.7393	2.0022
0.4	-0.1650	1.4089	1.6236	1.8132	1.8791	1.8767	1.8715	1.6747	2.0738	1.7655	2.0934	1.8344	1.8061	1.7583	1.8655	2.1232
0.4	-0.1560	1.4895	1.7018	1.8697	1.9914	1.9532	1.9590	1.7914	2.1643	1.8857	2.1919	1.9081	1.9050	1.8793	1.9620	2.2315
0.4	-0.1470	1.5592	1.7925	1.9493	2.1181	2.0509	2.0695	1.9100	2.2351	1.9960	2.2828	2.0116	2.0003	1.9838	2.0411	2.3374
0.4	-0.1380	1.6015	1.8767	2.0657	2.2386	2.1801	2.1953	1.9903	2.2962	2.0901	2.3687	2.1449	2.0955	2.0678	2.1109	2.4354
0.4	-0.1290	1.6302	1.9262	2.1871	2.3387	2.3070	2.3105	2.0371	2.3741	2.1772	2.4464	2.2626	2.1906	2.1481	2.1930	2.5145
0.4	-0.1190	1.6627	1.9313	2.2999	2.4226	2.4181	2.4092	2.0725	2.5000	2.2762	2.5238	2.3372	2.2948	2.2464	2.3118	2.5721
0.4	-0.1100	1.6997	1.9430	2.3920	2.5023	2.5110	2.4959	2.1382	2.6330	2.3720	2.5976	2.3708	2.3829	2.3334	2.4211	2.6033
0.4	-0.1010	1.7470	2.0006	2.4896	2.6082	2.6163	2.6004	2.2673	2.7630	2.4764	2.6832	2.3978	2.4618	2.4105	2.5114	2.6245
0.4	-0.0919	1.7986	2.0627	2.6028	2.7244	2.7279	2.7054	2.4139	2.8662	2.5892	2.7681	2.4478	2.5300	2.4856	2.5863	2.6497
0.4	-0.0827	1.8465	2.0730	2.7365	2.8274	2.8318	2.7877	2.5170	2.9213	2.7083	2.8353	2.5468	2.5870	2.5689	2.6550	2.6923
0.4	-0.0735	1.8949	2.0352	2.8654	2.9266	2.9119	2.8634	2.5750	2.9620	2.8317	2.8895	2.6746	2.6459	2.6625	2.7302	2.7493
0.4	-0.0643	1.9540	1.9825	2.9551	3.0455	2.9552	2.9662	2.6162	3.0439	2.9591	2.9456	2.7921	2.7251	2.7645	2.8253	2.8106
0.4	-0.0551	2.0299	1.9509	3.0085	3.1610	2.9713	3.0885	2.6635	3.1552	3.0843	3.0050	2.8892	2.8171	2.8531	2.9287	2.8759

Table A-2: Continued

Height above inlet (m)	Radial location (m)	Favre-averaged vertical velocity (m/s)														
		case1	case2	case3	case4	case5	case6	case7	case8	case9	case10	case11	case12	case13	case14	case15
0.4	-0.0460	2.1247	1.9762	3.0543	3.2175	2.9859	3.1927	2.7341	3.2357	3.1960	3.0581	2.9756	2.8954	2.8923	3.0101	2.9499
0.4	-0.0368	2.2405	2.0530	3.0974	3.2063	3.0065	3.2674	2.8369	3.2649	3.2917	3.0995	3.0530	2.9588	2.8840	3.0656	3.0249
0.4	0.0460	2.5630	2.1652	2.7937	3.0108	2.9308	2.9076	3.0462	2.9367	3.2303	3.0079	2.9796	3.1438	2.7429	3.0227	3.0078
0.4	0.0551	2.4497	2.1867	2.7207	2.9453	2.8566	2.7972	3.0212	2.8500	3.1659	2.9761	2.9470	3.0868	2.7386	2.9402	2.9110
0.4	0.0643	2.3501	2.2251	2.6190	2.8772	2.8017	2.6841	3.0023	2.7777	3.0782	2.9451	2.9140	3.0131	2.7234	2.8524	2.8014
0.4	0.0735	2.2604	2.1828	2.5262	2.8109	2.7580	2.5657	2.9446	2.7082	2.9755	2.8944	2.8472	2.9250	2.6945	2.7637	2.6915
0.4	0.0827	2.1756	2.0462	2.4529	2.7442	2.7105	2.4449	2.8360	2.6425	2.8704	2.8205	2.7371	2.8310	2.6482	2.6766	2.5914
0.4	0.0919	2.0921	1.9200	2.3715	2.6668	2.6371	2.3341	2.7113	2.6015	2.7823	2.7445	2.6089	2.7492	2.5799	2.5922	2.5091
0.4	0.0643	2.3501	2.2251	2.6190	2.8772	2.8017	2.6841	3.0023	2.7777	3.0782	2.9451	2.9140	3.0131	2.7234	2.8524	2.8014
0.4	0.0735	2.2604	2.1828	2.5262	2.8109	2.7580	2.5657	2.9446	2.7082	2.9755	2.8944	2.8472	2.9250	2.6945	2.7637	2.6915
0.4	0.1010	2.0113	1.8672	2.2719	2.5761	2.5336	2.2425	2.5976	2.5907	2.7173	2.6775	2.4848	2.6854	2.4929	2.5113	2.4448
0.4	0.1100	1.9430	1.8401	2.1828	2.4848	2.4312	2.1676	2.4930	2.5792	2.6497	2.6035	2.3699	2.6164	2.4043	2.4324	2.3794
0.4	0.1190	1.8945	1.7914	2.1251	2.4028	2.3541	2.1063	2.3898	2.5368	2.5569	2.5109	2.2647	2.5221	2.3249	2.3535	2.2983
0.4	0.1290	1.8612	1.7161	2.0701	2.3228	2.2865	2.0581	2.2630	2.4390	2.4297	2.4124	2.1539	2.3984	2.2291	2.2688	2.2060
0.4	0.1380	1.8432	1.6449	1.9979	2.2560	2.2228	2.0337	2.1284	2.3037	2.3039	2.3528	2.0534	2.2837	2.1179	2.1970	2.1387
0.4	0.1470	1.8212	1.5796	1.9071	2.1783	2.1440	2.0050	1.9885	2.1612	2.1682	2.3043	1.9461	2.1612	1.9967	2.1198	2.0791
0.4	0.1560	1.7786	1.5262	1.8116	2.0728	2.0419	1.9447	1.8638	2.0584	2.0210	2.2383	1.8274	2.0211	1.8879	2.0259	2.0122
0.4	0.1650	1.7130	1.4846	1.7130	1.9527	1.9322	1.8576	1.7566	1.9894	1.8741	2.1512	1.7086	1.8764	1.7925	1.9249	1.9345
0.4	0.1750	1.6216	1.4467	1.5935	1.8394	1.8368	1.7598	1.6462	1.9052	1.7350	2.0443	1.6014	1.7422	1.6871	1.8312	1.8397
0.4	0.1840	1.5251	1.4107	1.4819	1.7546	1.7708	1.6821	1.5432	1.8083	1.6326	1.9477	1.5318	1.6480	1.5921	1.7636	1.7464
0.4	0.1930	1.4126	1.3599	1.3813	1.6517	1.6857	1.6099	1.4256	1.7044	1.5339	1.8540	1.4742	1.5566	1.5088	1.6888	1.6417
0.4	0.2020	1.2858	1.2961	1.3015	1.5239	1.5648	1.5385	1.2990	1.5971	1.4261	1.7611	1.4131	1.4589	1.4416	1.5955	1.5242
0.4	0.2110	1.1529	1.2429	1.2442	1.4069	1.4247	1.4638	1.1948	1.4742	1.3053	1.6592	1.3299	1.3662	1.3825	1.4908	1.3972
0.4	0.2210	1.0140	1.2117	1.1981	1.3168	1.2730	1.3708	1.1241	1.3157	1.1590	1.5289	1.2056	1.2736	1.3124	1.3661	1.2514
0.4	0.2300	0.9228	1.1861	1.1409	1.2485	1.1709	1.2700	1.0669	1.1802	1.0355	1.4044	1.1001	1.1761	1.2255	1.2381	1.1263

Table A-2: Continued

Height above inlet (m)	Radial location (m)	Favre-averaged vertical velocity (m/s)														
		case1	case2	case3	case4	case5	case6	case7	case8	case9	case10	case11	case12	case13	case14	case15
0.4	0.2390	0.8774	1.1414	1.0480	1.1683	1.1154	1.1519	0.9819	1.0736	0.9342	1.2820	1.0282	1.0507	1.1052	1.0946	1.0140
0.4	0.2480	0.8392	1.0805	0.9489	1.0757	1.0552	1.0434	0.8632	0.9859	0.8458	1.1652	0.9694	0.9310	0.9798	0.9724	0.9084
0.4	0.2570	0.7653	1.0132	0.8789	0.9756	0.9346	0.9722	0.7164	0.8999	0.7562	1.0568	0.8946	0.8549	0.8822	0.9087	0.8024
0.4	0.2670	0.6710	0.9514	0.8112	0.8641	0.7751	0.9126	0.5744	0.7924	0.6527	0.9535	0.7912	0.7945	0.7976	0.8622	0.6979
0.4	0.2760	0.6301	0.9266	0.7157	0.7713	0.6879	0.8344	0.5265	0.6767	0.5595	0.8822	0.6923	0.7118	0.7174	0.7720	0.6357
0.4	0.2850	0.6199	0.9132	0.6047	0.6877	0.6380	0.7388	0.5259	0.5558	0.4690	0.8156	0.5986	0.6002	0.6346	0.6398	0.5988
0.4	0.2940	0.5887	0.8714	0.5328	0.6118	0.5499	0.6612	0.4898	0.4555	0.3830	0.7246	0.5194	0.4882	0.5669	0.5159	0.5661
0.6	-0.2940	0.8907	0.9233	0.6752	0.7166	0.4584	0.8240	0.7292	0.7751	0.4961	0.8400	0.6351	0.6486	0.6160	0.5637	0.5413
0.6	-0.2850	0.9536	0.9451	0.7380	0.8027	0.4764	0.9279	0.8056	0.8760	0.6197	0.9100	0.6555	0.7091	0.6637	0.6487	0.6262
0.6	-0.2760	1.0013	0.9883	0.8150	0.8870	0.5417	1.0216	0.9063	0.9743	0.7509	1.0111	0.6873	0.7468	0.7002	0.7434	0.7236
0.6	-0.2670	1.0518	1.0365	0.8954	0.9768	0.6301	1.0975	0.9995	1.0733	0.8576	1.1094	0.7832	0.8158	0.7627	0.8358	0.8392
0.6	-0.2570	1.1184	1.0854	0.9871	1.0850	0.7379	1.1655	1.0818	1.1803	0.9360	1.1997	0.9670	0.9456	0.8762	0.9347	0.9928
0.6	-0.2480	1.1747	1.1288	1.0857	1.1819	0.8453	1.2335	1.1612	1.2609	0.9968	1.2848	1.1225	1.0594	0.9883	1.0370	1.1532
0.6	-0.2390	1.2214	1.1762	1.2048	1.2753	0.9636	1.3172	1.2595	1.3254	1.0688	1.3923	1.2235	1.1414	1.0896	1.1549	1.3249
0.6	-0.2300	1.2699	1.2321	1.3301	1.3738	1.0906	1.3985	1.3644	1.3971	1.1566	1.5320	1.3031	1.2164	1.1846	1.2606	1.4789
0.6	-0.2210	1.3288	1.2992	1.4494	1.4832	1.2235	1.4645	1.4632	1.4944	1.2608	1.7034	1.3951	1.3083	1.2793	1.3349	1.5938
0.6	-0.2110	1.3946	1.3795	1.5840	1.6033	1.3762	1.5454	1.5639	1.6138	1.3880	1.8849	1.5080	1.4232	1.3860	1.4184	1.6996
0.6	-0.2020	1.4415	1.4512	1.7146	1.6972	1.5151	1.6492	1.6467	1.7126	1.5049	1.9999	1.6081	1.5270	1.4836	1.5343	1.8049
0.6	-0.1930	1.4819	1.5352	1.8308	1.7893	1.6449	1.7625	1.7176	1.8226	1.6226	2.0923	1.7090	1.6372	1.5841	1.6848	1.9336
0.6	-0.1840	1.5271	1.6473	1.9033	1.8982	1.7548	1.8536	1.7731	1.9723	1.7424	2.2041	1.8163	1.7643	1.6894	1.8500	2.0916
0.6	-0.1750	1.5845	1.7662	1.9564	2.0258	1.8628	1.9295	1.8390	2.1400	1.8669	2.3329	1.9257	1.8984	1.8016	2.0052	2.2588
0.6	-0.1650	1.6680	1.8540	2.0615	2.1785	2.0229	2.0342	1.9757	2.2842	2.0144	2.4602	2.0371	2.0289	1.9371	2.1337	2.4132
0.6	-0.1560	1.7503	1.8952	2.2043	2.3216	2.1980	2.1570	2.1454	2.3687	2.1507	2.5548	2.1349	2.1324	2.0651	2.2161	2.5222
0.6	-0.1470	1.8159	1.9492	2.3468	2.4712	2.3573	2.2937	2.2962	2.4503	2.2782	2.6510	2.2531	2.2501	2.1894	2.3062	2.6359
0.6	-0.1380	1.8639	2.0374	2.4599	2.6197	2.4852	2.4323	2.3997	2.5468	2.3934	2.7560	2.3977	2.3888	2.3082	2.4201	2.7650

Table A-2: Continued

Height above inlet (m)	Radial location (m)	Favre-averaged vertical velocity (m/s)														
		case1	case2	case3	case4	case5	case6	case7	case8	case9	case10	case11	case12	case13	case14	case15
0.6	-0.1290	1.9281	2.1388	2.5422	2.7459	2.6119	2.5639	2.4817	2.6397	2.5064	2.8556	2.5477	2.5238	2.4302	2.5389	2.8842
0.6	-0.1190	2.0394	2.2455	2.6104	2.8466	2.7704	2.7021	2.5704	2.7268	2.6368	2.9521	2.6954	2.6456	2.5754	2.6593	2.9873
0.6	-0.1100	2.1380	2.3377	2.6897	2.9215	2.8932	2.8452	2.6357	2.8117	2.7504	3.0463	2.7945	2.7319	2.7044	2.7632	3.0755
0.6	-0.1010	2.2030	2.4275	2.8145	3.0024	2.9716	3.0201	2.6774	2.9188	2.8528	3.1612	2.8575	2.8039	2.8221	2.8684	3.1774
0.6	-0.0919	2.2542	2.5036	2.9620	3.0980	3.0496	3.1848	2.7165	3.0262	2.9458	3.2740	2.9245	2.8802	2.9293	2.9676	3.2757
0.6	-0.0827	2.3209	2.5529	3.0973	3.2113	3.1792	3.2881	2.7794	3.1061	3.0335	3.3554	3.0391	2.9781	3.0275	3.0515	3.3460
0.6	-0.0735	2.4077	2.5871	3.2071	3.3277	3.3309	3.3496	2.8709	3.1748	3.1309	3.4196	3.1766	3.0827	3.1136	3.1336	3.3944
0.6	-0.0643	2.5079	2.6291	3.2915	3.4270	3.4428	3.4213	2.9856	3.2675	3.2575	3.4997	3.2852	3.1683	3.1840	3.2372	3.4415
0.6	-0.0551	2.6106	2.6833	3.3596	3.5033	3.5069	3.5148	3.1113	3.3802	3.4030	3.5923	3.3608	3.2459	3.2368	3.3491	3.4883
0.6	-0.0460	2.7014	2.7395	3.4256	3.5603	3.5541	3.6112	3.2298	3.4796	3.5347	3.6670	3.4330	3.3509	3.2706	3.4295	3.5222
0.6	-0.0368	2.7887	2.7967	3.4892	3.6024	3.6006	3.6931	3.3405	3.5513	3.6423	3.7135	3.5144	3.4855	3.2906	3.4703	3.5418
0.6	-0.0276	2.9010	2.8604	3.5278	3.6307	3.6407	3.7382	3.4544	3.5967	3.7323	3.7400	3.5914	3.6056	3.3074	3.4953	3.5570
0.6	-0.0184	3.0472	2.9307	3.5305	3.6545	3.6708	3.7364	3.5655	3.6197	3.8094	3.7539	3.6515	3.6869	3.3251	3.5196	3.5724
0.6	-0.0092	3.1948	2.9946	3.5092	3.6982	3.6917	3.6974	3.6307	3.6247	3.8692	3.7560	3.6857	3.7465	3.3339	3.5365	3.5815
0.6	0.0000	3.3081	3.0353	3.4753	3.7694	3.7019	3.6313	3.6258	3.6168	3.9048	3.7481	3.6906	3.7980	3.3245	3.5412	3.5773
0.6	0.0092	3.3599	3.0286	3.4308	3.8207	3.6915	3.5411	3.5974	3.6038	3.9059	3.7359	3.6812	3.8333	3.2931	3.5419	3.5569
0.6	0.0184	3.3335	2.9565	3.3758	3.8056	3.6527	3.4300	3.5933	3.5916	3.8674	3.7242	3.6710	3.8415	3.2424	3.5460	3.5199
0.6	0.0276	3.2622	2.8432	3.3105	3.7394	3.5983	3.3099	3.5982	3.5730	3.8161	3.7076	3.6489	3.8217	3.2042	3.5429	3.4762
0.6	0.0368	3.1908	2.7252	3.2349	3.6551	3.5451	3.1944	3.5800	3.5383	3.7838	3.6776	3.5977	3.7770	3.2123	3.5169	3.4358
0.6	0.0460	3.1169	2.6275	3.1434	3.5628	3.4899	3.0923	3.5396	3.4916	3.7588	3.6268	3.5209	3.7139	3.2362	3.4623	3.3808
0.6	0.0551	3.0171	2.5678	3.0307	3.4619	3.4201	3.0101	3.4948	3.4448	3.7078	3.5504	3.4329	3.6418	3.2155	3.3798	3.2826
0.6	0.0643	2.9009	2.5284	2.9095	3.3507	3.3286	2.9406	3.4408	3.3982	3.6187	3.4528	3.3391	3.5657	3.1418	3.2788	3.1490
0.6	0.0735	2.8116	2.4657	2.8145	3.2333	3.2176	2.8705	3.3572	3.3449	3.5009	3.3513	3.2419	3.4912	3.0523	3.1813	3.0254
0.6	0.0827	2.7499	2.3760	2.7470	3.1221	3.0999	2.7914	3.2370	3.2696	3.3666	3.2522	3.1429	3.4127	2.9636	3.0959	2.9310
0.6	0.0919	2.6577	2.3117	2.6632	3.0424	3.0037	2.7040	3.0939	3.1458	3.2322	3.1477	3.0437	3.3098	2.8617	3.0143	2.8492

Table A-2: Continued

Height above inlet (m)	Radial location (m)	Favre-averaged vertical velocity (m/s)														
		case1	case2	case3	case4	case5	case6	case7	case8	case9	case10	case11	case12	case13	case14	case15
0.6	0.1010	2.5122	2.2947	2.5457	2.9982	2.9355	2.6141	2.9422	2.9761	3.1075	3.0365	2.9414	3.1784	2.7430	2.9310	2.7695
0.6	0.1100	2.3703	2.2706	2.4371	2.9434	2.8515	2.5343	2.7894	2.8202	2.9844	2.9295	2.8210	3.0469	2.6275	2.8474	2.6976
0.6	0.1190	2.2784	2.1947	2.3682	2.8402	2.7197	2.4720	2.6427	2.7217	2.8532	2.8358	2.6722	2.9357	2.5292	2.7617	2.6341
0.6	0.1290	2.2092	2.0795	2.2964	2.6887	2.5654	2.4092	2.5076	2.6380	2.6952	2.7506	2.4988	2.8160	2.4255	2.6476	2.5452
0.6	0.1380	2.1395	1.9867	2.1915	2.5472	2.4695	2.3432	2.4249	2.5378	2.5416	2.6886	2.3614	2.6870	2.3205	2.5151	2.4251
0.6	0.1470	2.0512	1.9040	2.0658	2.4076	2.3910	2.2660	2.3487	2.4274	2.3813	2.6214	2.2398	2.5333	2.2099	2.3701	2.2907
0.6	0.1560	1.9431	1.8194	1.9562	2.2692	2.2853	2.1806	2.2371	2.3384	2.2197	2.5257	2.1233	2.3590	2.1066	2.2369	2.1785
0.6	0.1650	1.8297	1.7374	1.8681	2.1378	2.1562	2.0931	2.0902	2.2674	2.0655	2.4011	2.0073	2.1851	2.0176	2.1183	2.0808
0.6	0.1750	1.7256	1.6667	1.7789	2.0113	2.0261	2.0028	1.9176	2.1780	1.9154	2.2462	1.8781	2.0289	1.9382	1.9904	1.9471
0.6	0.1840	1.6469	1.6119	1.6998	1.9180	1.9214	1.9253	1.7675	2.0705	1.7976	2.1101	1.7626	1.9184	1.8771	1.8703	1.8086
0.6	0.1930	1.5499	1.5333	1.6238	1.8399	1.7947	1.8388	1.6209	1.9309	1.6822	1.9956	1.6500	1.7995	1.8101	1.7410	1.6962
0.6	0.2020	1.4255	1.4271	1.5506	1.7651	1.6380	1.7387	1.4827	1.7680	1.5584	1.9032	1.5449	1.6597	1.7279	1.6079	1.6188
0.6	0.2110	1.3012	1.3343	1.4750	1.6712	1.4834	1.6323	1.3689	1.6129	1.4201	1.8057	1.4557	1.5247	1.6312	1.4913	1.5308
0.6	0.2210	1.1905	1.2810	1.3851	1.5322	1.3426	1.5203	1.2719	1.4730	1.2524	1.6686	1.3745	1.3996	1.5118	1.3966	1.3864
0.6	0.2300	1.1160	1.2624	1.3031	1.4032	1.2346	1.4452	1.1671	1.3588	1.1134	1.5297	1.2912	1.2892	1.4044	1.3315	1.2467
0.6	0.2390	1.0605	1.2508	1.2247	1.2949	1.1314	1.4044	1.0152	1.2382	1.0047	1.3890	1.1799	1.1650	1.3047	1.2702	1.1301
0.6	0.2480	1.0111	1.2319	1.1499	1.2008	1.0273	1.3675	0.8611	1.1146	0.9128	1.2527	1.0657	1.0461	1.2055	1.1954	1.0354
0.6	0.2570	0.9554	1.1949	1.0770	1.1084	0.9192	1.2981	0.7596	0.9962	0.8182	1.1255	0.9786	0.9566	1.0971	1.0924	0.9533
0.6	0.2670	0.8947	1.1410	0.9871	1.0049	0.8033	1.1804	0.6913	0.8748	0.7056	0.9994	0.8951	0.8834	0.9690	0.9584	0.8640
0.6	0.2760	0.8571	1.0967	0.8864	0.9137	0.7150	1.0531	0.6223	0.7760	0.6012	0.9020	0.7968	0.8184	0.8556	0.8443	0.7744
0.6	0.2850	0.8319	1.0582	0.7799	0.8264	0.6429	0.9293	0.5335	0.6857	0.5034	0.8042	0.6884	0.7343	0.7542	0.7498	0.6851
0.6	0.2940	0.8029	1.0191	0.6954	0.7446	0.5806	0.8368	0.4343	0.6006	0.4242	0.6807	0.6103	0.6146	0.6752	0.6814	0.6172

APPENDIX B

GOVERNING EQUATIONS

B.1. Mathematic Formulation

The LES solver used for simulations solves the full system of Navier-Stokes equations on the grid points. It uses a segregated flow solver which solves the flow equations (one for each component of velocity, and one for pressure) in a segregated, or uncoupled, manner. The linkage between the momentum and continuity equations is achieved with a predictor-corrector approach. A Rhie and Chow type pressure-velocity coupling combined with a SIMPLE-type algorithm [53] is implemented in this solver.

The basic steps in the solution update are as follows:

1. Set the boundary conditions.
2. Compute the reconstruction gradients of velocity and pressure.
3. Compute the velocity and pressure gradients.
4. Solve the discretized momentum equation to create the intermediate velocity filed v^*.
5. Compute the uncorrected mass fluxes at faces m_f^*.
6. Solve the pressure correction equation to produce cell values of the pressure correction p`
7. Update the pressure field:

$$p^{n+1} = p^n + \omega p` \qquad (B.1)$$

where ω is the under relaxation factor for pressure.

8. Update the boundary pressure correction $p`_b$.
9. Correct the face mass fluxes:

$$m_f^{n+1} = m_f^* + m_f^` \tag{B.2}$$

10. Correct the cell velocities:

$$v^{n+1} = v^* - \frac{V\nabla p^`}{a_p^v} \tag{B.3}$$

where $\nabla p^`$ is the gradient of the pressure corrections, a_p^v is the vector of central coefficients for the discretized linear system representing the velocity equation, and V is the cell volume.

11. Update density due to pressure changes.
12. Free all temporary storage.

Also used is segregated fluid enthalpy model which solves the total energy equation with chemical thermal enthalpy as the independent variable. Temperature is then computed from enthalpy using the equation of state. The general equations for continuity, momentum, and energy are given by following equations:

$$\frac{\partial \rho}{\partial t} + \frac{\partial(\rho u_i)}{\partial x_i} = 0 \tag{B.4}$$

$$\frac{\partial(\rho u_i)}{\partial t} + \frac{\partial(\rho u_i u_j)}{\partial x_j} = -\frac{\partial p}{\partial x_i} + \frac{\partial \sigma_{ij}}{\partial x_j} - \rho g_i \tag{B.5}$$

$$\frac{\partial(\rho E)}{\partial t} + \frac{\partial((\rho E + p)u_j)}{\partial x_j} = -\frac{\partial q_j}{\partial x_j} + \frac{\partial(\sigma_{ij} u_i)}{\partial x_j} \tag{B.6}$$

where,

$$\sigma_{ij} = \mu\left(\frac{\partial u_i}{\partial x_j} + \frac{\partial u_j}{\partial x_i} - \frac{2}{3}\frac{\partial u_k}{\partial x_k}\delta_{ij}\right) \tag{B.7}$$

$$q_j = -k\frac{\partial T}{\partial x_j} \tag{B.8}$$

where k = thermal conductivity, E= total energy, which can be expressed in terms of internal energy e, and kinetic energy.

$$E = e + \frac{1}{2}\,u_i u_i \tag{B.9}$$

Scalar transport can be represented as below:

$$\frac{\partial(\rho\emptyset)}{\partial t} + \frac{\partial(\rho\emptyset u_j)}{\partial x_j} = \frac{\partial}{\partial x_j}\left(\rho D_\emptyset \frac{\partial\emptyset}{\partial x_j}\right) \tag{B.10}$$

The governing equation for LES was obtained by using spatial filtering of the equations B.4-B.9. This process effectively filters out eddies whose scales are smaller than the filter width or grid spacing used in the computations. The filtering operator used is:

$$\overline{\emptyset}(x) = \int_D \emptyset(x')G(x,x')dx' \tag{B.11}$$

where D represents the computational domain and G(x, x') represents the operational filter, $\overline{\emptyset}(x)$ can be thought of as the large scale or resolved variable. The filter G is expressed for the current study as

$$G(x,x') = \begin{cases} 1/V & x' \in v \\ 0 & otherwise \end{cases} \tag{B.12}$$

where V represents the volume of the computational cell, *v* is the volume of domain, and G must satisfy the following relation:

$$\int_{-\infty}^{\infty} G(x,x')dx' = 1 \tag{B.13}$$

The filtering operator simplifies to

$$\overline{\emptyset}(x) = \frac{1}{V}\int_D \emptyset(x')dx' \tag{B.14}$$

The finite volume discretization used turns this filter into implicit uniform filter which when applied to the governing equations is similar to taking ensemble average. This uniform filter transforms the original equations (B.4-B.10) to equations (B.15-B.20)

$$\frac{\partial \overline{\rho}}{\partial t} + \frac{\partial (\overline{\rho u_i})}{\partial x_i} = 0 \qquad (B.15)$$

$$\frac{\partial (\overline{\rho u_i})}{\partial t} + \frac{\partial (\overline{\rho u_i u_j})}{\partial x_j} = -\frac{\partial \overline{p}}{\partial x_i} + \frac{\partial \overline{\sigma_{ij}}}{\partial x_j} - \overline{\rho g_i} \qquad (B.16)$$

$$\frac{\partial (\overline{\rho E})}{\partial t} + \frac{\partial (\overline{(\rho E + p) u_j})}{\partial x_j} = -\frac{\partial \overline{q_j}}{\partial x_j} + \frac{\partial \left(\overline{\sigma_{ij} u_i}\right)}{\partial x_j} \qquad (B.17)$$

$$\overline{\sigma_{ij}} = \overline{\mu \left(\frac{\partial u_i}{\partial x_j} + \frac{\partial u_j}{\partial x_i} - \frac{2}{3} \frac{\partial u_k}{\partial x_k} \delta_{ij} \right)} \qquad (B.18)$$

$$\overline{q_j} = -k \overline{\frac{\partial T}{\partial x_j}} \qquad (B.19)$$

$$\frac{\partial (\overline{\rho \emptyset})}{\partial t} + \frac{\partial (\overline{\rho \emptyset u_j})}{\partial x_j} = \frac{\partial}{\partial x_j} \left(\overline{\rho D_\emptyset \frac{\partial \emptyset}{\partial x_j}} \right) \qquad (B.20)$$

Using commutative properties of filtering (and averaging) the above equations can be simplified. Gravity term, molecular viscosity, heat conduction coefficient, and diffusion constant in the above equations are either constant or fluid properties and thus are not a function of time or space. These equations are simpler if variables are recast in terms of favre-filtered quantities. A favre-filtered variable is defined as

$$\tilde{f} = \frac{\overline{\rho f}}{\bar{\rho}} \qquad (B.21)$$

Therefore, equations B.15 to B.20 can be written as below:

$$\frac{\partial \overline{\rho}}{\partial t} + \frac{\partial (\overline{\rho}\, \widetilde{u_i})}{\partial x_i} = 0 \tag{B.22}$$

$$\frac{\partial (\overline{\rho}\, \widetilde{u_i}\,)}{\partial t} + \frac{\partial (\overline{\rho}\, \widetilde{u_i u_j})}{\partial x_j} = -\frac{\partial \overline{p}}{\partial x_i} + \frac{\partial \widetilde{\sigma_{ij}}}{\partial x_j} - \overline{\rho}\, g_i \tag{B.23}$$

Equation B.23 can be rewritten as (filtered momentum equation)

$$\frac{\partial (\overline{\rho}\, \widetilde{u_i}\,)}{\partial t} + \frac{\partial (\overline{\rho}\, \widetilde{u_i}\widetilde{u_j})}{\partial x_j} = -\frac{\partial \overline{p}}{\partial x_i} + \frac{\partial \widetilde{\sigma_{ij}}}{\partial x_j} - \frac{\partial \tau_{ij}^{SGS}}{\partial x_j} - \overline{\rho}\, g_i \tag{B.24}$$

$$\tau_{ij}^{SGS} = \bar{\rho}\widetilde{u_i u_j} - \bar{\rho}\widetilde{u_i}\widetilde{u_j} \tag{B.25}$$

$$\widetilde{\sigma_{ij}} = \mu\left(\frac{\partial \widetilde{u_i}}{\partial x_j} + \frac{\partial \widetilde{u_j}}{\partial x_i} - \frac{2}{3}\frac{\partial \widetilde{u_k}}{\partial x_k}\delta_{ij}\right) \tag{B.26}$$

Energy Equation:

$$\frac{\partial (\overline{\rho}\, \tilde{E})}{\partial t} + \underbrace{\frac{\partial (\overline{(\rho E + p)u_j})}{\partial x_j}} = -\frac{\partial \widetilde{q_j}}{\partial x_j} + \frac{\partial \left(\widetilde{\sigma_{ij} u_i}\right)}{\partial x_j} \tag{B.27}$$

B.III

Term B.III together with equation B.9 gives:

$$\overline{(\rho E + p)u_j} = \overline{\left(\frac{1}{2}\rho u_i u_i u_j + \rho e u_j + p u_j\right)} \tag{B.28}$$

$$e = c_v T \tag{B.29}$$

$$p = R\rho T \tag{B.30}$$

$$c_p = c_v + R \tag{B.31}$$

$$\overline{(\rho E + p)u_j} = \frac{1}{2}\bar{\rho}\widetilde{u_i u_i u_j} + \bar{\rho} c_v \widetilde{T u_j} + \bar{\rho} R \widetilde{T u_j} \tag{B.32}$$

Employing the relation displayed by equation B.31 yields:

$$\overline{(\rho E + p)u_j} = \frac{1}{2}\bar{\rho}\widetilde{u_i u_i u_j} + \bar{\rho} c_p \widetilde{T u_j} \tag{B.33}$$

Equation B.33 can be rewritten as:

$$\overline{(\rho E + p)u_j} = \frac{1}{2}\bar{\rho}\widetilde{u_\iota u_\iota}\tilde{u}_j + \bar{\rho}c_p\tilde{T}\tilde{u}_j + \frac{1}{2}D_j + c_p q_T^{SGS} \quad (B.34)$$

where

$$D_j = \bar{\rho}\widetilde{u_\iota u_\iota u_j} - \bar{\rho}\widetilde{u_\iota u_\iota}\tilde{u}_j \quad (B.35)$$

$$q_T^{SGS} = \bar{\rho}c_p\widetilde{Tu_j} - \bar{\rho}c_p\tilde{T}\tilde{u}_j \quad (B.36)$$

Equation B.34 can be again decomposed and written as

$$\overline{(\rho E + p)u_j} = \frac{1}{2}\bar{\rho}\tilde{u}_\iota\tilde{u}_\iota\tilde{u}_j + \frac{1}{2}\left(\tau_{ij}^{SGS}\tilde{u}_j\right) + \bar{\rho}c_p\tilde{T}\tilde{u}_j + \frac{1}{2}D_j + c_p q_T^{SGS} \quad (B.37)$$

$$\tau_{ij}^{SGS}\tilde{u}_j = \bar{\rho}\widetilde{u_\iota u_\iota}\tilde{u}_j - \bar{\rho}\tilde{u}_\iota\tilde{u}_\iota\tilde{u}_j \quad (B.38)$$

Equation B.37 can be rewritten in terms of variable E and p as:

$$\overline{(\rho E + p)u_j} = \bar{\rho}\tilde{E}\tilde{u}_j + \widetilde{pu}_j + \frac{1}{2}(\tau_{ij}^{SGS}\tilde{u}_j) + \frac{1}{2}D_j + c_p q_T^{SGS} \quad (B.39)$$

Now equation B.27 can be written as

$$\frac{\partial\left(\overline{\rho}\,\tilde{E}\right)}{\partial t} + \frac{\partial\left(\bar{\rho}\tilde{E}\tilde{u}_j + \widetilde{pu}_j\right)}{\partial x_j} = -\frac{\partial\widetilde{q}_j}{\partial x_j} + \frac{\partial\left(\widetilde{\sigma_{\iota j}}\tilde{u}_\iota\right)}{\partial x_j} - \frac{1}{2}\frac{\partial\left(\tau_{ij}^{SGS}\tilde{u}_j\right)}{\partial x_j} - c_p\frac{\partial q_T^{SGS}}{\partial x_j} - \frac{1}{2}\frac{\partial D_j}{\partial x_j} + \frac{\partial\left(\widetilde{\sigma_{\iota j}u_\iota} - \widetilde{\sigma_{\iota j}}\tilde{u}_\iota\right)}{\partial x_j} \quad (B.40)$$

The last 2 terms of R.H.S from equation B.41 are generally small compared to other subgrid terms and therefore can be neglected

$$\frac{\partial\left(\overline{\rho}\,\tilde{E}\right)}{\partial t} + \frac{\partial\left(\bar{\rho}\tilde{E}\tilde{u}_j + \widetilde{pu}_j\right)}{\partial x_j} = -\frac{\partial\widetilde{q}_j}{\partial x_j} + \frac{\partial\left(\widetilde{\sigma_{\iota j}}\tilde{u}_\iota\right)}{\partial x_j} - \frac{1}{2}\frac{\partial\left(\tau_{ij}^{SGS}\tilde{u}_j\right)}{\partial x_j} - c_p\frac{\partial q_T^{SGS}}{\partial x_j} \quad (B.41)$$

$$\widetilde{q_J} = -k\frac{\partial \tilde{T}}{\partial x_j} \tag{B.42}$$

Scalar Equation:

$$\frac{\partial(\overline{\rho}\,\widetilde{\emptyset})}{\partial t} + \frac{\partial(\overline{\rho}\,\widetilde{\emptyset u_j})}{\partial x_j} = \frac{\partial}{\partial x_j}\left(\overline{\rho}\,D_{\emptyset}\frac{\partial \widetilde{\emptyset}}{\partial x_j}\right) \tag{B.43}$$

$$\frac{\partial(\overline{\rho}\,\widetilde{\emptyset})}{\partial t} + \frac{\partial(\overline{\rho}\,\widetilde{\emptyset}\widetilde{u_j})}{\partial x_j} = \frac{\partial}{\partial x_j}\left(\overline{\rho}\,D_{\emptyset}\frac{\partial \widetilde{\emptyset}}{\partial x_j}\right) - \frac{\partial {q_j}^{SGS}}{\partial x_j} \tag{B.44}$$

where ${q_j}^{SGS}$ represents the turbulent diffusion (${q_j}^{SGS} = q_T^{SGS}$ for $\emptyset = T$)

$${q_j}^{SGS} = \bar{\rho}\widetilde{\emptyset u_J} - \bar{\rho}\widetilde{\emptyset}\widetilde{u_J} \tag{B.45}$$

The subgrid-scale stresses resulting from the filtering operation are unknown, and require modeling. For scalar, momentum, and energy equations, one needs to model the fluxes ($\tau_{ij}^{SGS}, {q_j}^{SGS}$) for scales smaller than the filter width. This closure problem is solved using the subgrid-scale models. The subgrid-scale turbulence models in STAR-CCM+ employ the Boussinesq hypothesis [55] as in the RANS models, for computing subgrid-scale turbulent stresses from

$$\tau_{ij}^{SGS} = \frac{1}{3}\tau_{kk}\delta_{ij} - 2\mu_t\widetilde{S_{\iota J}} \tag{B.46}$$

where μ_t is the subgrid-scale turbulent viscosity. The isotropic part of the subgrid-scale stresses τ_{kk} is not modeled, but added to the filtered static pressure term. $\overline{S_{ij}}$, the rate-of-strain tensor for the resolved scale is defined by

$$\widetilde{S_{\iota J}} = \frac{1}{2}\left(\frac{\partial \widetilde{u_\iota}}{\partial x_j} + \frac{\partial \widetilde{u_j}}{\partial x_i}\right) \tag{B.47}$$

Subgrid-scale turbulent flux of a scalar, is modeled using a subgrid-scale turbulent Schmidt number (turbulent Prandtl number Pr_t for Energy closure, i.e., for $\emptyset = T$)

$$q_j{}^{SGS} = -\frac{\mu_t}{Sc_t}\frac{\partial \emptyset}{\partial x_j} \qquad (B.48)$$

μ_t is modeled using the WALE (Wall-Adapting Local-Eddy Viscosity) subgrid-scale model[68]. It uses an algebraic formulation to model the subgrid-scale stresses. This is the simplest, and hence the least computationally expensive, subgrid-scale modeling approach. Studies showed that it is less sensitive to the value of the coefficient than the Smagorinsky model. Also, it automatically gives accurate scaling at walls. It provides the following mixing-length type formula for the subgrid-scale viscosity:

$$\mu_t = \rho \Delta^2 S_w \qquad (B.49)$$

where ρ is the density, S_w is deformation parameter, and Δ is the length scale or grid filter width defined in terms of the cell volume V as:

$$\Delta = \begin{cases} C_w V^{\frac{1}{3}} & if\ length\ scale\ limit\ is\ not\ applied \\ \min\left(\gamma d, C_w V^{\frac{1}{3}}\right) & if\ length\ scale\ limit\ is\ applied \end{cases} \qquad (B.50)$$

Here γ is the von Karman constant with value 0.41 and the coefficient C_w has value 0.544 for the course of the study.

$$S_w = \frac{\left(S_{ij}^d S_{ij}^d\right)^{3/2}}{\left(\overline{S_{ij}}\,\overline{S_{ij}}\right)^{5/2} + \left(S_{ij}^d S_{ij}^d\right)^{5/4}} \qquad (B.51)$$

The deformation tensor S_{ij}^d is defined as:

$$S_{ij}^d = \frac{1}{2}\left(\overline{g_{ij}}^2 + \overline{g_{ji}}^2\right) - \frac{1}{2}\,\delta_{ij}\overline{g_{kk}}^2 \quad , \qquad \overline{g_{ji}} = \frac{\partial \overline{u_i}}{\partial x_j} \qquad (B.52)$$

REFERENCES

[1] W.L. Oberkampf and T.G. Trucano. "Verification and Validation in Computational Fluid Dynamics". *Sandia Report*, SAND2002-0529, March 2002

[2] S. Schlesinger. "Terminology for model credibility." *Simulation*, vol. 32, pp.103-104, 1979.

[3] P. J. Roache. *Verificaiton and Validation in Computational Science and Engineering*, Albuquerque, NM, Hermosa Publishers, 1998.

[4] P.J. Roache. "Verificaiton of Codes and Calculations." *AIAA Journal*, vol.36, No.5, pp. 696-702, 1998.

[5] W.L. Oberkampf, T.G. Trucano, and C. Hirsch. "Verification, Validation, and Predictive Capability in Computational Engineering and Physics." Proc. Foundations 02, Johns Hopkins Univ., Laurel, MD, Oct 2002

[6] C. E. Baukal Jr.,*The John Zink Combustion Hand Book*, CRC Press, 2001, pp. 589-634.

[7] U.S. Environmental Protection Agency, Greenhouse Gases and Global Warming Potential Values , http://www.epa.gov.

[8] M. R. Johnson, and L. W. Kostiuk. "Efficiencies of Low-Momentum Jet Diffusion Flames in Crosswinds." *Combustion and Flame*, Vol. 123, pp.189-200, 2000.

[9] E. Bourguignon, M. R. Johnson, and L. W. Kostiuk. "The Use of Closed-Loop Wind Tunnel for Measuring the Combustion Efficiency of Flames in a Cross Flow." *Combustion and Flame*, Vol. 119, pp.319-334, 1999.

[10] M. R. Johnson, and L. W. Kostiuk. "A Parametric Model for the Efficiency of a Flare in Crosswind." *Proceedings of the Combustion Institute*, Vol. 29, pp. 1943- 1950, 2002.

[11] A. J. Majeski, D. J.Wilson, and L. W. Kostuik, "Size and Trajectory of a Flare in a Cross Flow" Combustion Canada, Calgary Alberta, May 1999.

[12] J. H. Pohl, J. Lee, and R. Payne. "Combustion Efficiency of Flares." *Combust. Sci. Technol,* vol. 50, pp.217–231, 1986.

[13] N. R. Soelberg, "Evaluation of the Efficiency of Industrial Flares: Influence of Gas Composition." U.S. EPA Rept. 600/2-83-070, Washington, D.C, 1983.

[14] T. J. O'Hern, E. J. Weckman, A. L. Gerhart, S. R. Tieszen and R. W. Schefer. "Experimental study of a turbulent buoyant helium-plume." *J. Fluid Mech* , vol. 544, pp.143-171, 2005.

[15] G. Blanquart and H. Pitsch, "Large-eddy simulation of a turbulent buoyant helium-plume." Annual Research Briefs, Centre for Turbulence Research, 2008.

[16] User Guide, STAR-CCM+ V5.06.010

[17] A. Jatale, P. Smith, J. Thornock, S. Smith, and M Hradisky. "Measurement of Combustion Efficiency for Wind Tunnel Flares with Uncertainty Quantification." In Preparation , 2014.

[18] J. Abanto, D. Pelletiery, A. Garonz, J.Y. Trepanier and M. Reggio. "Verification of some Commercial CFD Codes on Atypical CFD Problems." 43rd AIAA Aerospace Sciences Meeting and Exhibit, Reno NV, January 2005.

[19] A.G. Sunderland, M. Ashworth, N. Li and C. Moulinec. "Towards Petascale Computing with Parallel CFD codes." Parallel CFD, Lyon, France, May 19-22, 2008.

[20] V J. Romero, "Elements of a Pragmatic Approach for Dealing with Bias and Uncertainty in Experiments through Predictions." SANDIA report, November 2011.

[21] C.J. Roy, and W.L. Oberkampf. "A Complete Framework for Verification, Validation, and Uncertainty Quantification in Scientific Computing." 48th AIAA Aerospace Sciences Meeting, , Orlando, Florida , 4 - 7 January 2010.

[22] M. J. Bayarri, J.O. Berger, R. Paulo and J. Sacks. "A Framework for Validation of Computer Models." *Technometrics*, vol. 49, no. 2, May 2007.

[23]American Institute of Aeronautics and Astronautics. "Guide for the Verification and Validation of Computational Fluid Dynamics Simulations." AIAA G-077-1998, AIAA, Reston, Va, 1998.

[24] American Society of Mechanical Engineers. "V&V 10 – 2006 Guide for Verification and Validation in Computational Solid Mechanics." available from ASME Codes & Standards website.

[25] I. Babuska, F. Nobile and R. Tempone. "Reliability of Computational Science." *Num. Methods in Partial Differential Equations*, Vol. 23, pp. 753-784, 2007.

[26] I. Babuska, J.T. Oden, and M. Papadrakakis. "Verification and Validation in Computational Engineering and Science: Basic Concepts." *Comput. Methods in Applied Mechanics and Engrng.*, Vol. 193, pp. 4057-4066, 2004.

[27] O. Balci. "Verification, Validation and Testing," Handbook of Simulation, ed. J. Banks, Engineering and Management Press (1998), pp. 335-393.

[28] A. R. Black, M. L. Hobbs, K. J. Dowding and T. K. Blanchat. "Uncertainty Quantification and Model Validation of Fire/Thermal Response Predictions", 18th AIAA Computational Fluid Dynamics Conference, Miami, FL, June 25-28, 2007.

[29] F.G. Blottner. "Accurate Navier-Stokes Results for the Hypersonic Flow over a Spherical Nosetip." *AIAA J. Spacecraft and Rockets*, Vol. 27, No.2, pp. 113-122, March-April 1990.

[30] K. Campbell. "A Brief Survey of Statistical Model Calibration Ideas." International Conference on Sensitivity Analysis of Model Output, Santa Fe, NM, March 8 – 11, 2004.

[31] M.J. Bayarri, J. O. Berger, D. Higdon, M. C. Kennedy, A. Kottas, R. Paulo, J. Sacks, J. A. Cafeo, J. C. Cavendish, C.H. Lin, and J. Tui. "A Framework for Validation of Computer Models." NISS Technical report 128, October 2002.

[32] M.G. Morgan, and M. Henrion. *Uncertainty: A Guide to Dealing with Uncertainty in Quantitative Risk and Policy Analysis*, 1st Ed., Cambridge, UK, Cambridge University Press, 1990.

[33] A.C. Cullen, and H.C. Frey, *Probabilistic Techniques in Exposure Assessment: A Handbook for Dealing with Variability and Uncertainty in Models and Inputs*, New York, Plenum Press, 1999.

[34] D. Vose. *Risk Analysis: A Quantitative Guide*, 3rd Ed., New York, Wiley, 2008.

[35] Y.Y. Haimes. *Risk Modeling, Assessment, and Management*, 3rd Ed., New York, John Wiley, 2009.

[36] A. D. Kiureghiana and O. Ditlevsen. "Aleatory or Epistemic? Does it Matter?." *Structural Safety*, vol. 31, iss. 2, pp. 105–112, March 2009.

[37] H. G. Matthies. " Quantifying Uncertainty: Modern Computational Representation of Probability and Applications, Extreme Man-Made and Natural Hazards in Dynamics of Structures." *NATO Security through Science Series*, pp.105-135, 2007.

[38] M. C. Kennedy and A. O'Hagan. "Bayesian Calibration of Computer Models." *Journal of the Royal Statistical Society: Series B (Statistical Methodology)*, vol. 63, iss. 3, pp. 425–464, 2001.

[39] S. Ferson, W.L. Oberkampf, and L. Ginzburg. "Model Validation and Predictive Capability for the Thermal Challenge Problem." *Computer Methods in Applied Mechanics and Engineering*. Vol. 197, pp. 2408-2430 , 2008.

[40] S. Ferson, and L.R. Ginzburg. "Different Methods are Needed to Propagate Ignorance and Variability." *Reliability Engineering and System Safety*, Vol. 54, pp. 133-144, 1996.

[41] S. Ferson, and J.G. Hajagos."Arithmetic with Uncertain Numbers: Rigorous and (Often) Best Possible Answers." *Reliability Engineering and System Safety*. Vol. 85, Nos. 1-3, pp. 135-152, 2004.

[42] P.A. Cavallo, and N. Sinha. "Error Quantification for Computational Aerodynamics Using an Error Transport Equation." *Journal of Aircraft*, Vol. 44, No. 6, pp. 1954-1963, 2007.

[43] T.I-P. Shih, and B.R. Williams. "Development and Evaluation of an A Posteriori Method for Estimating and Correcting Grid-Induced Errors in Solutions of the Navier-Stokes Equations." *AIAA*. Paper 2009-1499, 2009.

[44] M. Ainsworth, and J.T. Oden. "A Posteriori Error Estimation in Finite Element Analysis." *Computer Methods in Applied Mechanics and Engineering*, Vol. 142, No. 1-2, pp. 1-88, 1997.

[45] O.C. Zienkiewicz, and J.Z. Zhu. "The Superconvergent Patch Recovery and A Posteriori Error Estimates, Part 2: Error Estimates and Adaptivity." *International Journal for Numerical Methods in Engineering*, Vol. 33, pp. 1365-1382, 1992.

[46] H.W. Coleman, and F. Stern."Uncertainties and CFD Code Validation." *Journal of Fluids Engineering*, Vol. 119, pp. 795-803, 1997.

[47] F. Stern, R.V. Wilson, H.W. Coleman, and E.G. Paterson. "Comprehensive Approach to Verification and Validation of CFD Simulations-Part 1: Methodology and Procedures." *Journal of Fluids Engineering*, Vol. 123, No. 4, pp. 793-802, 2001.

[48] W.L. Oberkampf, and T.G. Trucano. "Verification and Validation in Computational Fluid Dynamics," *Progress in Aerospace Sciences*, Vol. 38, No. 3, pp. 209-272, 2002.

[49] M. N. Avramova, and K. N. Ivanov. "Verification, Validation and Uncertainty Quantification in Multi-physics Modeling for Nuclear Reactor Design and Safety Analysis." *Progress in Nuclear Energy*, vol.52, pp.601-614, 2010.

[50] O.M. Knio, and O.P. Le Maıtre. "Uncertainty Propagation in CFD Using Polynomial Chaos Decomposition." *Fluid Dyn. Res.,* vol. 38, iss. 9, pp.616–640, 2006.

[51] H. N. Najm. "Uncertainty Quantification and Polynomial Chaos Techniques in Computational Fluid Dynamics." *Annu. Rev. Fluid Mech*. Vol.41, pp.35–52, 2009.

[52] R. Feeley, P. Seiler, A. Packard, and M. Frenklach. "Consistency of a Reaction Dataset."*J. Phys. Chem. A*, vol.108, pp.9573–9583, 2004.

[53] R. Feeley, M. Frenklach, M. Onsum, T. Russi, A. Arkin, and A. Packard. "Model Discrimination Using Data Collaboration." *J. Phys. Chem. A*, vol.110, pp.6803–6813, 2006.

[54] M. Frenklach, A. Packard, P. Seiler, and R. Feeley. “Collaborative Data Processing in Developing Predictive Models of Complex Reaction Systems.” *International Journal of Chemical Kinetics*, vol.36, iss.1,pp.57–66, 2004.

[55] C.M. Rhie, and W.L. Chow. “A Numerical Study of the Turbulent Flow Past an Isolated Airfoil with Trailing Edge Separation.” *AIAA Journal*, vol.21, pp.1525-1532, 1983.

[56] J. O. Hinze. *Turbulence*. New York, McGraw-Hill Publishing Co., 1975.

[57] F. Nicoud, and F. Ducros. “Subgrid-Scale Stress Modeling Based on the Square of the Velocity Gradient Tensor.” *Flow, Turbulence and Combustion*, vol.62, pp. 183-200. 1999.

[58] R.W. Logan, and C.K. Nitta. “Comparing 10 Methods for Solution Verification, and Linking to Model Validation.” Tech. Rep. UCRL-TR-210837, Lawrence Livermore National Laboratory. 2005.

[59] C.J. Roy. “Review of Code and Solution Verification Procedures for Computational Simulation.” *Journal of Computational Physics*. vol.205, pp.131–156,2005 .

[60] L. Shunn and F. Ham. “Method of Manufactured Solutions Applied to Variable-density Flow Solvers.” *Annual Research Briefs*, Center for Turbulence Research 2007.

[61] S. R. Tieszen, T. J. O’Hern, R. W. Schefer ,E. J. Weckman, and T.K. Blanchat . “Experimental Study of the Flow Field In and Around A One Meter Diameter Methane Fire.” *Combustion and Flame* , vol.129, pp.378–391, 2002.

[62] http://chpc.utah.edu/docs/manuals/hardware/#ember

[63] J.A. Cafeo and J.C. Cavendish. “A Framework for Verification and Validation of Computer Models and Simulations.” General Motors Document, 2001.

[64] M. Pilch, T. Trucano, J. Moya, G. Hodges, and D. Peercy. “Guidelines for Sandia ASCI Verification and Validation Plans-Content and Format: Version 2.0.” Sandia National Laboratories Report -SAND2000-3101, January 2001.

[65] P. Moin, K. Squires, W. Cabot, and S, Lee. “A Dynamic Subgrid-scale Model for Compressible Turbulence and Scalar Transport.” *Phys fluid, A3,* vol. 11, November 1991

[66] T. Beji, J.P. Zhang, W. Yao, and M. Delichatsios. “On the Limitations of Constant Prandtl and Schmidt Numbers Assumption in LES Simulations of Reacting Buoyant Plumes.” Fourth European Combustion Meeting, Vienna University of Technology, Vienna, Austria, 2009.

[67] Y. Xin, and J.P. Gore. “Two-dimensional Soot Distributions in Buoyant Turbulent Fires.” *Proceedings of the Combustion Institute*. vol.30 , pp.719-726, 2005.

[68] I. Yimer, I. Campbell, and L.-Y. Jiang. "Estimation of the Turbulent Schmidt Number from Experimental Profiles of Axial Velocity and Concentration for High-Reynolds-Number Jet Flows." *Canadian Aeronautics and Space Journal*, vol.48, iss.3, pp.195-200,2002.

[69] J.X. Wen, K. Kang, T. Donchev, and J.M. Karwatzki. "Validation of FDS for the Prediction of Medium-scale Pool Fires." *Fire Safety Journal*, vol. 42 ,pp.127-138,2007.

[70] G. Box, and K.B.Wilson. "On the Experimental Attainment of Optimum Conditions." *Journal of the Royal Statistical Society, Series B*. vol.13, iss.1, pp.1–45. 1951.

[71] D.F. Waston. *Contouring: A Guide To The Analysis And Display Of Spatial Data*. New York: Pergaman Press, 1992. , pp.130-136.

[72] S. W. Sloan. "A Fast Algorithm for Generating Constrained Delaunay Triangulations." *Computers and Structures ,* vol. 47, iss.3, pp.441-450,1993.

[73] P. Smith, S. Smith, J. Thornock, A. Jatale, D. Nguyen and B. Schroeder. "A Validation Methodology for Quantifying Uncertainty in High Performance Computer-Based Simulations with Sparse Experimental Data". ASME Verification and Validation Symposium, May 2-4, 2012.

[74] A. Jatale, P. Smith, S. Smith, J. Thornock and M. Hradisky, "Validation and Uncertainty Quantification: Prediction for Problem with No Experimental Data", In preparation.

[75] B.M. Cetegen, and K.D. Kasper. "Experiments on the Oscillatory Behavior of Buoyant Plumes of Helium and Helium-air Mixtures." *Phys. Fluids*, vol. 8, pp.2974-2984, 1996.

[76] B.M. Cetegen and T.A. Ahmed. "Experiments on the Periodic Instability of Buoyant Plumes and Pool Fires." *Combust. Flame*, vol. 93, pp.157, 1993.

[77] A. Jatale, P. Smith, J. Thornock, S. Smith and M. Hradisky. "Validation and Uncertainty Quantification of a Turbulent Buoyant Helium-plume." In Preparation.

[78] H. Qin, V. V. Lissianski, H. Yang, W. C. Gardiner, S. G. Davis and H. Wang, "Combustion Chemistry of Propane: A Case Study of Detailed Reaction Mechanism Optimization." *Proceedings of the Combustion Institute*, vol. 28, pp. 1663–1669, 2000

[79] P.E.G. Gogolek , and A.C.S. Hayden. "Performance of Flare Flames in a Crosswind With Nitrogen Dilution." *Journal of Canadian Petroleum Technology*, vol. 43, iss. 8, pp.43-47 , August 2004.

[80] P R. Desam, P. J. Smith, S. G. Borodai and S. Kumar, "Computing Flare Dynamics Using Large Eddy Simulations." Combustion and Reaction Simulations (CRSIM) Research Group University of Utah, Salt Lake City, 2003.